Technische Universität München

Walther-Meißner-Institut für Tief-Temperaturforschung

Bayerische Akademie der Wissenschaften

Fabrication of Superconducting Thin-film Resonators and Josephson Junctions

---

Master's Thesis

Christoph Scheuer

Supervisor: Dr. Frank Deppe

Advisor: Yuki Nojiri

Garching – February 23, 2021

Contents

Chapter 1

Introduction

Quantum science and technology (QST) is a broad field, which has attracted more and more attention during the last years. In September 2020, the Bavarian State Government decided to support this field by allocating a budget of about 120 million euros for the following two years. The growing interest in this topic led to the establishment of the Munich Center for Quantum Science and Technology (MCQST) [1] cluster of excellence funded by the German Research Foundation (DFG). Besides basic research, the aim is to develop new applications in quantum information theory, quantum simulation, quantum computing, quantum communication, quantum matter as well as quantum metrology and sensing.
One of the key platforms to investigate fundamental quantum mechanics and the scalability of quantum information processing are superconducting quantum circuits. Here, quantum bits, or qubits, serve as principal information units. In general, a qubit can be seen as an artificial two-level atom [2]. These circuits typically consist of two important components:

- The qubit.
  In our case, we focus on so called transmon qubits. They origin from the Cooper pair box [3]. The core element is a Josephson junction [4]. By shunting this junction with a capacitance, one obtains a charge-insensitive qubit (transmon qubit) [5]. The nonlinear inductance of the junction facilitates the formation of the desired two-level system.

- Coplanar waveguide (CPW) resonators.
  They can be used to study light-matter interaction [6], as microwave photon storage devices [7], for qubit readout [8], or as quantum bus [9].

Building these superconducting circuits is a challenging task in micro- and nanofabrication. This task includes wafer cleaning methods, spin coating techniques, electron beam (e-beam) patterning and e-beam evaporation. In this context it is important to understand that, although many of the relevant techniques and requirements are generally known, their establishment in a specific lab is still a highly nontrivial task.
At the Walther-Meißner-Institute (WMI), such devices are fabricated for many applications. The goal of this work is to analyze the current aluminum fabrication process step by step and to contribute to its advancement. The specific steps taken are the following. First, we implement a new sample holder in our evaporation system, which allows us to evaporate up to 4 inch wafers in the future. However, for now we remain with silicon substrates diced to a 6 mm $\times$ 10 mm size. During our analysis, we notice a lack of consistency when fabricating multiple Josephson junctions even on the same chip. Therefore, we decide to implement a new design, namely the cross-type junction. We analyze the junction properties and stability by performing room temperature resistance measurements. According to the Ambegaokar-Baratoff relation, one then gets insight about the junction critical current by the normal state resistance [10].
In a second main effort, we fabricate superconducting resonators in order to analyze the material deposition process. For many applications in circuit quantum electrodynamics, the coherence time is limited by internal loss channels of the circuit. By performing transmission measurements at cryogenic temperatures, we investigate the different loss mechanisms, such as two-level systems (TLSs), quasiparticle loss or radiation. By extracting different loss participations and investigating their origin, we can improve the material process. For example, it has been shown, that TLSs are typically located at surfaces or interfaces [11], which means an improvement of the interfaces will decrease TLS losses.

The thesis is structured as follows.
In chapter 2, we introduce the theory aspects, which are important for this work. After introducing the phenomenom of superconductivity briefly, we investigate Josephson junctions, which are essential for many applications in superconducting circuits. Later, we define the Ambegaokar-Baratoff relation, which allows us to characterize our junctions by measuring their resistance at room temperature. Next, we focus on transmission lines and coplanar waveguide resonators. Most important for this work is the internal quality factor Q_i. In order to deduce this quality factor, we present an algorithm, which allows us to extract the desired internal quality factor from a transmission measurement by a suitable fitting method. Finally, we discuss different loss mechanisms in superconducting resonators.
In chapter 3, we present some experimental techniques, including sample fabrication and our measurement setups. In particular, we show the setup for normal resistance measurements of SQUID loops, as well as the cryogenic setup used for transmission measurements of resonators.
In chapter 4, we present our experimental results. First, we go through the fabrication process step by step and show the improvements we achieve during the course of this thesis. Second, we present the room temperature resistance measurements from SQUID loops and discuss the influence of different fabrication parameters. Afterwards, we extract the internal losses from transmission measurements of our resonators and give a guideline, how to distinguish the different loss sources and how to reduce them.
Finally, we conclude and summarize our studies and provide an outlook onto plans for the future regarding the fabrication of Josephson junctions and superconducting resonators.

Chapter 2

Theory

In this chapter, we discuss the theory aspects, which are important for this work. At first, we introduce the phenomenon of superconductivity briefly. Thus, we give a short historical background and show the quantum mechanical description of this effect.
Next, we investigate Josephson junctions. Their nonlinear behaviour is essential for many applications in superconducting circuits. After deriving the Josephson equations, we represent our junctions by an equivalent electrical circuit according to the resistively and capacitively shunted junction (RCSJ) model.
Later, we define the Ambegaokar-Baratoff relation. This allows us, to characterize our junctions by measuring their resistance at room temperature.
After explaining the nonlinear part of our circuits, we focus on the linear elements, namely transmission lines and coplanar waveguide resonators. Therefore, we give a short overview of transmission line theory in general. For this purpose, we show a lumped-element circuit model, how electromagnetic waves propagate on such a transmission line, as well as wave reflection, caused by an impedance mismatch.
In the next section, we focus on coplanar waveguide resonators in particular. After showing a circuit model, we define all characteristic variables. For this work, the internal quality factor Q_i is most important. From measurements, it is only possible to deduce a loaded quality factor. Hence, we present an algorithm, which allows us to extract the desired internal quality factor from a transmission measurement by a suitable fitting method.
Finally, we discuss different loss mechanisms in superconducting resonators. As the internal quality factor Q_i is inversely proportional to the internal loss tangent, we gain insight into the quality of our fabrication process.

2.1 Superconductivity

In general, superconductivity manifests in two properties. First, it shows a vanishing resistance below a critical temperature T_c. Second, a superconductor repells any magnetic field from the material when it is in its superconducting state. The phenomenon of vanishing resistance was first shown by Heike Kamerlingh Onnes in 1911 on mercury [12]. For thin-film aluminum, one finds $T_c \approx 1.2$ K. Later in 1933, Walther Meißner and Robert Ochsenfeld discovered the second effect and concluded, that every superconductor is also a perfect diamagnet [13]. Two years later, Fritz and Heinz London proposed a phenomenological model [14], followed by V. L. Ginzburg and L. D. Landau in 1950 [15]. Their theories contain a macroscopic model for superconductivity. In 1957, John Bardeen, Leon Neil Cooper and John Robert Schrieffer could explain superconductivity quantum mechanically with a microscopic model [16]. A fundamental result is, that superconductivity is a macroscopic quantum effect. In the superconducting state, electrons close to the Fermi energy level form so-called Cooper pairs, which show rather bosonic than a fermionic behavior. One can define a macroscopic wave function of all Cooper pairs by [17]:

$$\Psi(r,t) = \Psi_0(r,t) \cdot \mathrm{e}^{i\Theta(r,t)} = \sqrt{n_s(r,t)} \cdot \mathrm{e}^{i\Theta(r,t)} \tag{2.1}$$

with $n_s(r,t) = |\Psi|^2$ being the local density of all Cooper pairs and $\Theta(r,t)$ the macroscopic phase. In order to break a Cooper pair, an energy of 2Δ is required, where Δ is the superconducting energy gap.
The supercurrent density J_s is given by

$$J_s = \frac{q\hbar n_s(r,t)}{m} \left\{ \nabla\Theta(r,t) - \frac{2\pi}{\varphi_0} A(r,t) \right\} = \frac{q\hbar n_s(r,t)}{m} \gamma(r,t). \tag{2.2}$$

Here, $q = 2e$ and $m = 2m_e$ are the specific charge and mass of a Cooper pair. A is a vector potential defined as $B = \nabla \times A$, where B is the magnetic field. One immediatly recognizes, that the supercurrent density is proportional to the gauge invariant phase gradient $\gamma(r,t)$. This phase difference induced supercurrent will be important for the following section.

2.2 Josephson effect

The Josephson effect can be observed, if we weakly couple two superconductors, as illustrated in Fig. 2.1. In our case, they are seperated by an insulating oxide barrier of 1-2 nm. The behavior of such a system was first investigated by Brian D. Josephson. He derived the two Josephson equations [4].

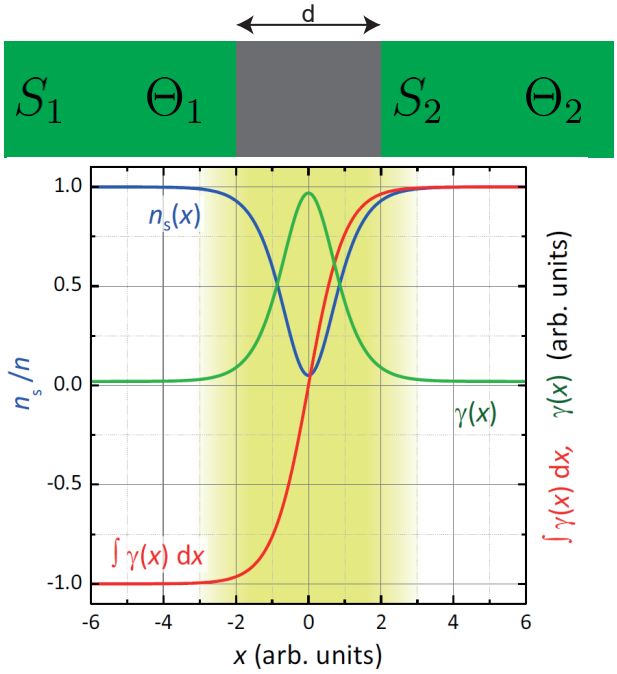

Figure 2.1: Top: Schematic drawing of a Josephson junction. It consists of two superconducting electrodes S_1 and S_2 (green), each with individual phase $\Theta_{1,2}$, separated by an insulating barrier of thickness d (grey).
Bottom: The graph shows the distribution of the Cooper pair density $n_s(x)$ (blue), the gauge invariant phase gradient $\gamma(x)$ and the integral of the phase gradient $\int \gamma(x)dx$ across the junction. In the absence of an external magnetic field, the integral is equal to the phase difference $\varphi = \Theta_1 - \Theta_2$. Picture was adapted from [18].

2.2.1 Josephson equations

The first equation describes the relation of supercurrent I_s and phase in the system by

$$I_s = I_c \cdot \sin(\varphi). \tag{2.3}$$

Here, omitting the contribution of an external magnetic field for simplicity, $\varphi = \Theta_1 - \Theta_2$ is the phase difference between superconductor S_1 and S_2. I_c is called the critical current and is a material parameter.

The second Josephson equation connects a voltage drop V over the barrier to a time-varying phase difference:

$$\frac{\partial \varphi}{\partial t} = \frac{2\pi}{\Phi_0} V, \tag{2.4}$$

where $\Phi_0 = \frac{h}{2e}$ is the magnetic flux quantum.

2.2.2 The RCSJ-model

In 1968, Stewart and McCumber introduced the resistively and capacitively shunted junction (RCSJ) model in order to describe the Josephson junction dynamics in terms of a circuit analysis language. According to this model, the equivalent circuit contains a nonlinear inductance L_J, a normal resistance R_n, and a capacitance C (Fig. 2.2).

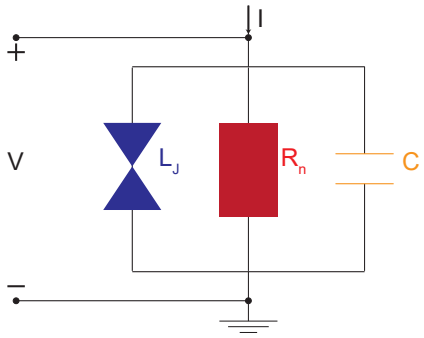

Figure 2.2: Schematic circuit of a Josephson junction according to the RCSJ model. The circuit contains a nonlinear inductance L_J, a normal resistance R_n, and a capacitance C.

By using Kirchhoff's law, one can denote the total current through the junction as:

$$I_\mathrm{tot} = I_\mathrm{s} + I_\mathrm{n} + I_\mathrm{d} = I_\mathrm{c} \sin(\varphi) + \frac{V}{R_\mathrm{n}} + C\frac{dV}{dt}, \tag{2.5}$$

where I_s the supercurrent, I_n a normal current through the resistance and I_d a displacement current, caused by the capacitance. Note, that the nonlinear inductance is hidden in the supercurrent as

$$V = L_\mathrm{s}\frac{dI_\mathrm{s}}{dt}. \tag{2.6}$$

Calculating the time derivative of the first Josephson Eq. 2.3 and inserting the second Josephson Eq. 2.4, we obtain:

$$L_\mathrm{s} = \frac{L_\mathrm{J}}{\cos(\varphi)}, \tag{2.7}$$

with $L_\mathrm{J} = \frac{\hbar}{2eI_\mathrm{c}}$ being the Josephson inductance.
If we insert both Josephson equations into Eq. 2.5 and substitute V, we obtain the nonlinear differential equation

$$I_\mathrm{tot} = I_\mathrm{c}\sin(\varphi) + \frac{1}{R_\mathrm{n}}\frac{\varphi_0}{2\pi}\frac{d\varphi}{dt} + C\frac{\Phi_0}{2\pi}\frac{d^2\varphi}{dt^2}. \tag{2.8}$$

2.2.3 Ambegaokar-Baratoff relation

In 1963, Ambegaokar and Baratoff discovered that the critical supercurrent (density) I_c (J_c) is related to the normal state resistance R_n via [10]

$$I_\mathrm{c}R_\mathrm{n} = \frac{\pi}{2e}\Delta(T)\tanh\left(\frac{\Delta(T)}{2k_\mathrm{B}T}\right), \tag{2.9}$$

with $I_\mathrm{c} = J_\mathrm{c}A$ and A being the junction area, $\Delta(T)$ the superconducting energy gap, and k_B is the Boltzmann constant.

2.2.4 The superconducting quantum interference device (SQUID)

In our work, we don't fabricate single junctions, but superconducting quantum interference devices (SQUIDs). These consist of two superconducting branches, which are arranged in a loop (Fig. 2.3). Each branch is interrupted by an insulating barrier, forming a Josephson junction. The supercurrent I_S through the SQUID splits up into two supercurrents I_{S1} and I_{S2},

$$I_S = I_{S1} + I_{S2} = 2I_c \cos\left(\frac{\varphi_1 - \varphi_2}{2}\right) \sin\left(\frac{\varphi_1 + \varphi_2}{2}\right). \tag{2.10}$$

Those are characterized by the junction critical current I_c and the phase difference $\varphi_{1,2}$ across the junction. In our case, we assume both junctions to have comparable parameters, and therefore equal critical currents.

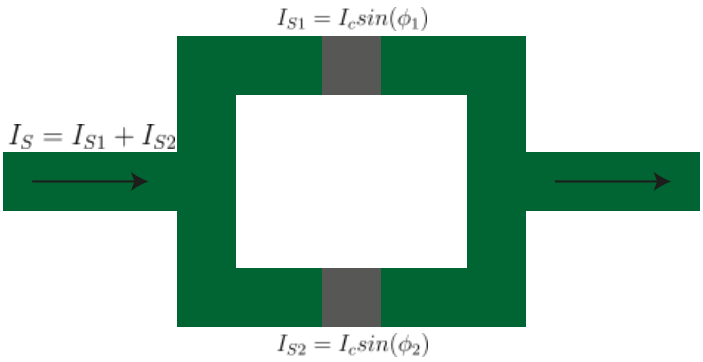

Figure 2.3: Schematic drawing of a SQUID. It consists of two superconducting branches (green), which are arranged in a loop. Each of them is interrupted by an insulating barrier (grey) and therefore forming a Josephson junction. The total supercurrent I_S splits up into I_{S1} and I_{S2}.

The most interesting property of a SQUID appears when penetrating the loop area with a magnetic field. The two phase differences become linked via the fluxoid quantization:

$$\varphi_2 - \varphi_1 = \frac{2\pi\Phi}{\Phi_0}, \tag{2.11}$$

where Φ is the magnetic flux inside the loop.

In general, the total flux inside the loop is given by $\Phi = \Phi_{\text{ext}} + \Phi_{\text{L}}$.
$\Phi_L = LI_{\text{cir}}$ results from a circulating current I_{cir} inside the loop. We define the so-called screening parameter β_L:

$$\beta_L = \frac{2LI_{\text{c}}}{\Phi_0}, \tag{2.12}$$

where L is the loop inductance. For our design, we have a small $\beta_L \ll 1$ and assume $\Phi \approx \Phi_{\text{ext}}$. If we now insert Eq. 2.11 into Eq. 2.10, we obtain the maximum supercurrent for $\sin\left(\varphi_1 + \pi\frac{\Phi}{\Phi_0}\right) = 1$,

$$I_{\text{s}}^{\text{m}} = 2I_{\text{c}} \left|\cos\left(\pi\frac{\Phi_{\text{ext}}}{\Phi_0}\right)\right|. \tag{2.13}$$

From Eq. 2.13, we see that, by arranging two Josephson junctions in a loop, we obtain a flux-tunable supercurrent. In transmon qubits, the transition frequency is related to the Josephson energy and therefore to the critical current. Using a SQUID instead of a single junction, the qubit transition frequency can be tuned by penetrating the loop with magnetic flux.

2.3 Transmission line theory

Now that we have described the nonlinear part of our circuit, we also have to consider the linear circuitry. In particular, this comprises a lumped-element circuit model and wave propagation on transmission lines, as well as microwave resonators and their properties. In the following, we rely strongly on Ref. [19].

2.3.1 The lumped-element circuit model

First of all, we show a lumped-element circuit model for transmission lines in general. These typically consist of two wires (Fig. 2.4). Here, R is the series resistance per unit length and L is the series inductance per unit length of both wires. Additionally, we find a shunt capacitance per unit length C between both conductors. Finally, a shunt conductance per unit length G exists, due to dielectric loss in the material between the wires (e.g. the substrate).

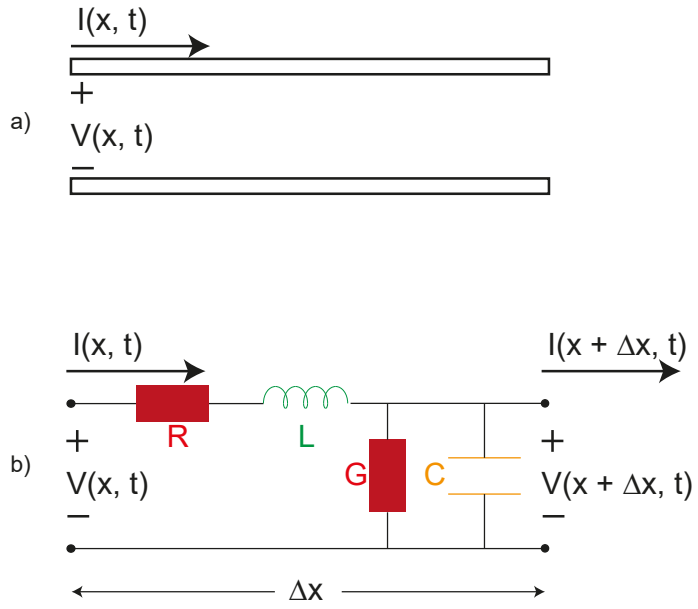

Figure 2.4: Equivalent circuit for a small piece of transmission line. (a) Voltage and current definitions. (b) Lumped-element circuit, where R is the series resistance and L the series inductance for both conductors per unit length. G and C represent the shunt conductance and capacitance per unit length, respectively.

After defining the circuit, we can now apply Kirchhoff's voltage law in order to obtain

$$V(x,t) - R\Delta x I(x,t) - L\Delta x \frac{\partial I(x,t)}{\partial t} - V(x+\Delta x, t) = 0. \tag{2.14}$$

From Kirchhoff's current law, it follows:

$$I(x,t) - G\Delta x V(x+\Delta x,t) - C\Delta x \frac{\partial V(x+\Delta x,t)}{\partial t} - I(x+\Delta x,t) = 0. \tag{2.15}$$

By dividing Eqs. 2.14 and 2.15 by Δx and by executing the limit $\Delta x \to 0$, we obtain the following differential equations:

$$\frac{\partial V(x,t)}{\partial x} = -RI(x,t) - L\frac{\partial I}{\partial t}, \tag{2.16}$$

$$\frac{\partial I(x,t)}{\partial x} = -GV(x,t) - C\frac{\partial V}{\partial t}. \tag{2.17}$$

Applying a Fourier transformation, we switch to the frequency domain:

$$\frac{dV(x)}{dx} = -(R + i\omega L)I(x), \tag{2.18}$$

$$\frac{dI(x)}{dx} = -(R + i\omega L)V(x). \tag{2.19}$$

Wave propagation on a transmission line

Solving the two Eqs. 2.18 and 2.19 simultaneously, we end up with two wave equations:

$$\frac{d^2V(x)}{dx^2} - \gamma^2 V(x) = 0, \tag{2.20}$$

$$\frac{d^2I(x)}{dx^2} - \gamma^2 I(x) = 0, \tag{2.21}$$

with

$$\gamma = \alpha + i\beta = \sqrt{(R + i\omega L)(G + i\omega C)} \tag{2.22}$$

being the complex propagation constant. Solving Eqs. 2.20 and 2.21, we can describe the voltage on the line by

$$V(x) = V_0^+ e^{-i\gamma x} + V_0^- e^{i\gamma x} \tag{2.23}$$

and the current by

$$I(x) = I_0^+ e^{-i\gamma x} + I_0^- e^{i\gamma x}. \tag{2.24}$$

Here, the $e^{-\gamma x}$ term accounts for wave propagation in the $+x$ direction, while the $e^{\gamma x}$ term accounts for the inverse direction. If we take the derivative of Eq. 2.23 with respect to x and insert Eq. 2.16, we can write the current along the line as:

$$I(x) = \frac{\gamma}{R + i\omega L}(V_0^+ e^{-i\gamma x} + V_0^- e^{i\gamma x}). \tag{2.25}$$

Next we define a characteristic impedance Z_0 as:

$$Z_0 = \frac{R + i\omega L}{\gamma} = \sqrt{\frac{R + i\omega L}{G + i\omega C}}, \tag{2.26}$$

which relates voltage and current by $Z_0 = \frac{V_0^+}{I_0^+} = \frac{-V_0^-}{I_0^-}$.

The lossless line

Our circuit is made of aluminum, which becomes superconducting below its critical temperature $T_c \approx 1.2$ K. Consequently, we neglect the series resistance R and the shunt conductance G, so that we obtain a purely real-numbered characteristic impedance:

$$Z_0 = \sqrt{\frac{L}{C}}. \tag{2.27}$$

2.3.2 Wave reflection and impedance mismatch

Wave reflection is an important problem concerning distributed-element systems. We assume an incident wave of the form $V_0^+ \mathrm{e}^{-i\gamma x}$ generated by a source at $x < 0$ and travelling in positive x-direction (Fig. 2.5). As we already know, the ratio of voltage and current is given by the characteristic impedance Z_0 of the line. For $x > 0$, we find a different characteristic impedance $Z_1 \neq Z_0$.

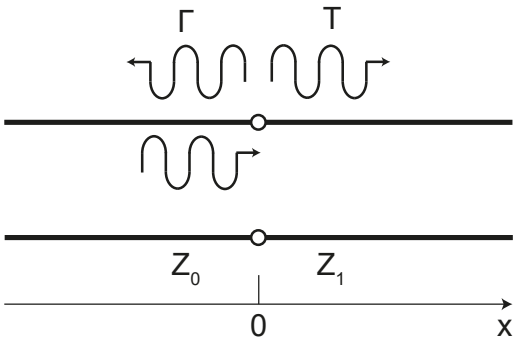

Figure 2.5: Wave reflection Γ and transmission T between two transmission lines with different impedances Z_0 ($x < 0$) and Z_1 ($x > 0$).

If the wave now reaches $x = 0$, a reflected wave must be excited, in order to fulfill the conditions for Z_1. So we can write the total voltage (according to Eq. 2.23) for $x < 0$ as:

$$V_0^+ e^{-i\gamma x} + V_0^- e^{i\gamma x} \tag{2.28}$$

and the current (similar to Eq. 2.24) as:

$$I(x) = \frac{V_0^+}{Z_0} e^{-i\gamma x} - \frac{V_0^-}{Z_0} e^{i\gamma x}. \tag{2.29}$$

At $x = 0$, the voltage and current are related by the impedance Z_1, so we get:

$$Z_1 = \frac{V(0)}{I(0)} = \frac{V_0^+ + V_0^-}{V_0^+ - V_0^-} Z_0. \tag{2.30}$$

Rewriting gives

$$V_0^- = \frac{Z_1 - Z_0}{Z_1 + Z_0} V_0^+. \tag{2.31}$$

The voltage reflection coefficient Γ describes the ratio of voltage amplitude of the incident wave to the reflected one:

$$\Gamma = \frac{V_0^-}{V_0^+} = \frac{Z_1 - Z_0}{Z_1 + Z_0}. \tag{2.32}$$

From the reflection coefficient, we can express an insertion loss IL in dB as:

$$IL = -20 \log |T| \, \mathrm{dB}, \tag{2.33}$$

where the transmission coefficient T is given by $T = 1 + \Gamma$.

2.3.3 Microwave resonators

One important part of our circuit are microwave resonators. They have many applications, such as storage of photons, coupling between qubits or readout of a qubit state. During this work, we focus on planar resonators used for the latter application. One way to realize such a microwave resonator is the coplanar waveguide geometry (Fig. 2.6). Here, we have an inner conductor in the middle, separated by two gaps from the ground planes. Those ground planes serve as our second conductor from Fig. 2.4. Note, that the characteristic impedance Z_0 now only depends on the strip width w, the gap spacing g, the substrate thickness and dielectric constant ϵ_r.

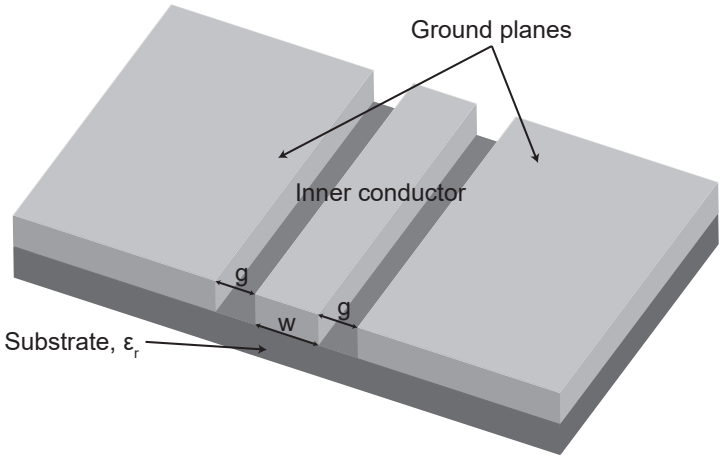

Figure 2.6: Geometry of a coplanar waveguide (not to scale). A microstrip of width w is separated from the ground planes by two gaps of width g.

Parallel resonant circuit

Near resonance, a microwave resonator can be described by either a series or parallel *RLC* equivalent circuit. In our work, we focus on the parallel resonance type (Fig. 2.7).

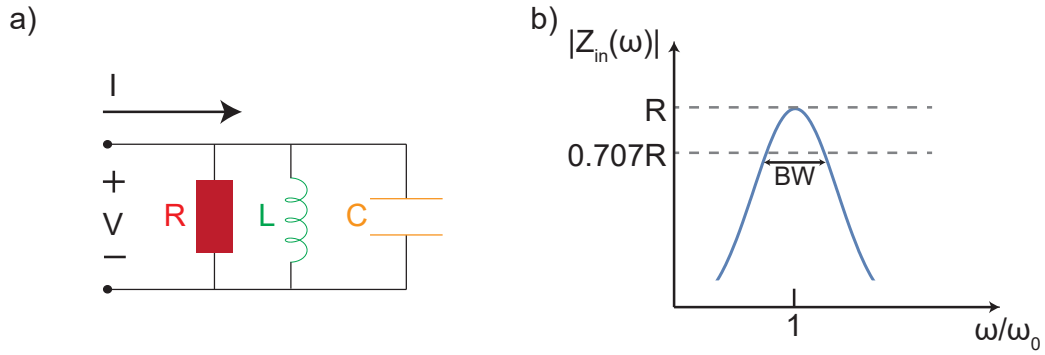

Figure 2.7: (a) A parallel resonant circuit. (b) Input impedance magnitude versus frequency.

As already mentioned, we are mostly interested in the quality factor Q. One can generally define it via

$$Q = \omega \frac{\text{average energy stored}}{\text{energy loss/second}} = \omega \frac{W_\text{m} + W_\text{e}}{P_\text{loss}}. \tag{2.34}$$

The average electric energy stored in the capacitor C is

$$W_\text{e} = \frac{1}{4}|V|^2 C \tag{2.35}$$

and the average magnetic energy stored in the inductor L is

$$W_\text{m} = \frac{1}{4}|I_\text{L}|^2 L. \tag{2.36}$$

Resonance occurs, when $W_\text{e} = W_\text{m}$. Then from Eqs. 2.35 and 2.36 we can write the resonance frequency ω_0 as

$$\omega_0 = \frac{1}{\sqrt{LC}}. \tag{2.37}$$

Consequently, the internal quality factor Q_i (ignoring external loading effects), can be written as

$$Q_\text{i} = \omega_0 \frac{2W_\text{m}}{P_\text{loss}} = \frac{R}{\omega_0 L} = \omega_0 RC, \tag{2.38}$$

We can define a bandwidth (BW) as

$$BW = \frac{\omega}{Q_\mathrm{i}}. \tag{2.39}$$

BW is also called the full width at half maximum (FWHM). In reality, the resonator is invariably coupled to other circuitry, which will lower the overall (loaded) quality factor Q_l of the circuit. Therefore we define an external quality factor Q_e, as

$$Q_\mathrm{e} = \frac{R_\mathrm{L}}{\omega_0 L} \tag{2.40}$$

for parallel circuits. Here, R_L is an external load resistor, which couples to our resonator. Finally, we can express the loaded quality factor as

$$\frac{1}{Q_\mathrm{l}} = \frac{1}{Q_\mathrm{e}} + \frac{1}{Q_\mathrm{i}}. \tag{2.41}$$

Short-circuited $\lambda/4$-line

In order to realize a parallel resonant circuit, we fabricate short-circuited $\lambda/4$-resonators. Here, one end of the inner conductor is short-circuited with the ground plane, while we have an open circuit on the other end. Consequently, we have a current maximum (and zero voltage) at the short and a voltage maximum (and zero current) at the open end as shown in Fig. 2.8.

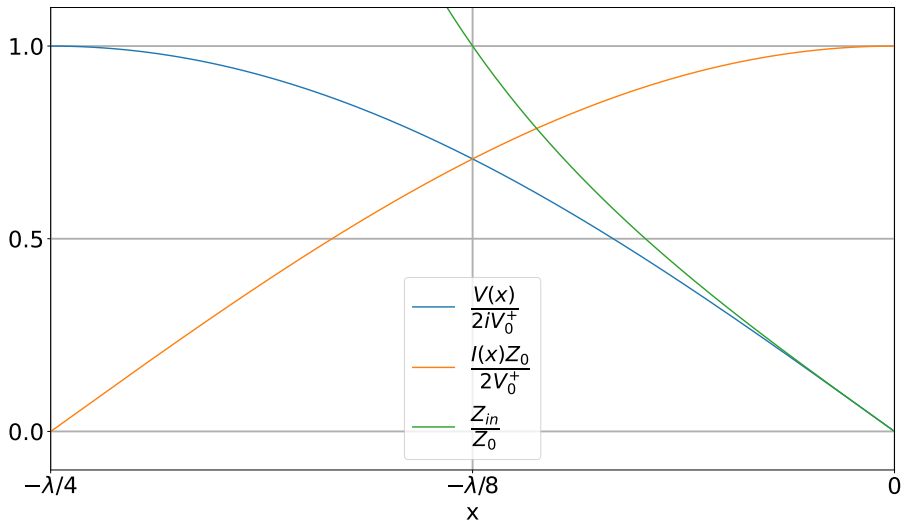

Figure 2.8: Voltage (blue line), current (orange line) and impedance ($R_{in} = 0$ or ∞, green lines) variation for the fundamental mode along a short-circuited transmission line.

The resonance frequency of the fundamental mode of a $\lambda/4$-resonator is given by:

$$f_0 = v_{\text{ph}}/\lambda = \frac{c}{\sqrt{\epsilon_{\text{eff}}}4l}, \tag{2.42}$$

whith $v_{\text{ph}} = c/\sqrt{\epsilon_{\text{eff}}}$ the phase velocity, c the speed of light, ϵ_{eff} an effective dielectric constant. The length l of the resonator is chosen such that $l = \frac{\lambda}{4}$.
We can express the impedance across the resonator by:

$$Z(l) = Z_0 \frac{Z_l + Z_0 \tanh(\gamma l)}{Z_0 + Z_l \tanh(\gamma l)}. \tag{2.43}$$

Assuming $\alpha l \ll 1$ for small loss and $\Delta\omega \ll \omega_0$ for a small frequency range we can write the resonator's input impedance as

$$Z_{\text{in}} \approx \frac{Z_0}{\alpha l + i\pi\Delta\omega/2\omega_0}. \tag{2.44}$$

2.4 Continuous wave measurement and internal quality factor extraction

The most important part of a continuous-wave measurement setup is a vector network analyzer (VNA). It serves as both a generator and a detector for microwave signals, and allows one to extract the scattering parameters of a circuit. Since the resonators fabricated during the course of this thesis are coupled to a transmission line across the sample, we are interested in transmission measurements. In Fig. 2.9, we illustrate such a measurement for an arbitrary two-port circuit. Here, each port of the circuit (1 and 2) is connected to one port of a VNA (A and B). When we create a microwave in port A, we can detect the transmitted wave in port B.

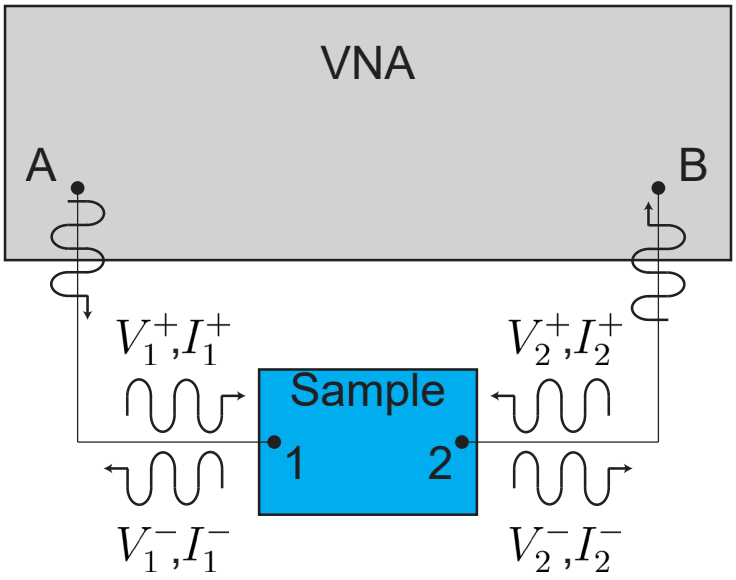

Figure 2.9: Scheme of a circuit with two ports 1 and 2, which is connected to a VNA. In order to measure the transmission through the sample, we can create microwaves in port A of the VNA while port B is used for detection.

Using the idea of incident, transmitted and reflected waves, we can describe such a system with the scattering matrix $[S_{ij}]$ by [19]:

$$\begin{bmatrix} V_1^- \\ V_2^- \end{bmatrix} = \begin{bmatrix} S_{11} & S_{12} \\ S_{21} & S_{22} \end{bmatrix} \begin{bmatrix} V_1^+ \\ V_2^+ \end{bmatrix}. \tag{2.45}$$

Any specific element of the scattering matrix is given by:

$$S_{ij} = \left. \frac{V_i^-}{V_j^+} \right|_{V_k^+ = 0 \text{ for } k \neq j}. \tag{2.46}$$

In practice, many microwave networks consist of a cascaded connection of two or more two-port networks. In this case we can define a 2×2 transmission matrix (also called *ABCD* matrix). Our network can then be described as [19]:

$$\begin{bmatrix} V_1 \\ I_1 \end{bmatrix} = \begin{bmatrix} A & B \\ C & D \end{bmatrix} \begin{bmatrix} V_2 \\ I_2 \end{bmatrix}. \tag{2.47}$$

Measurement of internal and coupling quality factors in the ideal case

In our samples, we couple $\lambda/4$ notch-type resonators capacitively to a transmission line, as illustrated in Fig. 2.10. In order to obtain the quality factors, we measure the transmission through the line, i. e., the ratio $\frac{V_2^-}{V_1^+} = S_{21}$ for an incident wave from port A. Note that in this case $V_2^+ = 0$. The transmission matrix can be written as $A = D = 1, B = 0$ and $C = 1/Z$ with $Z = 1/i\omega C_c + Z_r$. Note, that the coupling might also be partially inductive. However, the inductance is usually small and can therefore be neglected.

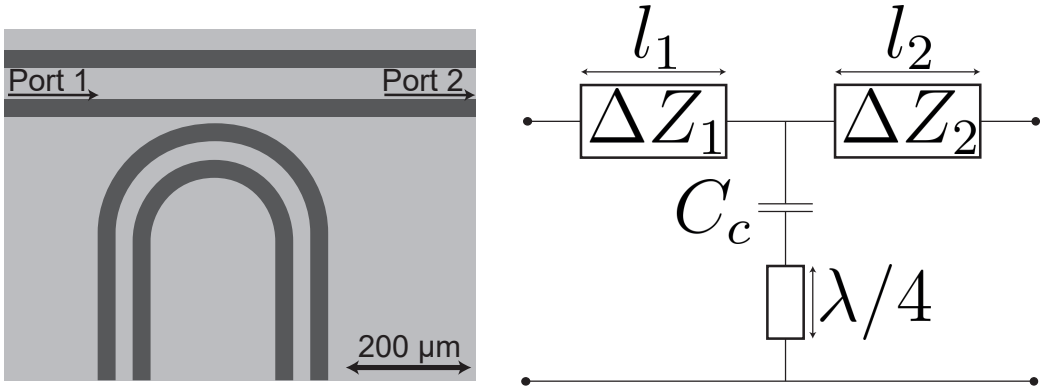

Figure 2.10: Schematic of a notch-type CPW resonator. The short-circuited $\lambda/4$ resonator is coupled to the transmission feedline by the coupling capacitance C_c.

We consider first a lossless resonator (with resonance frequency ω_0) and calculate then the resonance frequency ω_r for the whole system, similar to Refs. [20] and [21]. The resonance frequency of the resonator is shifted due to the coupling to the transmission line. For $\mathrm{Im}(Z) = 0$, resonance occurs and we obtain

$$\omega_r \approx \omega_0 - \frac{2Z_0 C_c \omega_0^2}{\pi}, \tag{2.48}$$

as long as $Q_i \gg \sqrt{\pi Q_e/8}$, where $Q_e = \pi/(2Z_0^2\omega_r^2C_c^2)$. This is always true for commonly used CPW resonators.
Under this condition, the input impedance near the resonance frequency can be written as:

$$Z \approx \frac{Z_0 Q_e}{2Q_i}(1 + i2Q_i\delta x), \tag{2.49}$$

where $\delta x = (\omega - \omega_0)/\omega_0$. Finally, the scatterig matrix reads

$$S_{11} = S_{22} \approx -\frac{Q_l/Q_e}{1 + i2Q_l\delta x}, \tag{2.50}$$

$$S_{21} = S_{12} \approx 1 - \frac{Q_l/Q_e}{1 + i2Q_l\delta x}. \tag{2.51}$$

Influence of small circuit asymmetry

However, in real measurements, we have to consider a small circuit asymmetry, ΔZ_1 and ΔZ_2, on both sides of the feedline coupled to the resonator. We obtain a new transmission matrix with $A = 1 + \Delta Z_1/Z$, $B = \Delta Z_1 + \Delta Z_2 + \Delta Z_1\Delta Z_2/Z$, $C = 1/Z$, $D = 1 + \Delta Z_2/Z$ [19]. For that case, the scattering matrix element S_{21} reads

$$S_{21} \approx 1 - \frac{Q_l'/Q_e'}{1 + i2Q_l'\delta x}, \tag{2.52}$$

where we have assumed $\Delta Z_1, \Delta Z_2 \ll Z_0$. Due to the asymmetry, the loaded quality factor becomes $1/Q_l' = 1/Q_i + 1/Q_e'$ where $Q_e' = Q_eZ_0(1/Z_1 + 1/Z_2)/2$, $Z_1 = Z_0 + \Delta Z_1$ and $Z_2 = Z_0 + \Delta Z_2$. Using this definition, both Q_l' and Q_e' could become complex.
However, as we only consider small asymmetry, the real parts in Z_1 and Z_2 should dominate. Therefore, we redefine the loaded quality factor as $1/Q_l' = 1/Q_i + \mathrm{Re}(1/Q_c')$ [22]. In conclusion, the scattering matrix element S_{21} becomes

$$S_{21} \approx 1 - \frac{e^{i\phi}Q_l'/|Q_e'|}{1 + i2Q_l'\delta x}. \tag{2.53}$$

Influence of the finite-length feedlines

Apart from circuit asymmetry, also the finite length of the feedline can influence the measurement. We recall the expressions of incident and reflected voltages at position l:

$$V^+(l) = V_0^+ \mathrm{e}^{-\gamma l} \tag{2.54}$$

$$V^-(l) = V_0^- \mathrm{e}^{+\gamma l}, \tag{2.55}$$

with $\gamma = \alpha + i\beta$. Now we assume two feedlines coupled to the resonator with length l_1 , $l_2 \neq 0$. It follows, that

$$V_1^{\pm'} = \mathrm{e}^{\pm\gamma l_1} V_1^{\pm}, V_2^{\pm'} = \mathrm{e}^{\pm\gamma l_2} V_2^{\pm} \tag{2.56}$$

and for the scattering matrix

$$S_{21}^{'} = \mathrm{e}^{-(\gamma_1 l_1 + \gamma_2 l_2)} S_{21}. \tag{2.57}$$

Note that this procedure assumes that the impedances of the feedline match the resonator's impedance. In general, mismatched lines can also cause an asymmetry.
Under a high-frequency approximation and assuming low loss, we have α being constant and $\beta \approx \omega\sqrt{l_\mathrm{r} c_\mathrm{r}}$ being frequency-dependent. Here, l_r and c_r are the inductance and capacitance of the CPW per unit length. We see, that a finite length of the feedlines might cause a damping coefficient, as well as a frequency-dependent phase in the scattering coefficients. Further, an imperfect instrument calibration and the influence of microwave devices (e. g. amplifiers or attenuators) could create a phase delay.
In total, we obtain a model, which describes the transmission coefficient of our notch-type resonators

$$S(\omega) \approx \alpha \mathrm{e}^{-i(\tau\omega+\varphi)} \left(1 - \frac{\mathrm{e}^{i\phi} Q_\mathrm{l}/|Q_\mathrm{e}|}{1 + 2iQ_\mathrm{l}(\omega/\omega_0 - 1)}\right). \tag{2.58}$$

Here, $\tau\omega + \varphi$ represents a frequency-dependent phase shift.

The circuit fitting procedure

With the expression given in Eq. 2.58, a fitting method to the data has been developed in order to obtain the external and internal quality factors from the scattering responses [23], [24]. For our measurements, we use a python script, originally written by Qi-Ming Chen, which we have adapted to suite our specific setup. The circuit-fitting procedure has been summarized by Chen et al. in Ref. [25] and works as follows.

Fit a circle to the measured response

The non-zero length of the feedlines can cause a frequency-dependent phase in the scattering coefficients. We directly observe this phase shift in Fig. 2.11 and 2.13, where the expected circle is deformed. Consequently, to fit a circle properly, we must correct the phase shift. We split this procedure into the following three steps:

1. Rough phase correction with linear fit
2. Data selection with Lorentzian fit
3. Fine phase correction with circle fit

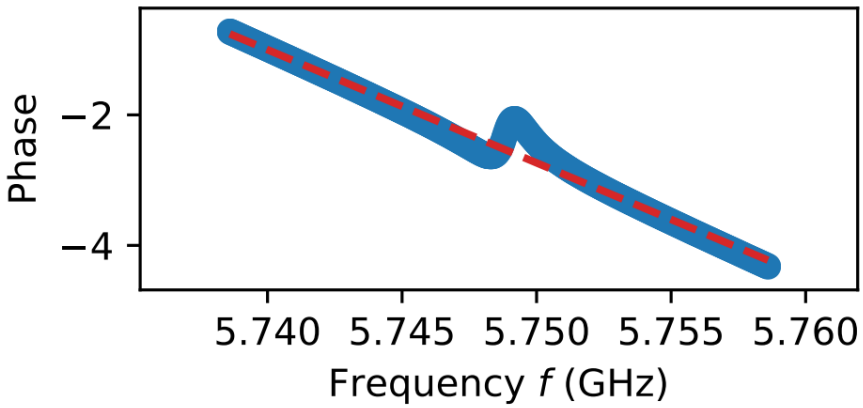

Figure 2.11: Step 1: Measured phase vs. frequency of resonator 1 on sample Res-035. Blue points show data points, while the red dashed curve shows the linear fit.

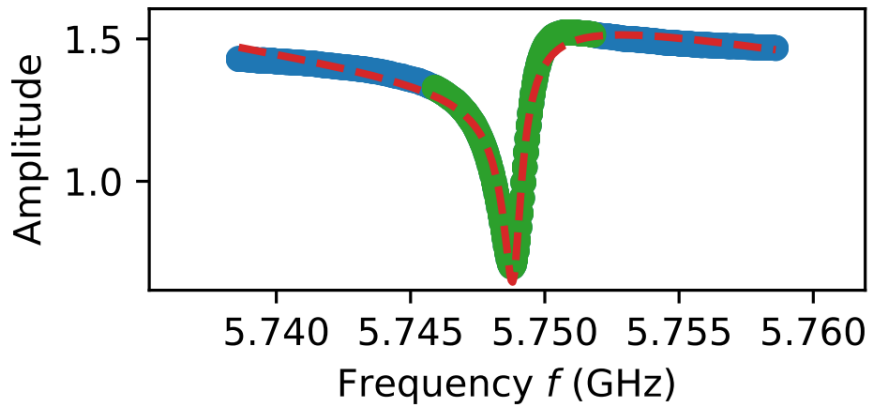

Figure 2.12: Step 2: Measured relative voltage amplitude vs. frequency of resonator 1 on sample Res-035. Amplitude A is calculated by $A = 10^{P/20}$, where P is the measured power in dBm. The Blue points show data points, while the red dashed curve shows the lorentzian fit. Green points indicate the selected data within the range $\pm 5 \cdot \Delta\omega_{3\text{dB}}$ around the resonance frequency, where $\Delta\omega_{3\text{dB}}$ is the FWHM.

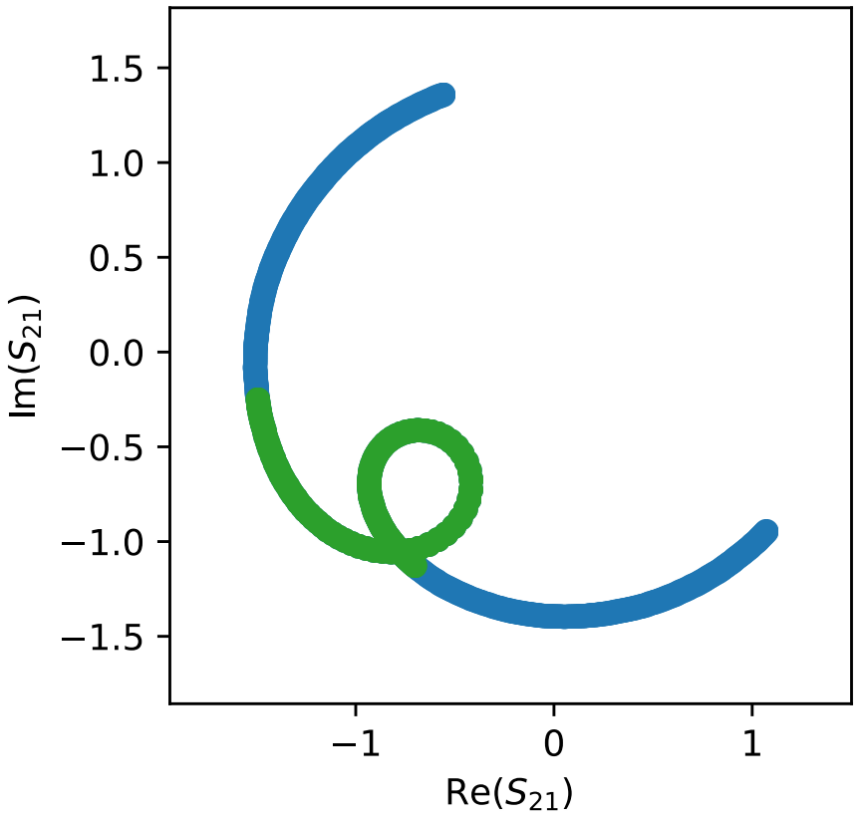

Figure 2.13: Imaginary part of S_{21} vs. its real part. Blue points show all data points, while the green dots represent the data chosen during the Lorentz fit. Due to the phase shift, the circle is slightly deformed.

Step 1: First of all, we fit a linear function to extract the frequency-dependent phase. The fitting function reads

$$J_1 = \{-(\tau\omega + \varphi - \angle S(\omega)\}^2, \tag{2.59}$$

by defining τ and φ as fitting parameters. Here, $\angle S(\omega)$ is the unwrapped phase of the complex signal. The fit is shown in Fig. 2.11. When fitting a circle in the third step, the extracted fit parameters are used as the initial guess of the frequency-dependent phase coefficient.

Step 2: In the ideal case, the data within the full width at half maximum (FWHM) of the amplitude can form a half circle. In order to minimize the influence of the background, we remove the far off-resonant data. Hereby, we use a Lorentzian fit to obtain roughly the resonance frequency ω_r and the FWHM $\Delta\omega_{3dB}$. Then, we only keep data around the resonance frequency within the range $\pm 5 \cdot \Delta\omega_{3dB}$. For some measurements, we need to increase that range so the fit converges.

The objective funciton to be minimized is [23]

$$J_2 = \left[\left(A_1 + A_2 f + \frac{A_3 + A_4 f}{\sqrt{1 + 4\left(\frac{\omega - \omega_r}{\Delta\omega_{3dB}}\right)^2}} \right) - |S(\omega)| \right]^2 , \tag{2.60}$$

with A_1 - A_4 being fit parameters. The results are shown in Fig. 2.12. The green dots in Fig. 2.12 and 2.13 are the selected data within the chosen bandwidth.
Step 3: Now that we have an initial guess for the parameter τ and have removed the far off-resonant data, we apply an optimization algorithm to fit a circle to the selected data. We use the algorithm described in Ref. [24]. Here, we use an algebraic method to determine the center S_c and the radius r_c [26]. At the same time, we keep adjusting the parameter τ according to

$$J_3 = \left(r_c - \left| e^{i\tau\omega} S(\omega) - S_{c1} \right| \right)^2 . \tag{2.61}$$

This way, the updated data $S_1(\omega) = e^{i\tau\omega} S(\omega)$ is more likely to be a circle. Figure 2.14 shows the corrected data $S_1(\omega)$ (green) and the fitted circle (red dashed).

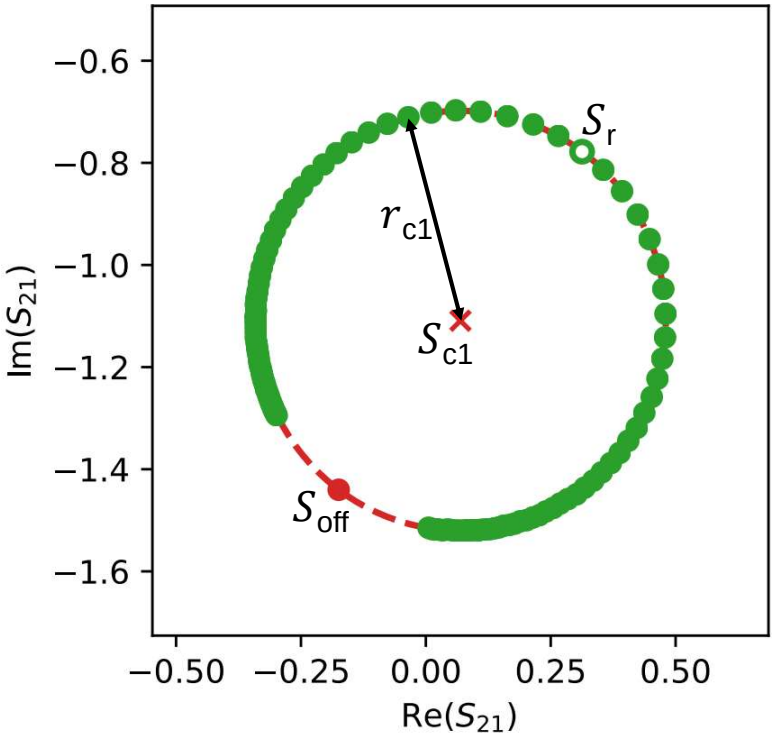

Figure 2.14: Step 3: Updated data of the imaginary part of S_{21} vs. its real part. S_r and S_{off} are filled with white or red colors, respectively. Also, the circle center S_{c1} and the radius r_{c1} are shown.

Transform the circle to the canonical form

Now that we have fitted a circle, we transform it into the canonical form described by Eq. 2.53. We know, that for an ideal measurement, the response intersects with the real axis at the position $1 + i0$ for $\omega \to \infty$. The transformation can be split into the following three steps:

1. Resonant frequency determination with phase versus frequency fit
2. Cable attenuation and frequency-independent phase correction
3. Asymmetry correction

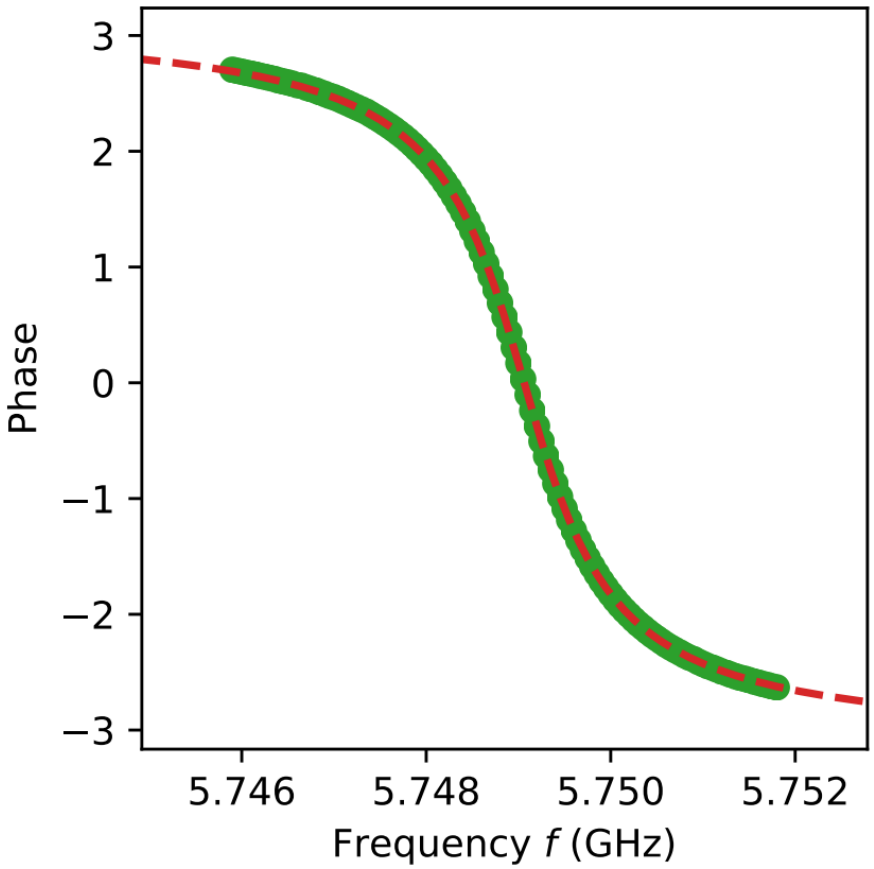

Figure 2.15: Step 1: Determination of resonance frequency by fitting phase vs. frequency.

Step 1.: With regard to the circle center S_{c1}, the far off-resonant point should be symmetric to the on-resonant point S_r, i. e., $S_{off} = S_{c1} + (S_{c1} - S_r)$. Therefore, we use the phase versus frequency fit to determine the position of S_r and S_{off} [23]. The objective function reads

$$J_4 = \left\{ \theta_0 + 2 \arctan\left[2Q_l \left(1 - \frac{\omega}{\omega_r} \right) \right] - \arg[S(\omega)] \right\}^2, \tag{2.62}$$

with θ_0 being an offset phase, resonance frequency ω_r and the loaded quality factor Q_l as fitting parameters. The red curve in Fig. 2.15 shows the results from the fit, which allows us to determine Q_l and ω_r. We can also locate S_r and S_{off}. They are shown in Fig. 2.14.

Step 2: Now that we know the position of S_{off}, we can remove cable attenuation and frequency-independent phase shift by using

$$S_2(\omega) = S_1(\omega)/S_{off}. \tag{2.63}$$

Fig. 2.16 shows the corrected data $S_2(\omega)$. Here, the off-resonant point intersects with the real axis at $1 + i0$. The circle center is also transformed to the new position $S_{c2} = S_{c1}/S_{off}$ and the new circle radius is given by $r_{c2} = r_{c1}/|S_{off}|$.

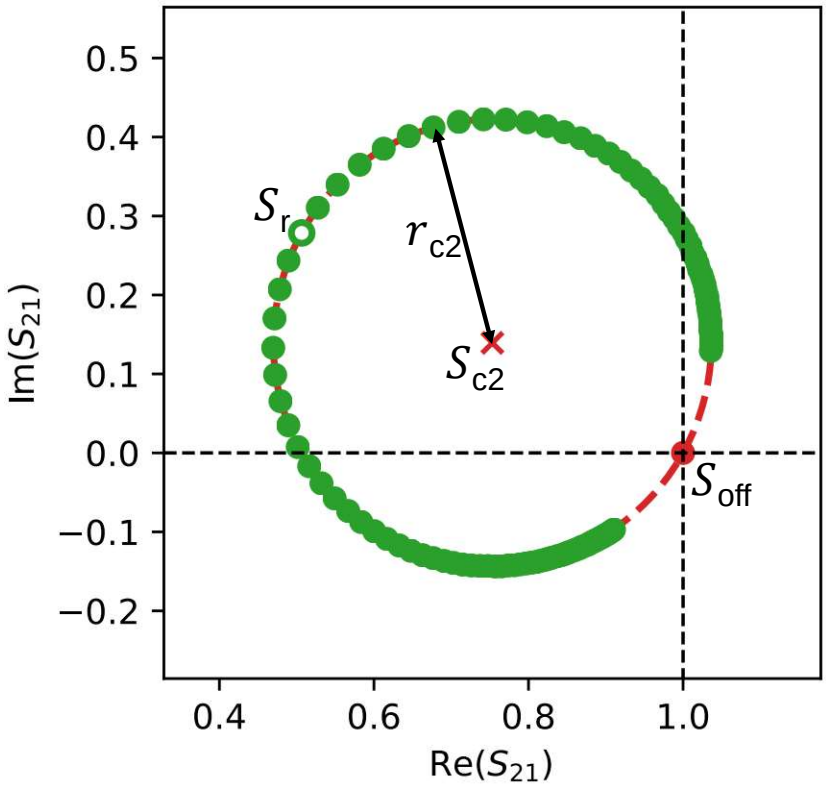

Figure 2.16: Step 2: Corrected data $S_2(\omega)$. Here, we remove cable attenuation and frequency-independent phase shift and the off-resonant point S_{off} intersects with the real axis at $1 + i0$

Step 3: As last step, we correct the asymmetry in the scattering coefficient. As S_{c2} should be on the real axis without asymmetry, we identify ϕ by

$$\phi = \angle(S_{c2} - S_{off}) - \pi, \tag{2.64}$$

and perform a rotation of the circle around the off-resonant point $1 + i0$. Meanwhile, the circle radius is rescaled by a factor $\cos(\phi)$ to account for a difference in $|Q_c|$ and $\mathrm{Re}(Q_c)$ [22]. The total transformation is described by

$$S_3(\omega) = (S_2(\omega) - 1)\, e^{-i\phi} \cos(\phi) + 1. \tag{2.65}$$

The final result is shown in Fig. 2.17. Finally, the internal quality factor can be obtained by

$$Q_i = \frac{Q_l}{1 - 2r_{c3}}, \tag{2.66}$$

where $\mathrm{Re}(Q_e) = Q_l/(2r_{c3})$.

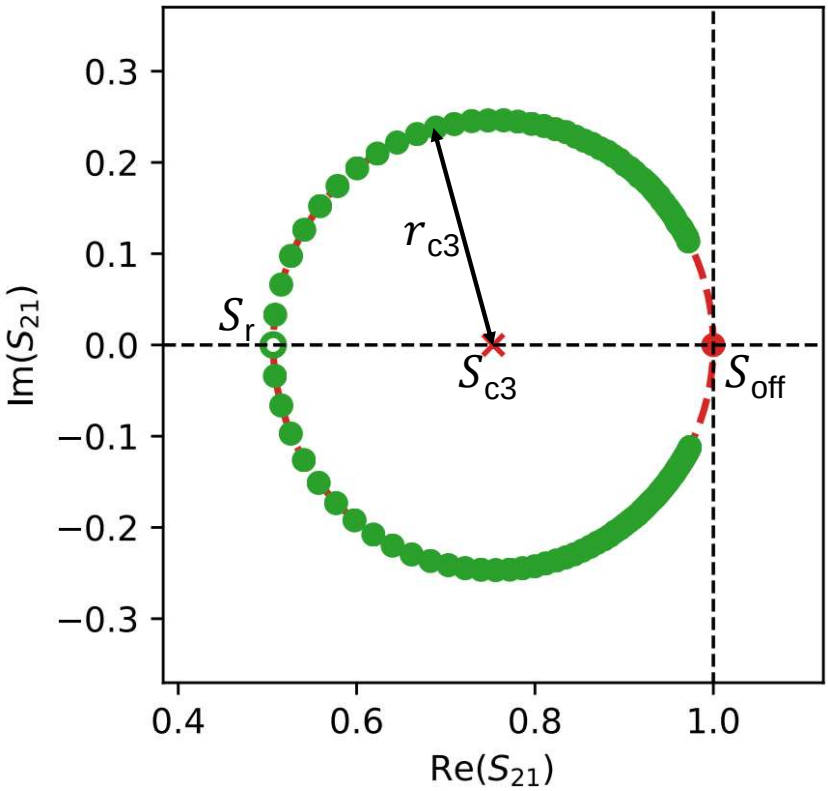

Figure 2.17: Step 3: Rotation of the circle, so the circle center is located on the real axis. At the same time the circle radius is rescaled by a factor of $\cos(\phi)$ in order to account for a difference in $|Q_c|$ and $\mathrm{Re}(Q_c)$ [22].

2.5 Loss mechanisms in superconducting thin film resonators

In order to analyze a resonator, we calculate the internal loss $\delta_i = 1/Q_i$ (with $\tan \delta_i$ being the well known loss tangent) from a transmission measurement. The internal quality factor is obtained by using the procedure described in Sec. 2.4.
Generally, the CPW geometry influences all loss channels. For a fixed gap g, the loss decreases with $w^{-2/3}$ for $w \leq g$ and saturates for $w \geq g$. Scaling up the CPW geometry, the fraction of the electric energy in two-level systems (TLSs) decreases [11]. On the other hand, for larger widths other loss contributions, such as radiation and trapped flux in the center strip increase. However, for a fixed geometry, a characteristic impedance $Z_0 = 50 - 60\ \Omega$ minimizes the total internal loss [27].

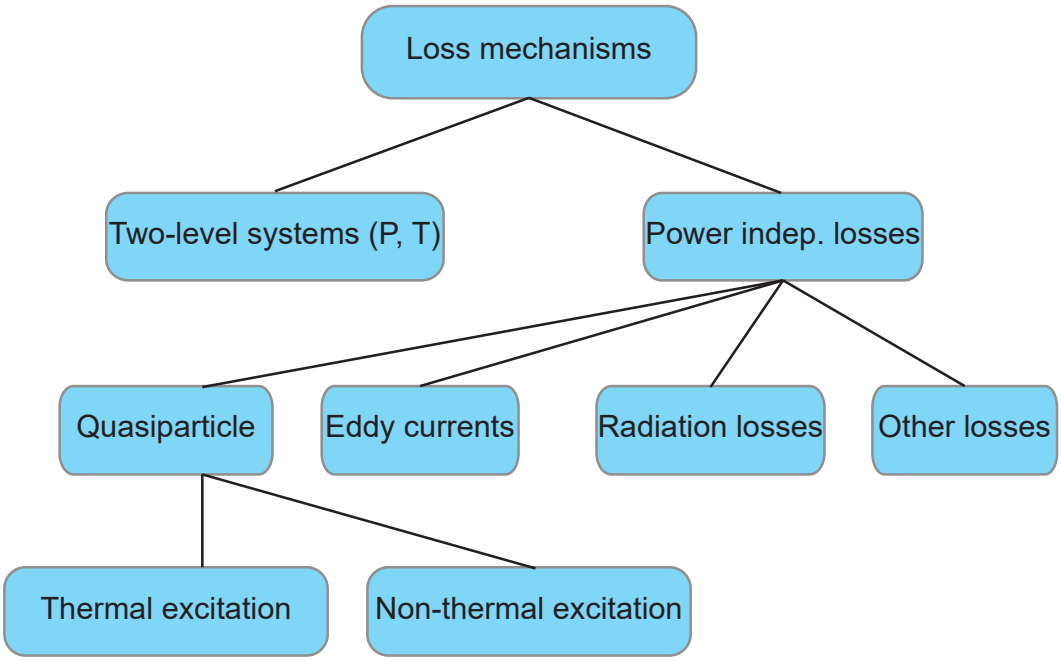

Figure 2.18: Different loss contributions. By varying input power and temperature, we can extract TLS and quasiparticle losses from the measured total losses. [28]

We want to have a deeper look into different loss mechanisms and their origin. An overview over different loss contributions is given in Fig. 2.18. Therefore, we follow the analysis of Ref. [28]. As first step, we split the internal loss into power independent losses δ_c and TLS losses $\delta_{TLS}(P_r, T)$:

$$\delta_i(P_r, T) = \delta_{TLS}(P_r, T) + \delta_c. \tag{2.67}$$

Further, power independent losses can be split into quasiparticle losses δ_{qp}, eddy currents $\delta_s(h)$, radiation losses δ_{rad} and other loss channels δ_{other}:

$$\delta_c(T, h) = \delta_{qp}(T) + \delta_0, \tag{2.68}$$

with $\delta_0 = \delta_s(h) + \delta_{rad} + \delta_{other}$.

2.5.1 Two-level system losses

A significant loss source in superconducting circuits are so-called two-level systems (TLSs) in the dielectrics, interfaces and surface oxides. Generally, at low powers, the loss decreases with temperature down to ≈ 2 K. However, for even lower temperatures loss increases again as temperature decreases. This behavior can be attributed to polar molecules or impurities with electric dipole moments, that act as TLSs [29]. Due to the high crystal quality of the used substrates, the TLS loss doesn't predominantly origin from the bulk substrate, but rather from surfaces or interfaces [11].
There are three types of amorphous interfaces in thin film resonators, that can contain TLSs:

- Metal-air
- Metal-substrate
- Substrate-air

Simulations and experiments have shown, that the dominant losses come from either the metal-substrate interface, or the substrate-air interface [27].
The losses due to two-level fluctuators, coupling to electric fields in our resonators, can be calculated by:

$$\delta_{TLS}(P_r, T) = \delta^0_{TLS} \frac{\tanh(\hbar\omega_r / 2k_B T)}{\sqrt{1 + (P_r/P_c)^{\beta/2}}}, \tag{2.69}$$

where $P_r = P_{in} Q_l^2 / n\pi Q_e$ is the power circulating inside the resonator for the n-th mode and P_{in} the input power.

P_c is a temperature dependent characteristic power of TLS saturation and can be approximated as [28]:

$$P_c(T) = \frac{3\hbar\epsilon}{2d^2\tau_1(T=0)\tau_{ac}} \coth\left(\frac{\hbar\omega_r}{2k_B T}\right) T^{\alpha}. \tag{2.70}$$

Here, d is the effective dipole moment of the TLSs, τ_1 represents the relaxation time of the TLSs and τ_{ac}^{-1} describes the TLS coupling rate to acoustic phonons. β is a design-dependent parameter. For a fixed temperature, δ_{TLS} is maximized in the low power limit ($P_r < P_c$). On the other hand, TLS losses decrease by having a high power circulating in the system. Here, the bath of TLS is then saturated by the large amount of photons [30].

2.5.2 Quasiparticle losses

Another loss participation comes from quasiparticle generation due to stray infrared light. Usually the main source of this radiation is the 4 K stage of a dilution refrigerator, and can thereby be seen as 4.2 K black-body radiation. This radiation loss δ_{rad}^{qp} depends on quasiparticle density n_{qp} and resonator frequency f_r [31]:

$$\delta_{rad}^{qp} = \frac{\gamma}{\pi}\sqrt{\frac{2\Delta}{hf_r}}\frac{n_{qp}}{D(E_F)\Delta}. \tag{2.71}$$

where Δ is the superconducting energy gap and $D(E_F)$ the two-spin density of states. The infrared light can enter the sample mount through connectors and lid joint. The rate equation for the total number of quasiparticles can be written as [32]:

$$\frac{\partial N_{qp}}{\partial t} = \frac{P}{\Delta} + G - RN_{qp}^2, \tag{2.72}$$

where P is the absorbed power for which $hf > 2\Delta$, G the standard thermal generation term due to pair breaking by phonons, and R a material-dependent recombination constant. The light-induced density exceeds the thermal background under strong loading and the quasiparticle density scales as $n_{qp} \propto \sqrt{P/\Delta}$. For aluminum, we find a gap frequency $f_{gap} = 2\Delta/h \approx 87$ GHz. Hence, the majority of the power of a black-body radiator at 4.2 K can be absorbed (See App. A.1).
Additionally, thermally induced quasiparticle losses δ_{qp} usually become dominant, when the sample temperature exceeds approximately 10% of the critical temperature

T_c. We describe these losses with the Matthis-Bardeen theory [33], [34]

$$\delta_{qp} = \frac{2\gamma}{\pi} \frac{e^{-\zeta} sinh(\xi) K_0(\xi)}{1 - e^{-\zeta}(\sqrt{2\pi/\zeta} - 2e^{-\xi} I_0(\xi))}, \tag{2.73}$$

with γ being the ratio of kinetic to total inductance of the conductor, $\zeta = \Delta/k_B T$, and $\xi = \hbar\omega_r/2k_B T$. I_0 and K_0 are the modified Bessel function for the first and second kind, respectively.

2.5.3 Eddy current losses

The main source of Eddy currents $\delta_s(h)$ is the finite conductivity of the material on the backside of the substrate. The loss basically increases with decreasing substrate thickness. This thickness dependency arises due to a residual magnetic field on the backside. Consequently, a field H_s in the glue between sample box and substrate is present. According to Ref. [28] the loss is given as

$$\delta_s = \sqrt{\omega_r \mu/2\sigma_{\omega_r}}(1 + \epsilon_r) Z_0 K(h)^2 l/32(Z_{VAC} g)^2. \tag{2.74}$$

Here, σ_{ω_r} is the electrical conductivity at the resonator frequency, $Z_0 = 50\,\Omega$ and $Z_{vac} \approx 377\,\Omega$ is the vacuum impedance. $K(h)^2 = \int_{-\infty}^{\infty} k(y,h)^2 dy$ with $k(h,y)$ being the field distribution at $z = 0$ along the y-direction. l is the resonator length, g the gap width and $\epsilon_r = 11.9$ the relative dielectric constant of the Si substrate.

2.5.4 Radiation losses

Energy can also leak out of the resonator in the form of electromagnetic radiation. The loss mainly depends on material properties and resonator geometry [21].
Vayonakis originally calculated the radiation loss for a quarter wave resonator [35]:

$$\delta_{rad} = \frac{2\epsilon^{5/2}}{\pi(1+\epsilon)^2} \frac{Z_0}{Z_{vac}} I'(\epsilon, n)(n - \frac{1}{2}) \left(\frac{s}{l}\right)^2 \tag{2.75}$$

with n the mode number, $s = w + 2g$ and l being the resonator length. $I'(\epsilon, n)$ is

$$I'(\epsilon, n) = \int_{\theta=0}^{\pi/2} d\theta \int_{\phi=0}^{2\pi} d\phi \frac{\left(1 - \sin(\theta)^2 \cos(\phi)^2\right) \sin(\theta)^3 \sin(\phi)^2}{(\alpha^2 - 1)^2} \left[1 + \alpha^2 + 2\alpha(-1)^n \sin\left((n - \frac{1}{2})\alpha\pi\right)\right]. \tag{2.76}$$

Here, $\alpha = \sqrt{\frac{2\epsilon}{1+\epsilon}} \sin(\theta)\cos(\phi)$. For $\epsilon = 11.68$, one finds $I'(\epsilon, n = 1) = 1.615$.

2.5.5 Other losses

Besides the loss contributions discussed above, there are other sources of intrinsic loss. A good summary is given in Ref. [36]. In the following, we mention some of those other losses, but we do not analyze them in detail in this work.

In a superconducting film, vortices of trapped magnetic flux can form islands of normal metal and can thus dissipate power due to a current at the core of the vortex. A study of microwave response of vortices was carried out in Ref. [37].

Through hybridization with nearby low-Q modes, such as chip modes, box modes, and slotline modes, a resonators internal quality factor Q_i can be reduced.

Coplanar transmission lines lose energy due to radiation into surface-wave modes and the substrate [38], if the substrate's thickness is a considerable fraction of a surface-mode's wavelength.

Due to a small imaginary part in the superconducting gap, quasiparticles can be present inside the energy gap (intragap states). The surface resistance therefore deviates form the Mattis-Bardeen theory at low temperature, followed by a saturation of a resonator quality factor for decreasing temperature [39].

Chapter 3

Experimental techniques

Now that we have settled the theoretical foundation of our thesis, we want to present some experimental techniques, including sample fabrication, and our meaurement setups.
In particular, the sample fabrication consists of three steps, namely sample preparation, electron beam lithography and evaporation together with oxidation. First, we present the standard process in Sec. 3.1.
Second we present the setup for normal resistance measurements of SQUID loops, which allows us to analyze parameter dependency of our fabrication, e.g., charge dosis and chip position. Further, we can calculate the critical current density J_c using the Ambegaokar-Baratoff relation (Eq. 2.9), as well as an overall yield.
Finally, we show the cryogenic setup, which is used for transmission measurements of resonators.

3.1 Sample fabrication - standard process

The fabrication of superconducting nanostructures is challenging since it spans a huge parameter space. Our starting point is the current fabrication process of aluminum structures on silicon substrates ($6 \times 10\,\mathrm{mm}^2$) with high specific resistivity ($> 2\,\mathrm{k\Omega cm}$).

3.1.1 Sample preparation

Removal of protective resist

First of all, we need to remove the protective resist on top of the substrate (Fig. 3.1). This resist is usually applied in order to avoid damage during wafer dicing.

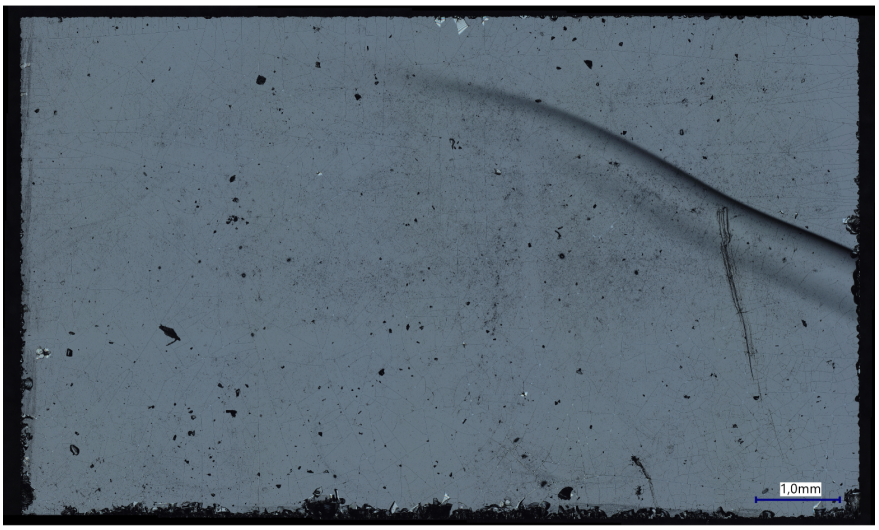

Figure 3.1: A typical silicon substrate ($6 \times 10\,\mathrm{mm}^2$) with protective resist on top.

For the standard process (Fig. 3.2), we put the sample into a bath of acetone and heat it at 70 °C for 10 minutes. After a second iteration of this step, we switch to a bath of isopropylic alcohol (or isopropanol, IPA) and put the sample into a supersonic bath (power level 9) for 2 minutes. Afterwards we blow the chip dry with nitrogen.

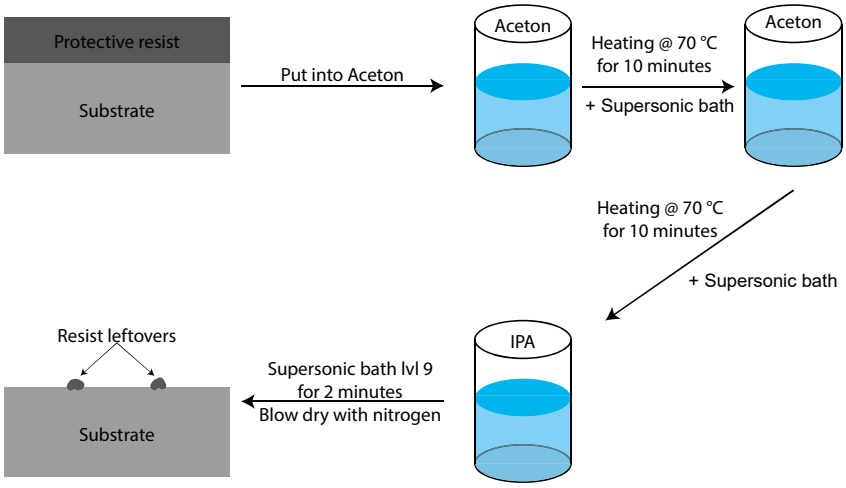

Figure 3.2: Standard cleaning process. First, we heat the sample twice in acteone baths at 70 °C for 10 minutes, followed by a supersonic bath for 2 minutes. Afterwards we perform a supersonic bath for 2 minutes in isopropanol (IPA).

Spin coating

Next, we apply a two-layer resist system onto the sample (Fig. 3.3). For the bottom layer, we apply 440 µl of PMMA/MA 33% and spin it at 2000 rotations per minute (R.P.M.) for 120 s. Afterwards, we bake the substrate at 160 °C for 10 minutes. For the top resist, we repeat this step with 220 µl of PMMA 950K and 4000 R.P.M. Afterwards, we place some gold nanoparticles close to the substrate edges, which are needed for the next fabrication step.

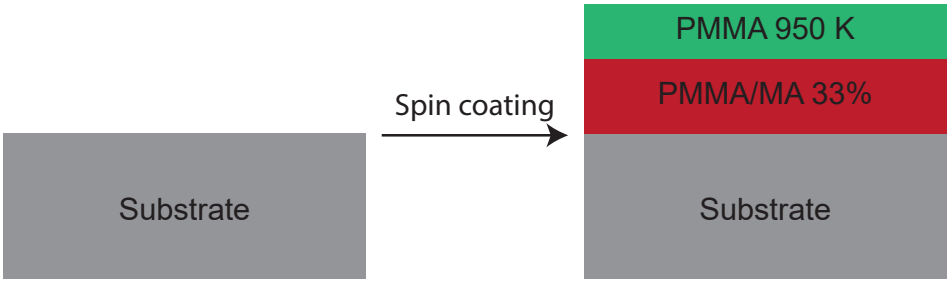

Figure 3.3: Schematic of the spin coating process.

3.1.2 Electron beam lithography

In contrast to optical lithography, where photons account for exposure of the resist, electrons are used for e-beam lithography. Our resist system contains long polymer chains, which are destroyed due to electron bombardment at a certain critical dose. For this purpose, we utilize the electron beam lithography system at WMI, the NanoBeam nB5 from NanoBeam Limited, which is shown in Fig. 3.4. The huge advantage of e-beam lithography is, that we no longer rely on optical resolution ($\approx$ 1 - 2 µm). In this section, we discuss the previous junction layout and explain some basic concepts of e-beam lithography. Later, we describe, how the exposed area is removed during development.

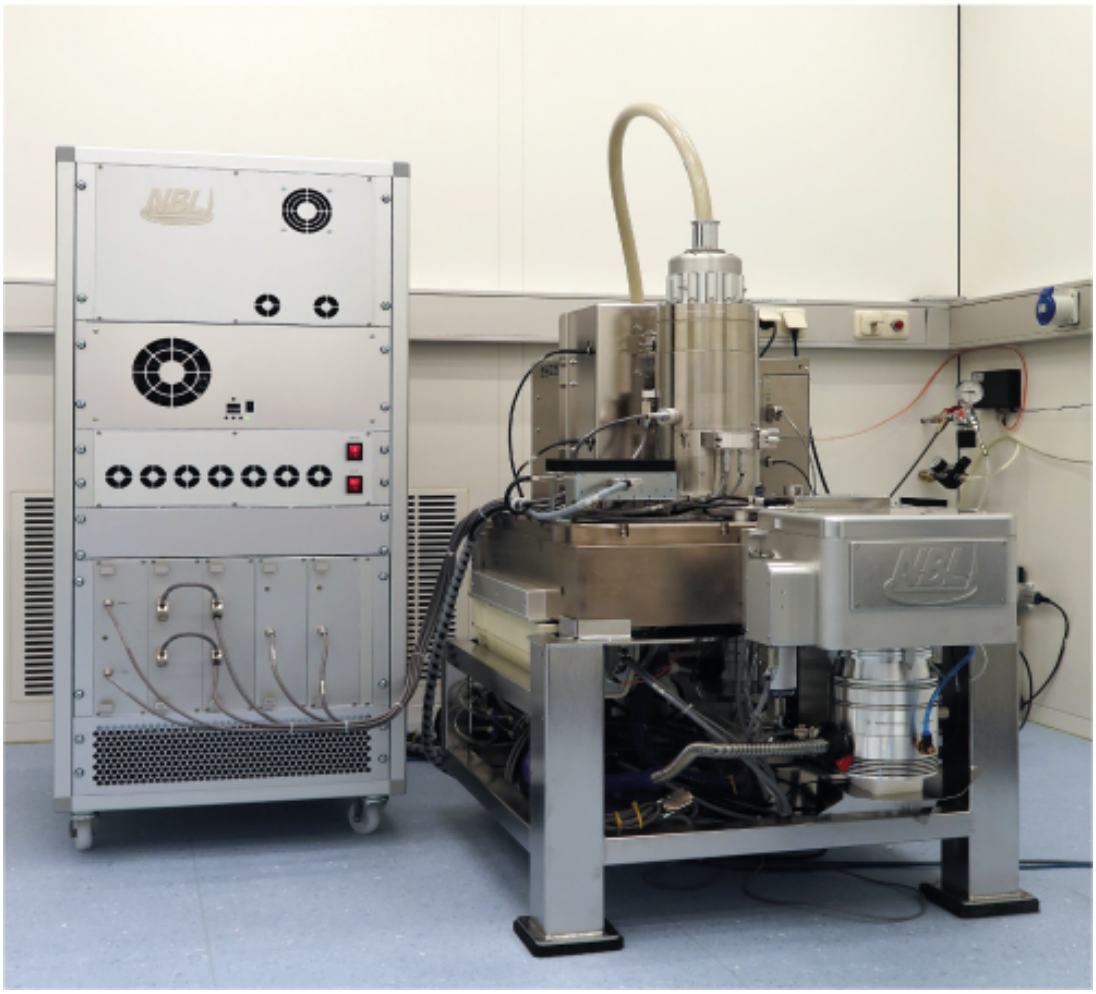

Figure 3.4: Photograph of the electron beam system nB5 from NonoBeam Limited.

Sample layout

The desired structures are drawn in LayoutEditor and afterwards compiled into a NanoBeam pattern file (npf). So far, the pattern of choice for junction fabrication at WMI has been the so-called nose-junction (Fig. 3.5). Here, the fabricated junctions don't have a perfect rectangular shape, which makes it difficult to measure the exact area. Another problem arises due to the design's susceptibility to resist thickness fluctuations. We discuss this behavior in more detail in Sec. 4.1.1 - Spin coating.

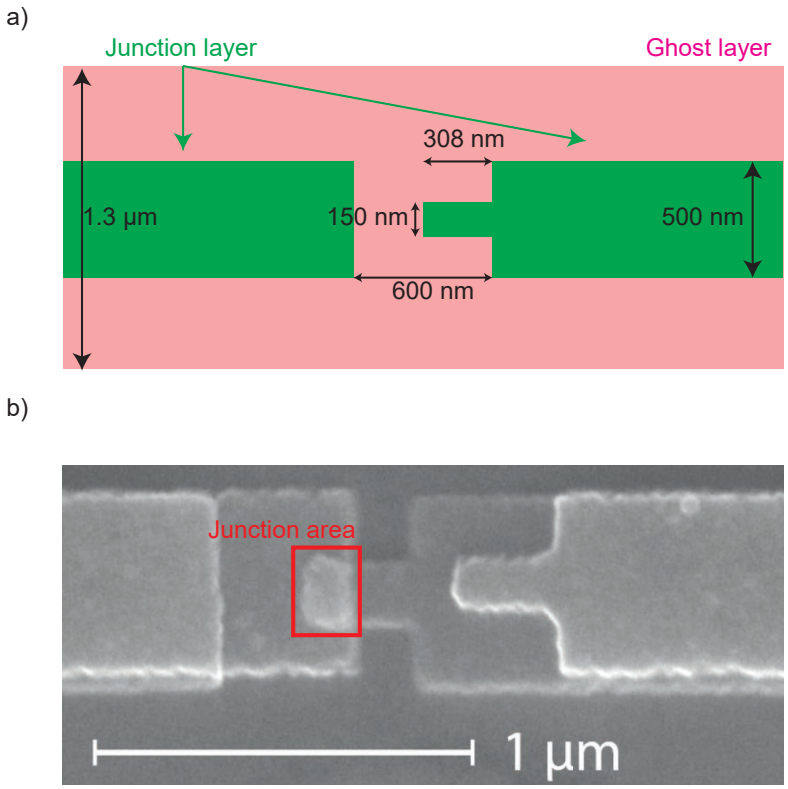

Figure 3.5: Old "nose-junction" design. **(a)** Pattern of the old junction design. It consists of a junction layer (green) and the ghost layer (pink). **(b)** Scanning electron microscope (SEM) image of a nose-junction. The junction area lies within the red square. The shape does not match the rectangular design perfectly.

Nanostructuring

The NanoBeam consists of two chambers: The load lock, which contains a cassette, that holds multiple discs. On each disc, we can mount up to 12 samples, allowing a high fabrication throughput. With the help of a robotic arm, a disc can be transferred to the main chamber, where the actual exposure takes place. In order to prevent electrons

from scattering with air molecules, both chambers are under vacuum.
After the disc has been transferred into the main chamber, we align the substrate with the internal scanning electron microscope (SEM). Next, we run an initialization setup, which performs a calibration of the electron optics and sets the acceleration voltage of the electrons to 80 kV.
The electron beam is usually out of focus due to two reasons [40]: The focal point can be out of the focus plane or astigmatism might arise. The former results in an isotropic blurring, the latter in an elliptical shape of the beam. An unfocused writing spot will cause discrepancies between the designed pattern and the real structure. Consequently, as final calibration step, we focus the electron beam by looking at the gold nanoparticles through the SEM. We adjust the focus point until the particle shapes are well visible. Note, that the resists are also susceptible to the electrons from the electron microscope. For this reason, we place the nanoparticles at the substrate edges, where no relevant structures will be written.
Finally, we create a job file, where we assign a value of charge dose (in units of C/m^2) to each layer in the pattern file. Depending on structure size, the choice of resist, and its thickness, different doses are required. Too high values increase the amount of back-scattered electrons, resulting in an increased exposed area. On the other hand, too low values might not deliver sufficient energy to cut all polymer connections through the whole resist, leaving areas partially underexposed.

Development

As next step, we remove the exposed resist by placing the sample in a developer (Ar-600-56) for 1 minute at room temperature. Afterwards, we switch to a cold IPA bath (T = 4.5 °C) for 10 minutes. This second bath acts on the bottom resist, while the top layer is largely unaffected. The result is an undercut in the profile (Fig. 3.6), which is needed for shadow evaporation and proper lift-off. As last step, we put the sample into deionized water in order to stop the development process and remove residual IPA. Using cold IPA during the second development, we achieve a slower development process. This allows us to use longer development times, creating a more stable process.

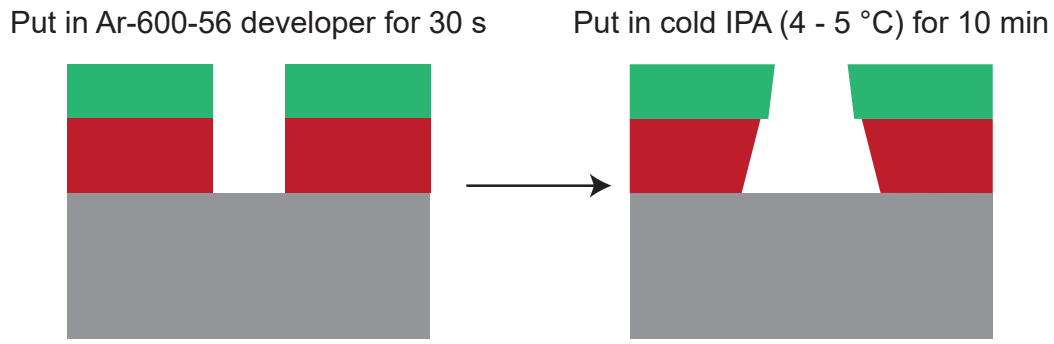

Figure 3.6: Schematic of the development process. The first developer removes the exposed resist from both layers. During the second development step with IPA we achieve an undercut, as it mainly acts on the bottom resist.

3.1.3 Evaporation and oxidation

In order to deposit nm-thin films of metals, evaporation is a well-established technique. In an ultra-high vacuum (UHV), the metal is heated by an electron beam with high currents until it melts. Thus, parts of the metal evaporate and deposit uniformly on the sample as a thin layer. In the following section, we present the well-known technique of shadow evaporation, used to form Josephson junctions, followed by a lift-off process to remove residual resist and metal. Afterwards, we introduce the evaporation system at the WMI, which fulfills all requirements for shadow evaporation.

Shadow evaporation

During shadow evaporation (Fig. 3.7), a silicon substrate with a double layer resist is mounted in a UHV chamber. While the developed top layer serves as a mask, the bottom resist provides an undercut. At the desired junction location, we find a suspended resist bridge (Dolan bridge), which creates a shadow on the substrate. Now, aluminum is evaporated under an angle of 17° and with a thickness of 40 nm. Afterwards, we oxidize this first layer under a constant pressure, by letting a constant oxygen flow into the chamber for 70 minutes. Typically, we achieve a pressure of 7.9×10^{-3} mbar under an oxygen flow of 8 sccm. As last step, we evaporate a second aluminum layer under an angle of -17° and a thickness of 70 nm, in order to create an overlap between the oxidized bottom layer and the new top layer. Finally, we obtain an $Al/AlO_x/Al$ sandwich, which serves as Josephson junction.

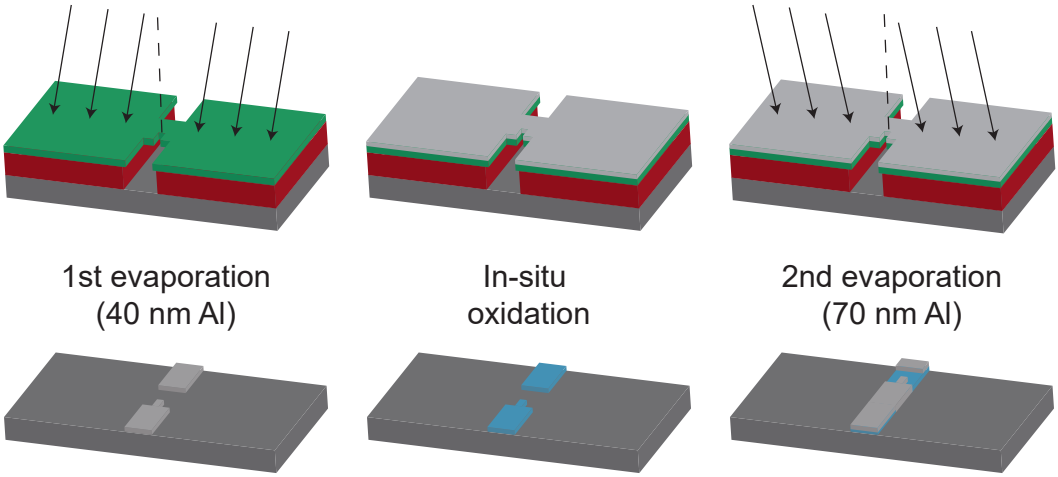

Figure 3.7: Illustration of the shadow evaporation process. The bottom and top resists are shown in red and green, respectively. The top row shows the process with resist bridge while in the bottom row the resist is not shown for a better visibility of the evaporated structures.
First, we evaporate 40 nm of aluminum under an angle of 17°. This step is followed by an in-situ oxidation under constant pressure for 70 minutes. Then we evaporate another layer of aluminum (70 nm) at an angle of -17°.

Evaporation system

The evaporation system at the WMI is home-made and basically consists of two chambers: a load lock and the process chamber (Fig. 3.8). The load lock allows a quick exchange of samples, while we can keep constant UHV in the main chamber, avoiding contamination. The main chamber is constantly pumped with a turbo molecular pump. Different pressure sensors are mounted inside each chamber. A crucible changer allows for fast exchange of evaporation material. It contains aluminum, titanium and gold. On the backside, the ion gun and quartz crystal are connected to the main chamber.
The quartz crystal oscillates with a certain frequency which depends on its mass. During evaporation, more and more material is evaporated onto the crystal, changing its mass and frequency. From the frequency change, the evaporation rate can be deduced. Once calibrated, this is a very precise way to determine the evaporated thickness. The system control panels, including a computer, allow for an automated evaporation and display the system parameters during evaporation. Additionally, the ion gun can be controlled here.

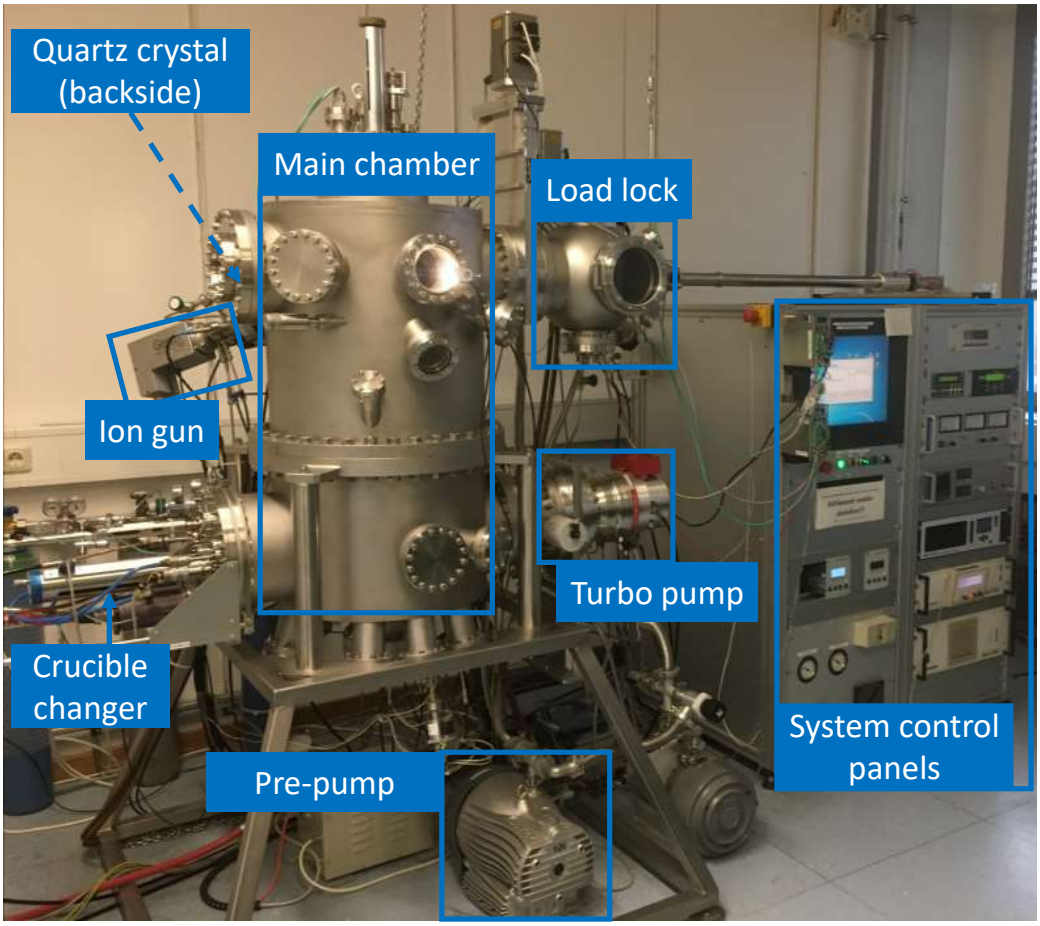

Figure 3.8: Evaporation system. It consists of a main chamber (or evaporation chamber) and a load lock for fast sample exchange. Turbo and pre-pump maintain UHV in the main chamber. Different pressure sensors are mounted inside each chamber. A crucible changer allows for an exchange of evaporation material. On the backside, one finds the ion gun and a quartz crystal, connected to the evaporation chamber.

Lift-off process

After shadow evaporation, we need to get rid off remaining resists and metal. From there, we put the the sample into acetone and heat it at 80 °C for 10 min. Afterwards, we put the sample into a supersonic bath at level 1 for 2 seconds. Next, we put the sample in IPA at room temperature and carefully stirr with a plastic pipette for 2 minutes. Finally, the sample is blown dry with nitrogen. As shown in Fig. 3.9, this procedure does not always lead to reproducible results. Often aluminum at the CPW gaps is not removed. Especially small gaps (from the resonators) are usually covered with aluminum. Improvements are discussed later in Sec. 4.1.

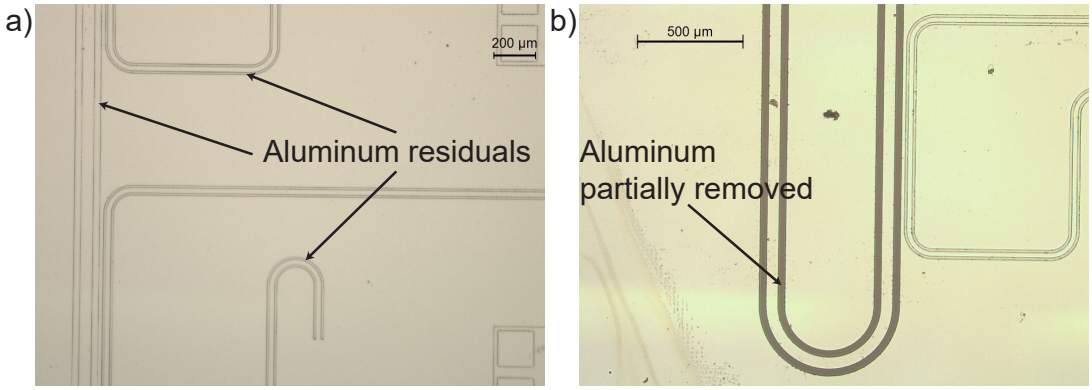

Figure 3.9: Optical microscope image of two of our first samples, fabricated using the standard process.
(a) Using the standard lift-off method, but without the plastic pipette, the aluminum film at the gap positions is not removed. **(b)** Carefully stirring the IPA with a plastic pipette removes the aluminum for wider gaps. However, tinier areas are still not removed at all. This result is not well reproducible due to inconsistent usage of the pipette.

3.2 Room temperature resistance measurement setup

In order to obtain the critical current density of our junctions, we measure their room temperature resistance. Since we have 144 SQUIDs on each sample, we require a fast but accurate measurement setup (Fig. 3.10). For that reason, we connect the cables of a current source to two conducting needles of a wafer prober with very small tips. With the help of a microscope, we align each of the two conducting pads of a SQUID with one of the needles. We apply voltages V of -1 to 1 mV, while we measure the corresponding current I through the loop. In order to obtain a proper measurement, we start a voltage sweep, while we lower the needles. As soon as we see ohmic behavior, we turn off the current source and restart for a full sweep. The reason for this procedure is the small thickness of the aluminum layers. If one applies too much pressure, the needle will punch a hole into the aluminum and eventually falsify the measurement.

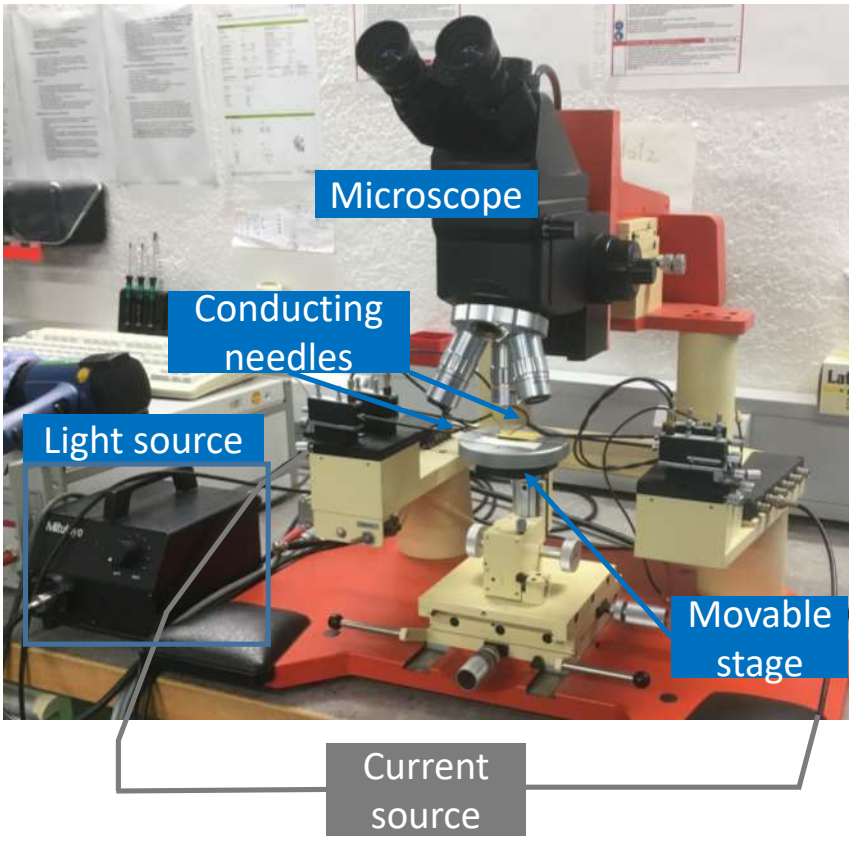

Figure 3.10: Setup for room temperature resistance measurements.

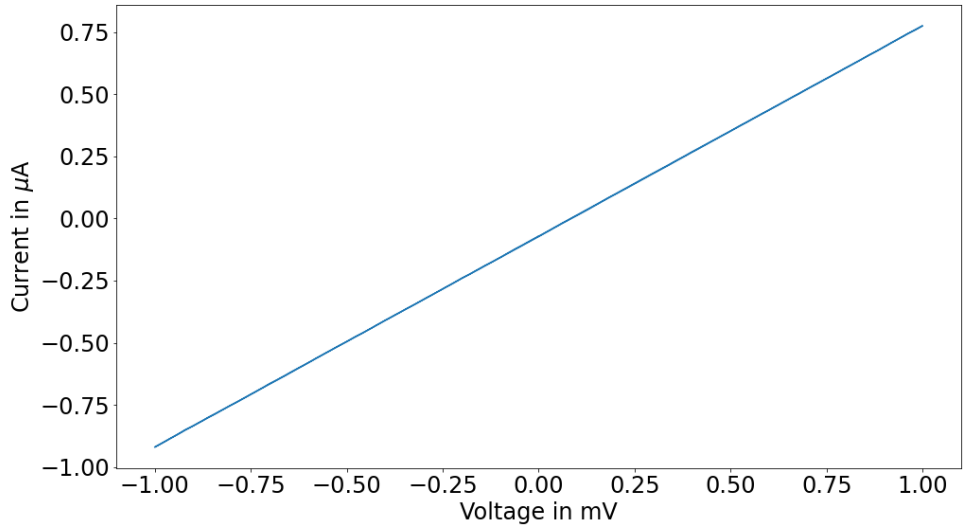

Figure 3.11: Exemplary current-voltage characteristics of an aluminum SQUID measured at room temperature.

Finally, a Python script performs a linear fit to each measurement. A typical graph is shown in Fig. 3.11. According to Ohm's law,

$$I = \frac{1}{R_\mathrm{n}} V, \tag{3.1}$$

and the linear equation

$$y = m \cdot x \tag{3.2}$$

we can extract the room temperature resistance from the inverse slope $R_\mathrm{n} = 1/m$.
A more detailed analysis follows in Sec. 4.2.

3.3 Resonator measurement setup

3.3.1 Sample packaging

For a transmission measurement, we need to connect our sample to the microwave cables from a VNA. We do this by gluing the substrate with GE varnish (specifications shown in Fig. C.2) onto a copper box, which is coated with gold (Fig. 3.12). The inner conductor of the feedline is then bonded with aluminum to the inner conductor of a printed circuit board (PCB). On the other hand, the PCB's inner conductor is soldered to the inner conductor of a microwave cable connector. The ground planes of the sample are connected to the ground planes of the PCBs. A photograph of a bonded sample is shown in Fig. 3.13. Typically, we use as many bonds as possible in order to avoid charge accumulations on the sample.

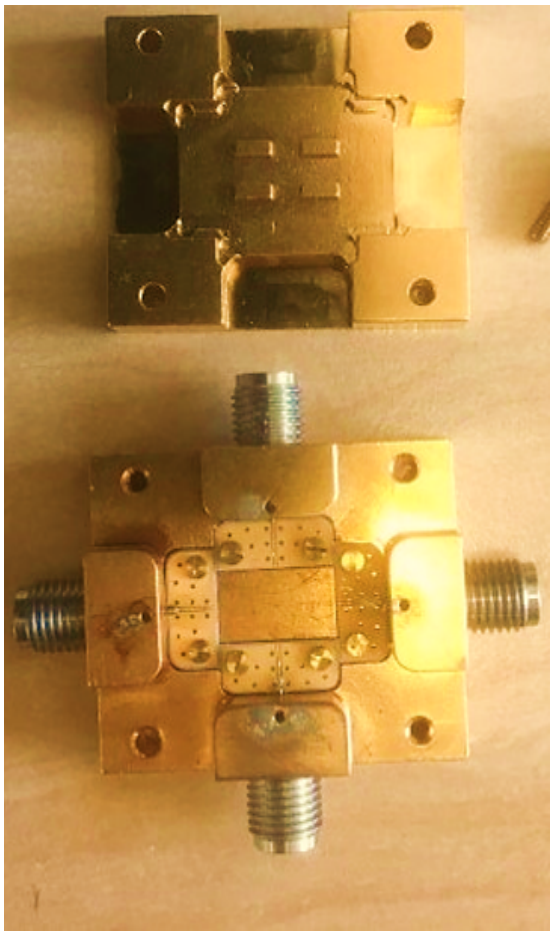

Figure 3.12: Optical micrograph of our 4-port sample holder. For our transmission measurements, we connect the sample to ports west and east.

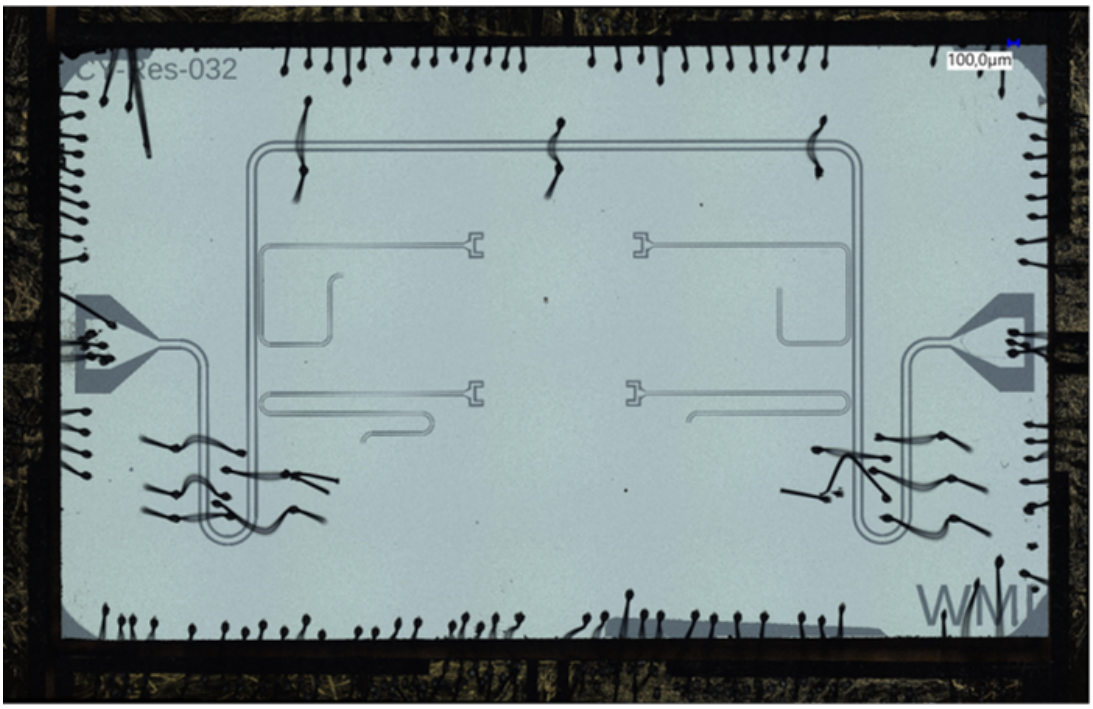

Figure 3.13: Optical micrograph of one of our samples, connected to the 4-port sample holder.

After bonding, we perform a time domain reflectometry (TDR) measurement to check for impedance mismatches. The TDR sends an microwave pulse via a cable through the sample holder PCB and the on-chip transmission line. If at any point on the line an impedance mismatch is present, the wave is partially reflected. This reflected signal is then detected by the TDR and converted into an impedance mismatch. We can even identify the position of the mismatch, by plotting impedance versus travel time of the wave (Fig. 3.14). First, we measure only the cable (blue line). At the end of the cable, there is an open circuit leading to a huge impedance mismatch. Next, we measure both ports to check for a proper soldering between connector and PCB (purple and red curve). Here, we can observe a minimal deviation, which is typical. Last, we perform a measurement on each port with a bonded sample (green and orange lines). As soon as the microwave travels through the PCB and the bonds, we measure an increasing impedance. Impedance mismatches are common at the bond positions.

3.3.2 Cryogenic setup

Our resonator measurement is carried out in a 3He/4He dilution refrigerator with a base temperature of approximately 50 mK. A more detailed description of the working principle of such refrigerators can be found in Refs. [41] and [42]. The cryogenic measurement setup is shown in Fig. 3.15.

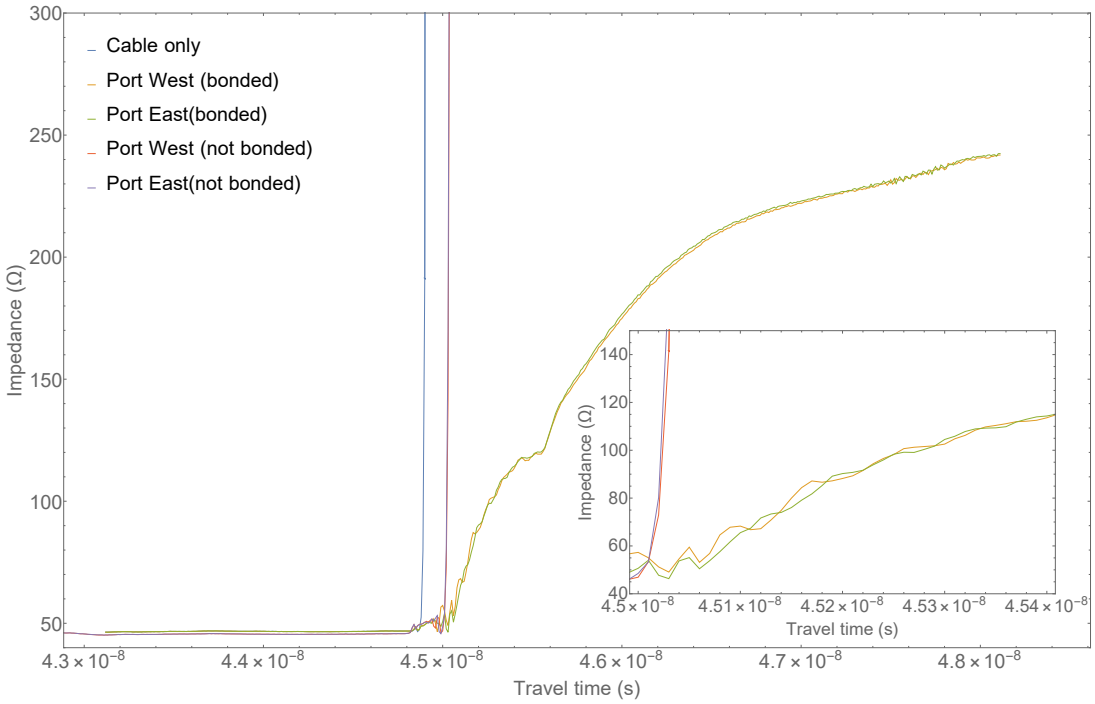

Figure 3.14: TDR measurement of sample Res-005 mounted inside the 4-port sample holder. The inset shows the impedance change due to the bonds.

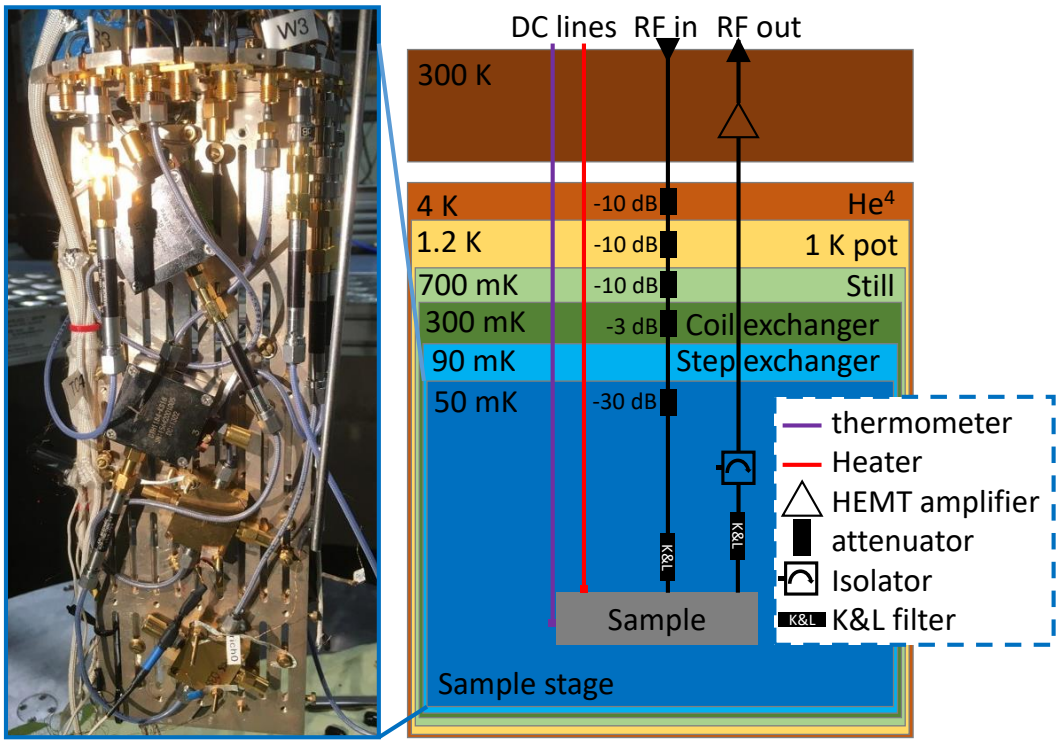

Figure 3.15: Image of the sample stage (left) and schematic drawing of our dilution refrigerator with all important components for the resonator quality factor measurements (right).

Chapter 4

Experimental results

Now that we are familiar with the fabrication process and the experimental setups, we present our experimental results.
First, we go through the fabrication process step by step and show the improvements we achieve during the course of this thesis.
Second, we present the room temperature resistance measurements from SQUID loops and discuss the influence of different fabrication parameters.
Finally, we extract the internal losses from transmission measurements of our resonators and give a guideline, how to distinguish the different loss sources from Sec. 2.5 and how to reduce them.

4.1 Improvements on the fabrication process

4.1.1 Sample preparation

Removal of protective resist - additional ashing

As we can see in Fig. 4.1, most of the resist is removed during the standard cleaning process. However, having a closer look, one clearly observes some resist leftovers (inset of Fig. 4.1). These leftovers can contain TLSs and increase the loss of resonators on one hand. On the other hand, they can cause structural damage during fabrication.

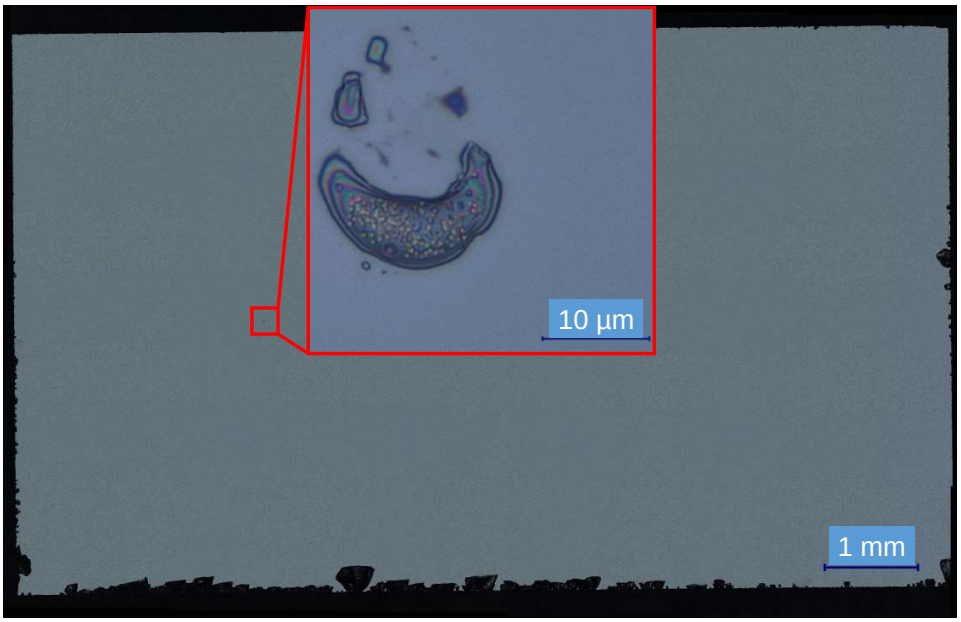

Figure 4.1: Substrate from Fig. 3.1 after the standard cleaning process. Most of the protective resist is removed by our standard cleaning process. However, often some small areas are still covered with resist leftovers.

In order to get rid of those resist leftovers, we perform a so-called plasma ashing step. For that, we create an oxygen plasma in our reactive ion etching (R.I.E.) system (Fig. Plasmalab) using high power radio waves. Those oxygen radicals combine with the resist and form ash, which is removed by a vacuum pump. In the course of this thesis, we investigate two different ashing times, as well as a third ashing process where we add argon (argon:oxygen ratio of 1:2). The idea is to use argon as "physical" component to remove native oxide on top of the silicon substrate.

Sometimes, independently of the specific ashing method, there is still resist left on the chip surface. Therefore, we add an additional cleaning step as shown in Fig. 4.2) by flushing the sample with acetone and putting it into a supersonic bath in IPA. Finally the sample is blown dry with nitrogen and we end up with a clean sample.

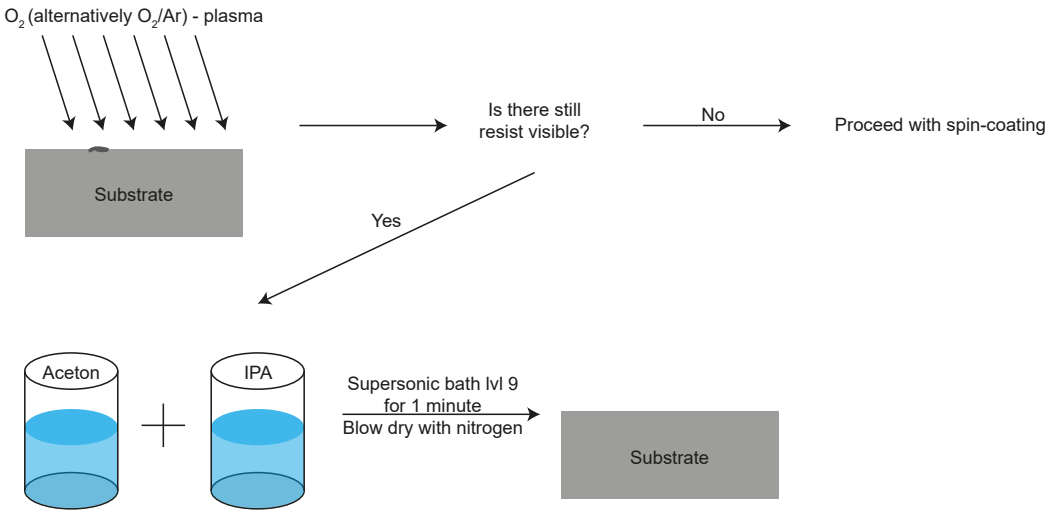

Figure 4.2: Scheme of our ashing process with optional additional cleaning. During this thesis we vary the ashing time (for oxygen ashing) and also perform ashing with an argon/oxygen-mixture. Sometimes, even after the ashing process resist is still there. For that reason, we add a second cleaning with acetone and IPA in a supersonic bath. The ashing softens the resist, which allows us to remove it with this additional cleaning and we end up with a clean sample.

AFM measurements

We want to investigate the effect of our ashing processes, as resonator losses are dependent on surface properties of the substrate [29]. We have a closer look at our samples using an atomic force microscope (AFM).
In general, as discussed in Ref. [29], the total internal loss increases with surface roughness, while the TLS losses stay unaffected (Tab. 4.1).

RMS roughness in gap (nm)	δ_i (10^{-5})	δ^0_{TLS} (10^{-5})
45 ± 0.3	8.5	1.5 ± 0.1
11 ± 0.3	1.6	1.3 ± 0.3

Table 4.1: Comparison of internal losses in dependence of surface roughness at the gaps. Data taken from Ref. [29].

For our analysis, we measure 5 positions on a cleaned substrate for the following procedures:

- standard cleaning
- oxygen ashing (3 minutes)
- oxygen/argon ashing (3 minutes)

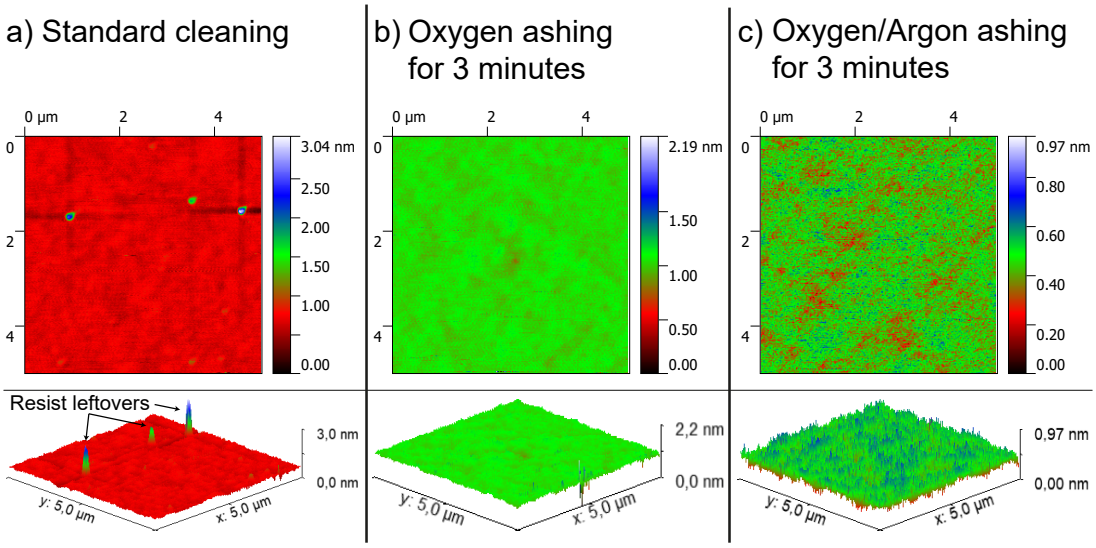

Figure 4.3: AFM measurements of silicon substrates after different ashing processes. The top row shows an aerial perspective, while the bottom row the corresponding 3D view. **(a)** Colorplot for standard cleaning process. One can see 3 areas with resist leftovers.**(b)** Colorplot for oxygen ashing process. Here, no resist leftovers can be seen. **(c)** Colorplot for oxygen/argon ashing process. Here, no resist leftovers can be seen.

Figure 4.3 shows typical AFM images of all three cases. Here, each measurement covers a $5 \times 5\ \mu m^2$ area. The root mean square (RMS) roughness extracted from the colorplots is summarized in Tab. 4.2. All measurements can be found in Tab. C.1.

Cleaning method	Standard cleaning	Oxygen ashing	Oxygen/Argon ashing
Avg. RMS roughness (nm, total grid size)	0.063	0.052	0.083
Avg. RMS roughness (nm, without grains)	0.052	0.052	0.066

Table 4.2: Root mean square (RMS) roughness according to our AFM measurements. The values in line 2 are calculated by averaging the measurements of 5 positions on the sample. Each has an area of $5 \times 5\ \mu m^2$.
In line 3, we average over 4 areas of $1 \times 4\ \mu m^2$ size per position. The areas are chosen such that they do not contain any grains. Therefore, we can neglect high resist leftovers or other dirt and get more insight about the actual substrate surface.

From our data we can extract two important results:
First, our average roughness is smaller compared to the values from Ref. [29]. This arises from a different fabrication process. Wisbey et al. produce their samples by etching into a metal-covered substrate with a structured resist on top. This step might also attack the substrate, resulting in a higher surface roughness. In our case, none of the fabrication steps after the ashing affects the substrate surface remarkably.
Second, oxygen ashing does not change the roughness. We even see a lower value over the whole area, but this occurs from less resist leftovers. We split each area into 4 smaller areas of $1 \times 4\ \mu m^2$, chosen such that they do not contain grains. Averaging then gives the same result as for standard cleaning. Adding argon during the ashing process slightly increases the roughness.
To sum up, both of our ashing processes reduce the amount of residual resist without damaging the substrate and therefore they should not increase internal losses.

Spin coating

During the course of this thesis, we analyze our spin coating process, performing film thickness measurements with a white light spectrometer. At this point we would like to thank Rayner Schelwald from Filmetrics for inviting us to his company in order to test their measurement setup (Fig. 4.4). It contains a spectrometer, which is attached to an automated stage, allowing fast measurements across whole wafers (up to 100 mm diameter). An additional deuterium/halogen light source increases the range of accessible substrate-film combinations one can measure.

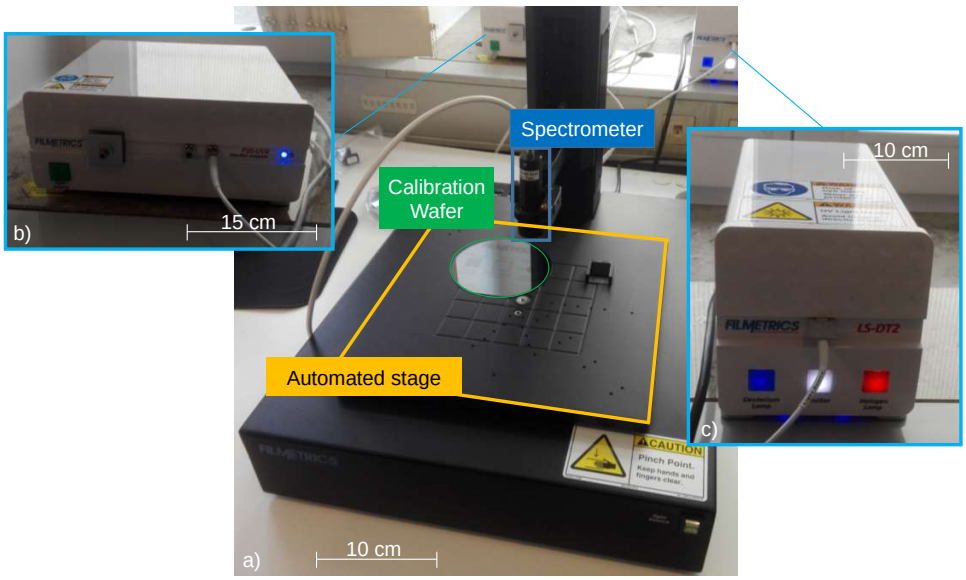

Figure 4.4: Filmetric's setup for resist thickness measurements. **(a)** Automated stage, with spectrometer and calibration wafer. **(b)** Thin film analyzer with integrated light source. **(c)** Additional deuterium/halogen light source.

During operation, the spectrometer varies the wavelength (200 nm - 1050 nm) of incident light, then the thin film analyzer measures the intensity of reflected light. There are two reflected waves, one from the substrate and the other one from the resist. Both waves can interfere with each other, depending on their phase relation. Under an incident angle of $\alpha = 90°$, constructive interference occurs for

$$2nd = k\lambda, \tag{4.1}$$

while destructive interference appears for

$$2nd = \left(k + \frac{1}{2}\right)\lambda. \tag{4.2}$$

Here, d is the resist thickness, n the defractive index, k an integer, and λ the wavelength. Varying the wavelength, one sees an oscillatory behaviour in reflection with d determining the period of oscillation. Figure 4.5 shows a typical reflectance measurement with varying wavelength (blue line) and the corresponding curve, calculated from the model (red line). Although they differ in amplitude, the positions of maxima and minima fit very well, allowing a proper thickness extraction.

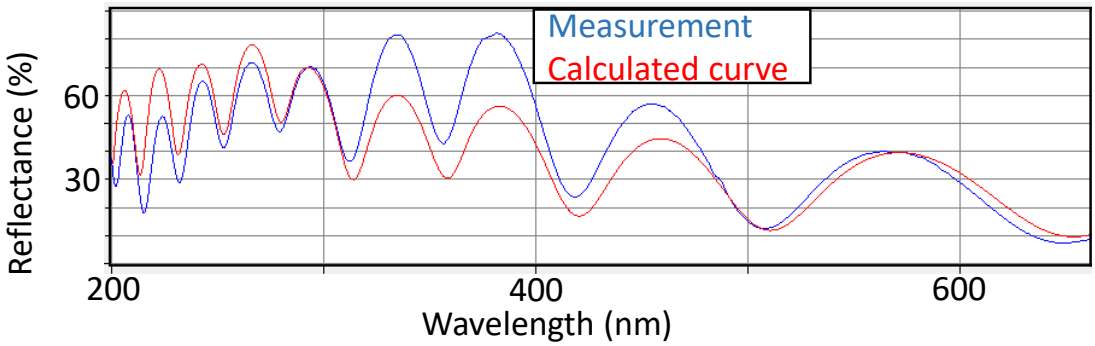

Figure 4.5: Reflectance measurement for a spin coated sample at an arbitrary position. The blue curve shows the measured reflectance, while the red curve shows the calculated curve obtained from the model. One may note the difference in amplitude between measurement and simulation. However, for our purpose, only the periodicity matters, which shows good agreement between measurement and simulation.

Performing such a measurement on different positions on the sample, we plot a colormap across the substrate. As the refractive index of our two resists is very similar, it is not possible to distinguish both of them within one measurement. Consequently, we measure two samples with only PMMA/MA 33% and two samples with both resists. For each variant a colorplot is shown in Fig. 4.6 and Fig. 4.7, respectively. The results of all measurements are summarized in Tab. 4.3.

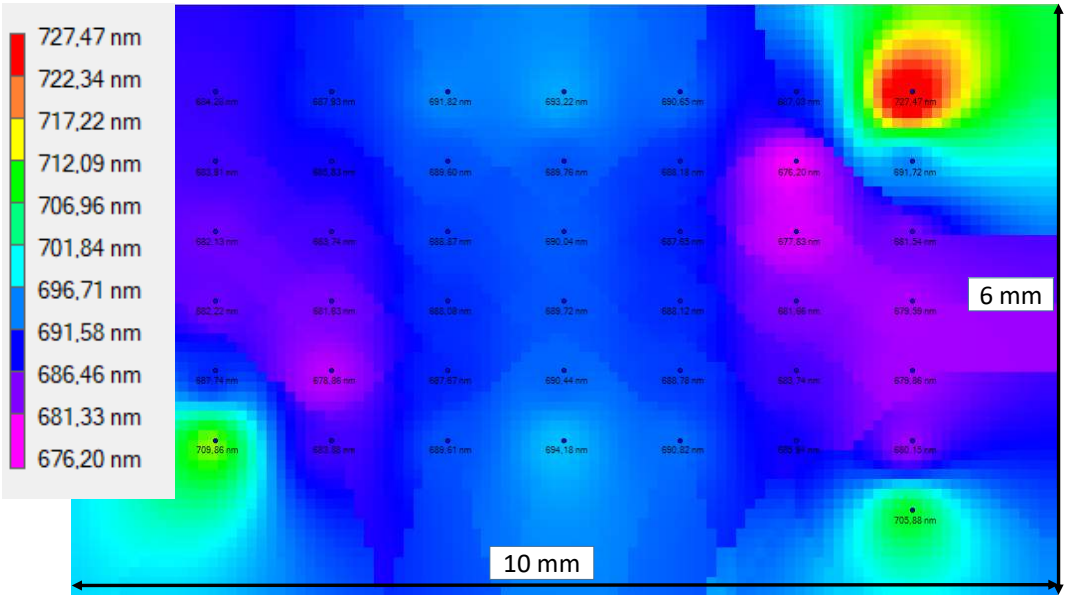

Figure 4.6: Resist thickness variation over a $6 \times 10\,\mathrm{mm}^2$ silicon substrate. This sample is coated with a single resist layer of PMMA/MA 33% at 2000 R.P.M. The thickness values are obtained via white light spectrometry.

For the single resist, we obtain an average thickness of 688.09 nm for sample F001 and 652.65 nm for sample F002, respectively. We already see a difference of approximately 5% between both samples. On the other hand, for the double resist layer we only have a difference of less than 2%. Within each sample we observe an average spread of 46 nm between minimal and maximal thickness. While the bottom resist generally shows a higher spread (53.7 nm), the double layer seems to be more continuous with 38.6 nm spread of total thickness.

Sample	Resist	Minimal thickness	Maximal thickness	Avg. thickness	Std. dev.
F001	Single layer	676.20	727.47	688.09	8.86
F002	Single layer	627.57	683.69	652.65	14.38
F003	Double layer	752.31	788.33	761.74	10.47
F004	Double layer	735.01	776.24	750.47	8.61

Table 4.3: Comparison of film thickness measurements of different samples and resist systems. All quantities are given in nm.

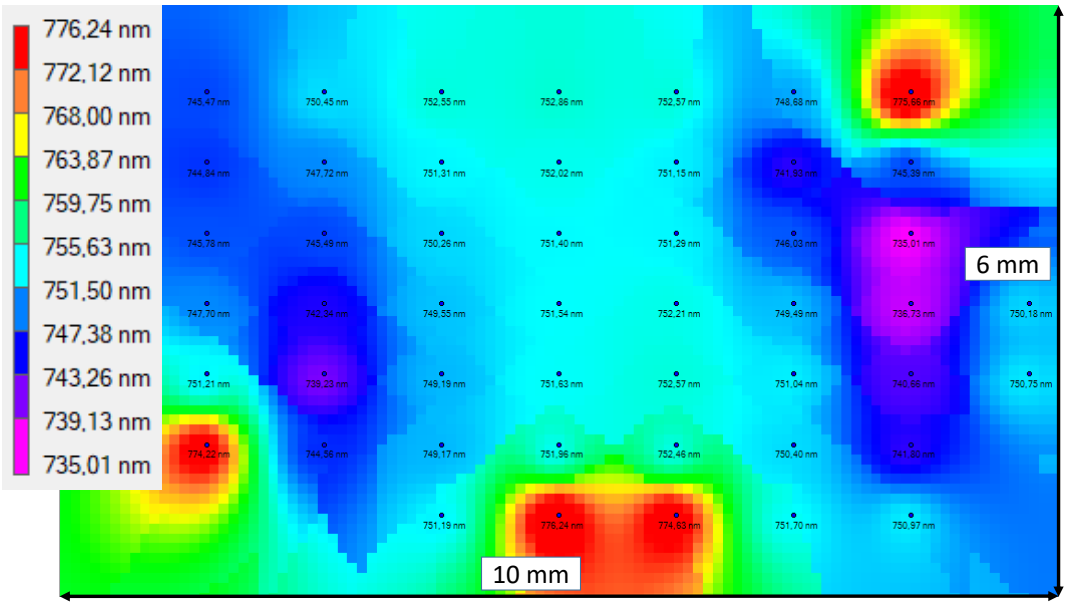

Figure 4.7: Resist thickness variation over a $6 \times 10\,\mathrm{mm}^2$ silicon substrate. This sample is coated with a double resist layer, consisting of PMMA/MA 33% (bottom resist) and PMMA 950 K (top resist). The thickness values are obtained via white light spectrometry.

During shadow evaporation, the resist thickness is a crucial parameter. Figure 4.8 illustrates how an overlap junction is formed during shadow evaporation. The overlap length depends on bridge width b, incident angles α_1 and α_2, as well as the bottom resist height h_1. Note that the top resist thickness should not affect the junction geometry. From a simple geometric picture, the shift due to an incident angle during evaporation is given by:

$$\Delta x = h_1 \tan(\alpha) \tag{4.3}$$

Taking Eq. 4.3, we can calculate the total overlap x_{overlap} by:

$$x_{\mathrm{overlap}} = \Delta x_1 + \Delta x_2 - b = h_1 \cdot (\tan(\alpha_1) + \tan(\alpha_2)) - b \tag{4.4}$$

where Δx_1 and Δx_2 denote the shift due to evaporation 1 and 2, respectively. The junction area then is given by $A_{\mathrm{junction}} = b_{\mathrm{nose}} \cdot x_{\mathrm{overlap}}$, with b_{nose} being the width of the nose from the design. Taking a bridge width of $b = 292\,\mathrm{nm}$, incident angles of $\pm 17°$ and a nose width $b_{\mathrm{nose}} = 150\,\mathrm{nm}$, we can investigate the influence of the resist thickness on the junction area (Tab. 4.4).

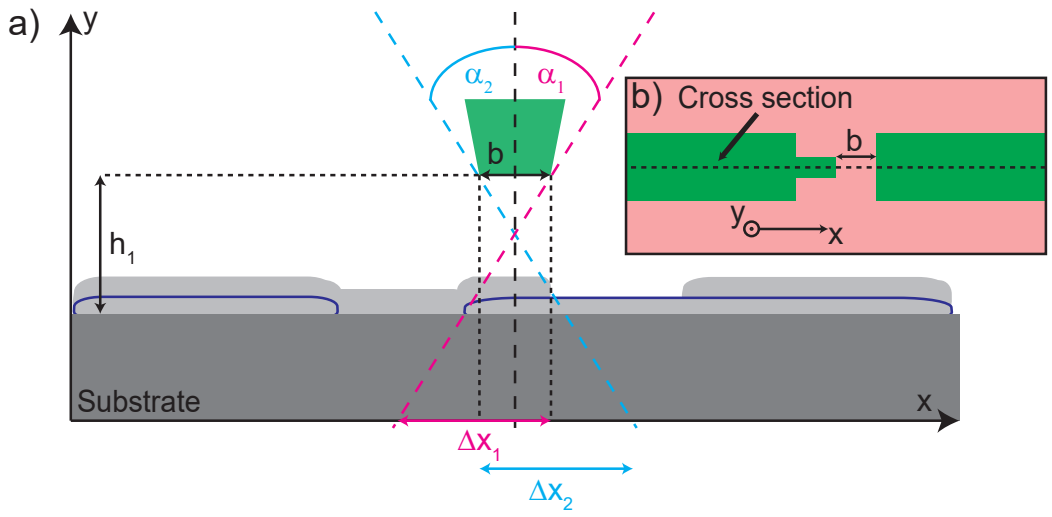

Figure 4.8: Schematic of shadow evaporation using a Dolan bridge. **(a)** Cross section of a nose-type junction. The overlap length depends on bridge width b, incident angles α_1 and α_2, as well as the bottom resist height h_1. **(b)** Junction design. The cross section shown in (a) is along the dashed line.

Taking the average values for samples F001 and F002, as well as the minimal and maximal measured thickness, we obtain an average area of $A_{\text{junction}} = 0.018\ \mu\text{m}^2$. Although the thickness variations are not too high, the related junction areas show a spread of ±25%. We want to mention, that the actual bridge width is smaller due to scattered electrons and the development process. The nose width might also differ, depending on charge dose and development parameters. However, we can take these results as an estimation for the vulnerability of the nose junction design.

Resist thickness	627.57	652.65	688.09	727.47
x_{overlap}	91.73	107.07	128.69	152.82
Junction area (μm^2)	0.0138	0.0161	0.0193	0.0229

Table 4.4: Comparison of junction area in dependence of film thickness. The variation in resist thickness cause a huge deviation in the junction areas.

Since substrates have finite dimensions, we will always see edge beads and fluctuations in the resist height, making it difficult to improve the spin-coating process. Consequently, we chose to change our junction design, which will be introduced in the next section.

4.1.2 Electron beam lithography

As already mentioned, we implement a new design for our Josephson junctions, so-called cross-type junctions. This new design is mostly independent of resist thickness variations and a promising approach to scale superconducting circuits.
Later, we also present our resonator design. Here, a coplanar waveguide serves as feedline for transmission measurements. For each chip, we couple four λ/4-resonators to the feedline. We space their resonance frequency by roughly 300 MHz, so we can easily distinguish them during our measurements.
We further compare different development parameters and try to find a good trade-off between resolution and reproducibility.
As last part, we present our new evap sample holder, which is capable of carrying up to 4 inch wafers and allows for processes requiring substrate rotation.

Sample layout

During shadow evaporation, the position of the bridge shadow depends on angle and resist thickness. As we could see earlier, relatively small thickness variations can lead to a large spread in junction area. Further, the total yield is typically low, as some structures might not show a proper overlap. For future applications, we have to improve on these issues.
As consequence, we decide to change our design into a cross-type junction, originally invented by Martinis *et al*. It consists of two conductors, arranged orthogonal to each other (Fig. 4.9). For our first tests, we add many vertical conductors with a width $w_v = 200\,\text{nm}$ in order to obtain more statistics. Additionally, we apply a small charge dose around the bridge (ghost layer) in order to improve an undercut in the resist walls.

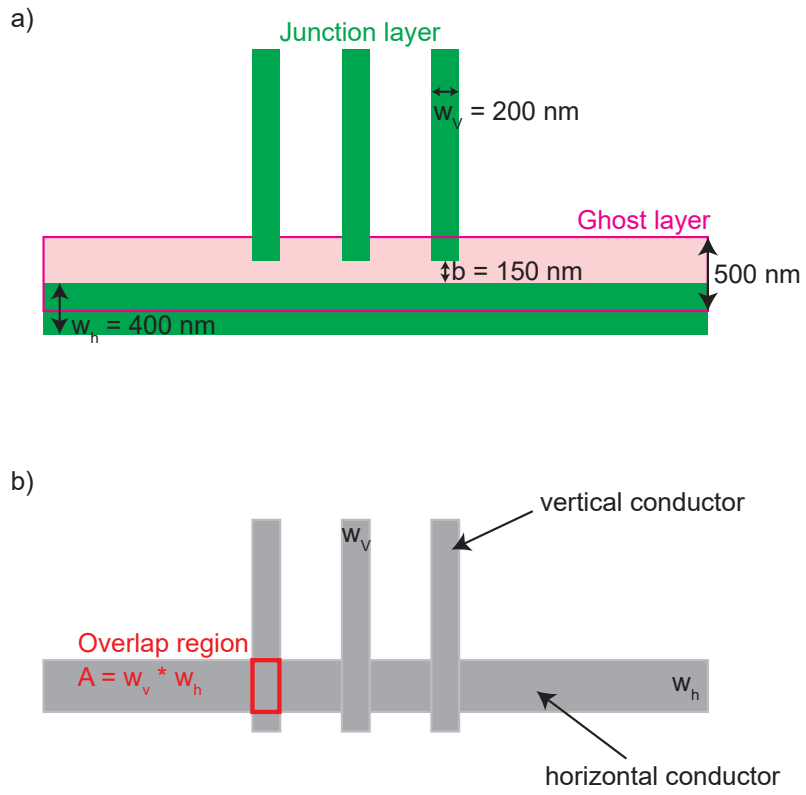

Figure 4.9: Test design for multiple cross-type junctions using one horizontal and many vertical conductors. **(a)** E-beam pattern of the cross type junction. Typical charge doses are 7 C/m^2 for the junction layer (green) and 0.8 C/m^2 for the ghost layer (pink). **(b)** Schematic view of a cross-type junction. The junction area is equal to the overlap region $A = w_\mathrm{v} w_\mathrm{h}$.

The major advantage of this geometry is the independence of incident angle during evaporation. For the first evaporation, we can chose a steep angle ($\alpha_1 = 50°$), while we evaporate the second layer without tilting the sample ($\alpha_2 = 0°$). The junction is formed by an overlap of horizontal and vertical conductor with an area $A = w_\mathrm{h} \cdot w_\mathrm{v}$, simply given by the conductor widths. Since we choose a steep angle, both conductors will overlap entirely, independent of resist thickness.
Later on, we adjust the design by adding a t-shape to the vertical conductor (Fig. 4.10), inspired by Alexander Bilmes from KIT. This way, we form a symmetric, rectangular Dolan bridge ($b = 300$ nm), which facilitates a homogeneous development from both sides. We also change both conductor widths to 200 nm.

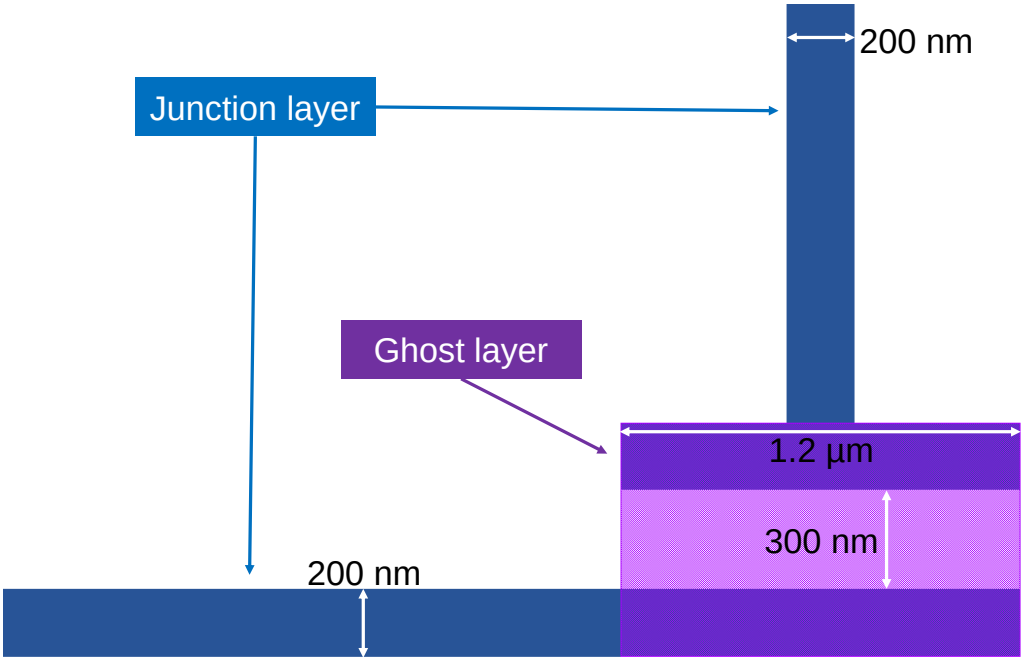

Figure 4.10: Updated crosstype design. The vertical conductor has been extended above the resist bridge in order to facilitate a homogeneous development from both sides of the bridge.

We insert the new junction design into state of the art Xmon qubits in the form of SQUID loops (Fig. 4.11). Since we want to analyze our fabrication by measuring room temperature resistance of the SQUID loops, we extend the x-shaped capacitance above the loop to a rectangle. We also add a rectangle structure below the loop. Both serve as conducting pads, we can easily contact. We design three different types of SQUID loops with identical junction parameters.
Now we build an array of $7.5 \times 3.8\,\mathrm{mm}^2$ size, containing 144 SQUIDs, in order to investigate position and charge dose dependence (Fig. 4.12). The whole area is split into 6 sections. Within each section, we vary the applied charge dose between $5.0\,\mathrm{C/m}^2$ and $8.5\,\mathrm{C/m}^2$ for each triplette of SQUIDs.

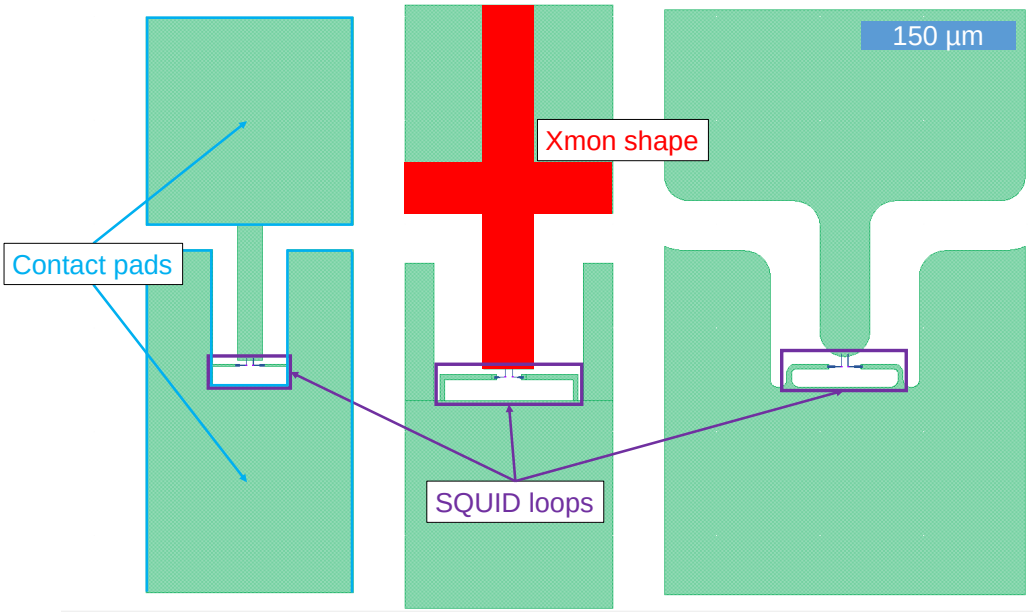

Figure 4.11: Different designs for SQUID loops, inspired by the state of the art Xmon qubit. We extend the x-shaped capacitance above the loop to a rectangle and add another rectangle below the loop. Both serve as contact pads.

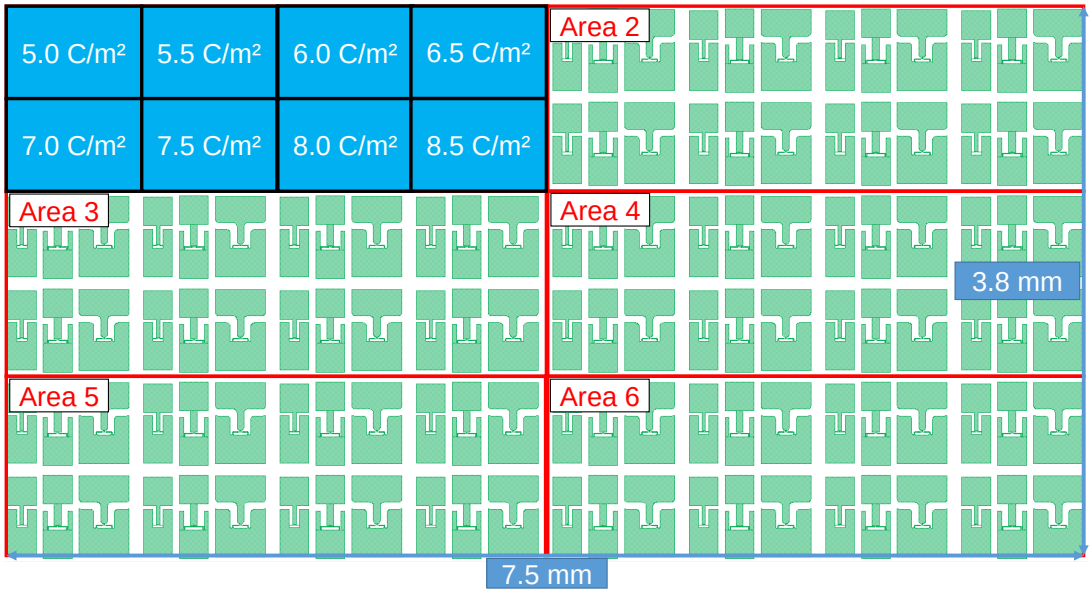

Figure 4.12: Chip layout for SQUID samples. We arrange 144 SQUIDs in an array of 7.5 × 3.8 mm^2. Then we devide the whole area into 6 sections (red rectangles). Within each section, we vary the charge dose for each triplette of SQUIDs (blue boxes).

For the linear part of our circuitry (the resonators), we use a coplanar waveguide as our feedline (Fig. 4.13). This approach allows us to perform transmission measurements, having an input on the left and an output on the right. On each chip, we couple then four $\lambda/4$-resonators to the feedline. At the open end, we add a horseshoe structure, which can be used to mediate coupling between the resonator and the capacitance of an Xmon qubit in the future. Both, resonators and feedline, have a geometry, such that their characteristic impedance $Z_0 \approx 50\,\Omega$ (see Tab. 4.5 for more details).

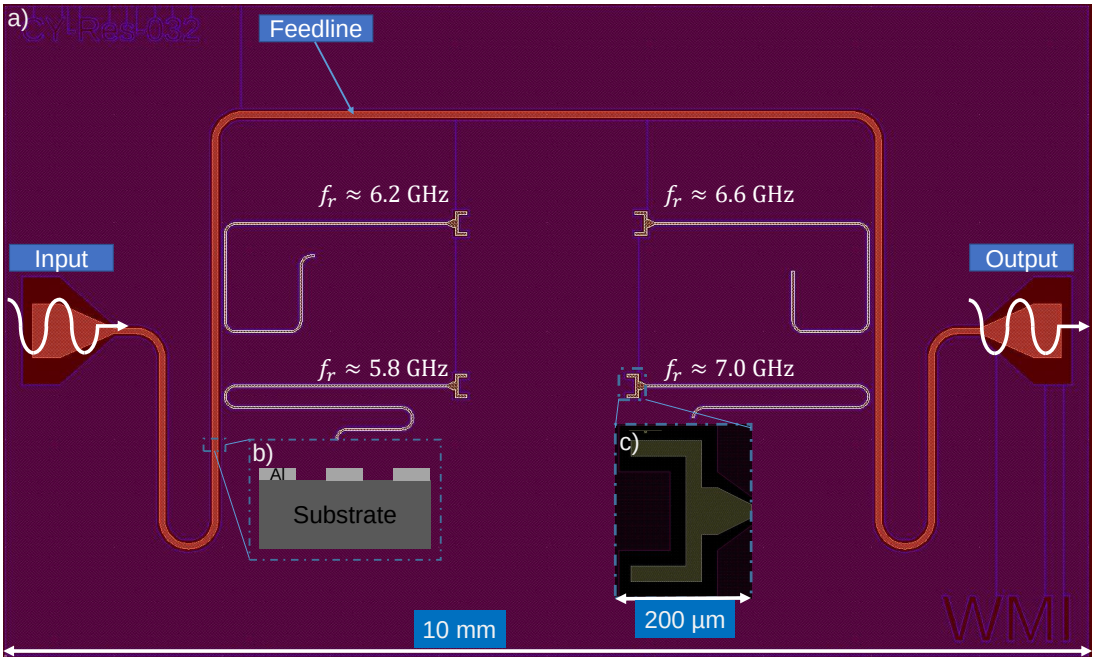

Figure 4.13: Chip layout for resonators. **(a)** The feedline (orange) is seperated by two gaps (dark red) from the ground plane (purple). We couple 4 resonators (yellow) with different resonance frequencies to our transmission line. The two top resonators are strongly coupled while the bottom two resonators show weak coupling. **(b)** Cross section of the feedline. **(c)** Horseshoe structure, which enhances coupling between resonator and the capacitance of an Xmon qubit.

	conductor w (µm)	gap g (µm)	Z_0
Transmission line	50	30	50.514
Resonator	20	12	50.480

Table 4.5: Geometry for transmission line and resonators and their corresponding characteristic impedance Z_0. The values for Z_0 are calculated on microwaves101.com. Additionally, we use wcalc.sourceforge.net to confirm the results.

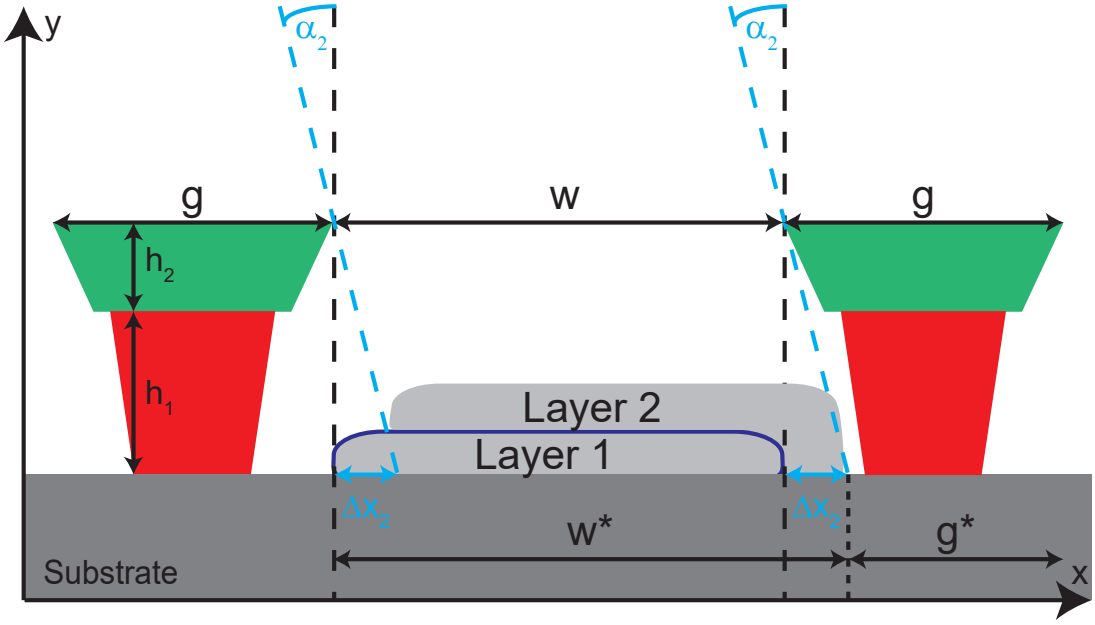

Figure 4.14: Scheme of shadow evaporation for the inner conductor of a resonator. We have $\alpha_1 = 0°$ and no shift. During the second evaporation under an angle α_2, the wire is shifted by Δx_2. Consequently, we obtain a wider conductor of width w^* and a smaller gap g^* on the right hand side.

Note that the resonator chips run through the same fabrication process as the Josephson junctions. That way, we are able to fabricate all structures on a chip during one process. Due to shadow evaporation (55° and 0°), we have a wider conductor w^* and one smaller gap g^*. Assuming a resist thickness of 755 nm (both resists) and an incident angle $\alpha_2 = 55°$, we obtain a shift of $\Delta x = 1078$ nm. Figure 4.14 illustrates this change in CPW geometry. The new geometry and corresponding impedances are summarized in Tab. 4.6. As we have two slightly different gaps, we define $\bar{g} = (g + g^*)/2$ for the impedance calculation.

	conductor w^* (µm)	gap $\bar{g}$ (µm)	Z_0
Transmission line	51.1	29.46	49.93
Resonator	21.1	11.46	49.05

Table 4.6: New geometry of transmission line and resonators due to the influence of the shadow evaporation. Also, their corresponding characteristic impedance Z_0 is shown. The values for Z_0 are calculated on microwaves101.com. Additionally, we use wcalc.sourceforge.net to confirm the results.

Since the conductors are not parallel to the tilt axis along their whole length, the actual impedance change is smaller compared to the values of Tab. 4.6. Using Eq. 2.32 we can calculate the voltage reflection coefficient Γ between microwave input with impedance Z_1 and the transmission line. Since microwave cables are usually matched to $Z_1 = 50\,\Omega$, we obtain a voltage reflection coefficient of

$$\Gamma = \frac{Z_1 - Z_0}{Z_1 + Z_0} = \frac{50\,\Omega - 49.93\,\Omega}{50\,\Omega + 49.93\,\Omega} = 7.0 \cdot 10^{-4} = 0.07\%. \tag{4.5}$$

To sum up, even though we have a shift of up to 5% of the structures' size during shadow evaporation, we obtain a negligible reflection of less than 0.1%. So the new impedance of our feedline ($Z_0 = 49.93\,\Omega$) does not increase microwave reflection at the sample input and output, respectively.

Development

The starting point here is the standard development process with AR-600-56 for 1 minute, IPA for 10 minutes (at 4.5 °C) and a bath of water afterwards. For our analysis, we fabricate vertical wires with different widths (from 250 nm up to 2 µm), across a $6.8 \times 4.2\,\text{mm}^2$ area (Fig. 4.15). For efficiency reasons, we do not cover the whole area but put clusters of 3 rows × 5 columns at 5 relevant positions (sample mid and the 4 borders). The structures closest to the sample edges still have a distance of 0.9 mm (top and bottom positions) and 1.6 mm (left and right) to the substrate borders.
We evaporate three layers of aluminum under different angles (0°, 17° and -17°) and measure the conductor widths. We investigate the influence of different development times and evaporation angles, looking at the fabricated structures with our scanning electron microscope (SEM). An example is given in Fig. 4.16.

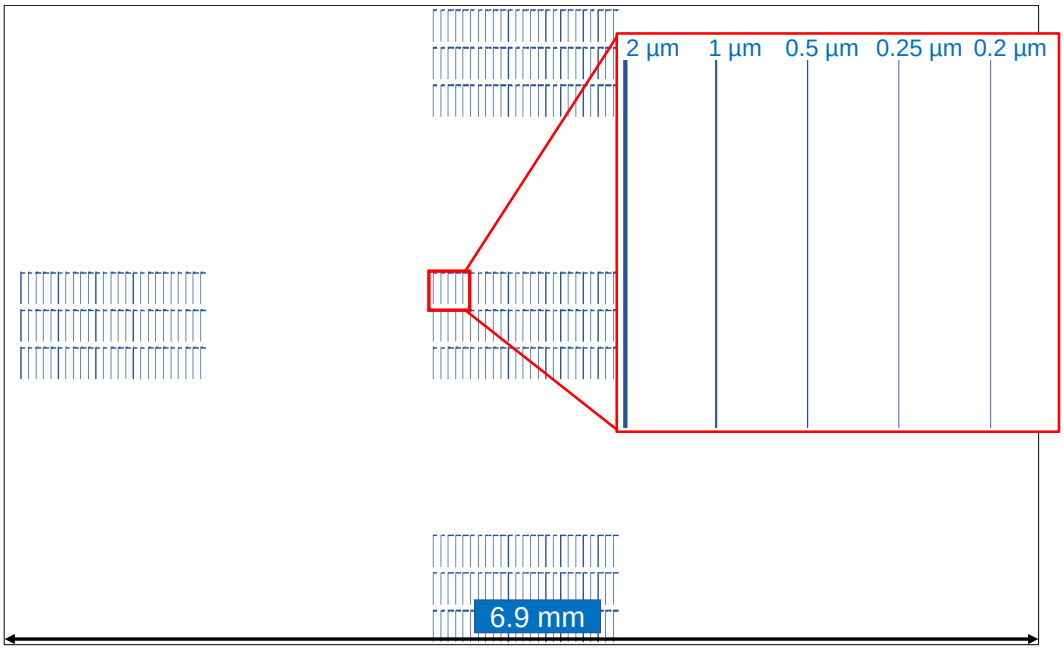

Figure 4.15: Design for development tests. We pattern vertical wires with different widths (from 250 nm up to 2 µm), across a 6.8 × 4.2 mm^2 area. For time effectiveness, we do not cover the whole area, but put clusters of 3 rows × 5 columns at 5 relevant positions (sample mid and the 4 borders). The structures closest to the sample edges still have a distance of 0.9 mm (top and bottom positions) and 1.6 mm (left and right) to the substrate borders.

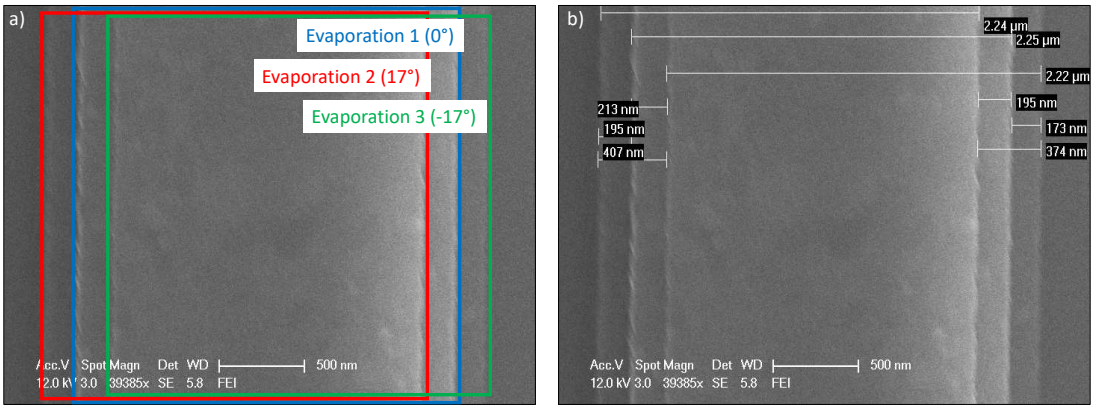

Figure 4.16: SEM pictures of stripes on sample Stripes-001 in the mid area. **(a)** The boxes mark the stripes produced by three evaporation steps. We use angles of 0°, 17° and -17°. **(b)** For better visibility, we show the same image with measurements.

The most important results can be obtained from Fig. 4.17. Here, we plot the relative deviation of a stripe in relation to its nominal width. In particular, we measure the top, mid and bottom of each evaporated conductor and average over those 3 measurements. First, we see that evaporating under $\alpha = 0°$ always implies a higher deviation. Since we have a finite undercut, evaporating under an angle of $\alpha = 17°$ causes a smaller deviation as the structure is partially evaporated onto the remaining resist wall.
Independent of development time and evaporation angle, we see a strongly decreasing deviation for broader structures. A widening of structures is mainly caused by back-scattered electrons close to the patterns border. Consequently bigger structures are less affected. For the samples shown in Fig. 4.17, we apply a very high charge dose of $20\,\mathrm{C/m^2}$ in order to emphasize this effect.

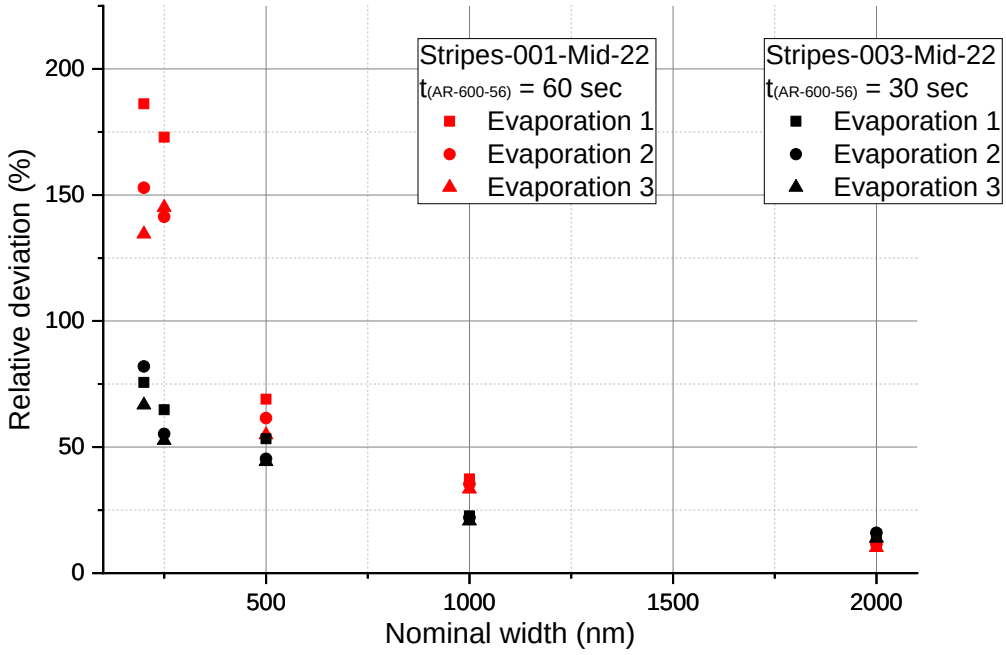

Figure 4.17: Comparison of different development times for stripe structures (red points: $t_{\text{AR-600-56}} = 60\,\text{s}$, black points: $t_{\text{AR-600-56}} = 60\,\text{s}$). First, we see a decreasing relative deviation for wider structures. Second, reducing the development time to 30 s improves the accuracy for smaller structures significantly.

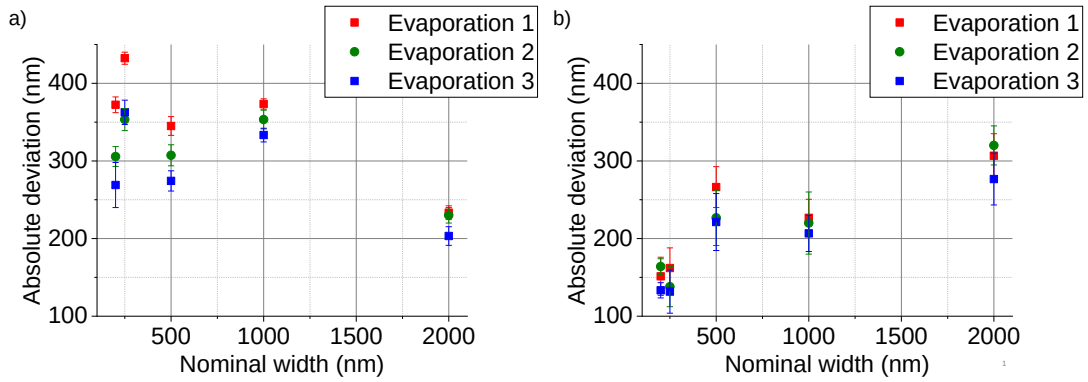

Figure 4.18: Absolute deviation of the stripe widths in relation to their nominal width.
(a) Data of sample Stripes-001 with a development time t = 60 s.
(b) Data of sample Stripes-003 with a development time t = 30 s.

We observe a relatively constant absolute deviation for smaller structures (250 nm - 1000 nm) for 60 s development time [Fig. 4.18(a)]. Reducing the development time to 30 s, we already achieve a significantly smaller error [Fig. 4.18(b)]. The 2 µm stripes are less affected by a shorter development and even show a higher deviation.
Adjusting the applied charge dose during e-beam patterning to 7 C/m^2 gives quite good results (Fig. 4.19) for 60 s development time, because the smallest structures (200 nm width) almost vanish by evaporation under an angle of 17°. During the first evaporation step under a high angle, we want the horizontal conductor of a cross-type junction to be shifted into the resist wall. Therefore, a slightly increased angle is required for the new design.

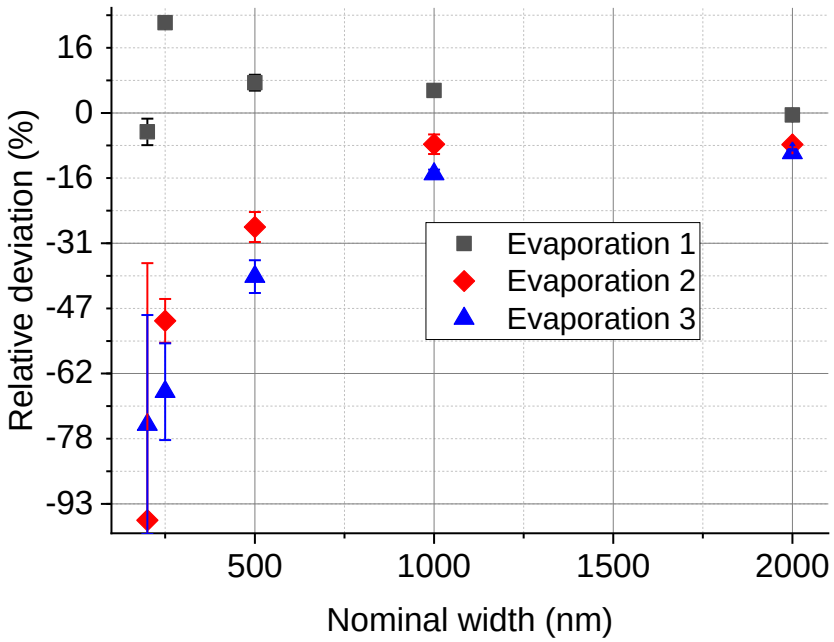

Figure 4.19: Relative deviation of the stripe widths in relation to their nominal width on sample Stripes-004, for a lowered charge dose of 7 C/m^2 and a development time of 60 s.

We see later in Sec. 4.2.1, that - for a viable charge dose - a development time of 30 s causes good results for the cross-junctions. We do not want to decrease the time further, as it then becomes increasingly hard to develop different samples exactly for the same time. It is reasonable to assume a systematic error of ± 1 s.
Subsumming, we have shown that a reduction of development time to 30 s results in a more precise fabrication without losing consistency. We also see a small influence of development time and charge dose for bigger structures. For a viable charge dose, we obtain a deviation of less than 1% for 2 µm stripes, evaporated with $\alpha = 0°$. This means that for our resonator fabrication (structure size of > 10 µm), we do not need a precise control over the development time.

4.1.3 Evaporation and oxidation

The last part of this section covers improvements on evaporation and oxidation. The main changes concern the implementation of a new sample holder into the evaporation chamber, as well as a calibration of the device. Furthermore, we implement two in-situ pre-evaporation procedures, namely Argon-ion-milling and Titanium gettering.
We keep the previous evaporation rate of 10 Å/s. We also do not change the oxidation parameters itself, as previous works have already focussed on this process. However, during our work at WMI, the turbo pump of the main chamber broke and has been replaced. With the new pump, the pressure during oxidation is $p_{\text{oxidation}} = 7.80 \times 10^{-3}$ mbar for a 15% open VAT ventil and an oxygen flow of 8 sccm. The old pump achieved pressures of 7.85×10^{-3} mbar for the same settings. It turns out, that thicker oxide barriers are more reproducible and follow a phenomenological $p^{1/2}t$ law. This results from the Cabrera-Mott theory [43], [44] for the formation of thin film oxide films. The critical current density of a Josephson junction can be expressed as

$$J_c = \frac{\alpha\kappa}{\sinh\left[0.664\kappa\left[\ln(2p^{1/2}t + c)\right]^{2/3}\right]} \tag{4.6}$$

where α, κ and c are material constants.
As we oxidize for 70 minutes, we obtain $p^{1/2}t = 371\ \text{mbar}^{1/2}\text{s}$. For our material system, already around $250\ \text{mbar}^{1/2}\text{s}$, we observe a saturation in critical current density [45]. As we are far above this value, no optimization is required here.

Pre-evaporation procedures

During our work at WMI, we implemented two in-situ procedures directly before evaporation.
First, we perform a so-called argon ion milling with the sputter ion gun GenII from tectra (App. C.2). By coupling microwave energy into a coaxial waveguide and further into an alumina plasma chamber, the oscillating electric fields cause the gas inside to break down and a plasma discharge to take place. We usually let argon gas into the chamber with a flow of 0.5 sccm. Optionally, oxygen can be added into the evaporation chamber. However, this always causes the plasma in our device to break down and we remain with argon only. In principle, this step works similar to the ashing process we described in Sec. 3.1.1. The goal is to remove residual resist in order to obtain a clean substrate-metal interface and reduce the amount of TLS. Later, we analyze the influence of ion milling by comparing resonator losses for different fabrication

parameters in Sec. 4.3.2.
Second, we carry out a titanium (Ti) gettering process. This is applied to improve the vacuum inside the evaporation chamber. Titanium is known to be a good getter material, i.e., it adsorbs molecules inside the evaporation chamber when evaporated under a small rate [46]. The gettering effect (e.g., of oxygen, nitrogen and carbon dioxide) can be observed as a change in pressure.
At room temperature, we slowly increase the current, which heats up the Ti, to approx. 95 mA. This results in an evaporation rate of ≈ 1 Å/s. Note that the shutter must be closed during this step, otherwise we evaporate Ti onto our sample. First, the pressure increases, as Ti fills the chamber. After a certain time, the gettering effect takes place and the pressure decreases slowly. At some point, we observe a saturation in pressure and stop the process. Typically, we evaporate 30 - 40 nm of Ti in accordance with a gettering time of 5 - 7 minutes. We summarize the pressure change for a number of different procedures in Tab. 4.7.

	Evaporated Ti (nm)	p_0 (10^{-8} mbar)	p_{const} (10^{-8} mbar)	p_{after} (10^{-8} mbar)
Without ion milling	30.2	2.15	1.26	< 1.15
Before ion milling	40	0.80	1.65	< 0.82
After ion milling	30.1	5.0	-	< 1.04

Table 4.7: Pressure change due to different titanium gettering procedures, combined with argon ion milling. We read the pressure before (p_0), at the end of the process (p_{const}) and roughly 5 minutes after we stopped gettering (p_{after}). After this time, the pressure still decreases slowly.

We see no change in pressure, if the initial pressure was already good enough ($p_0 = 8 \times 10^{-9}$ mbar). Since the evaporation system is often used multiple times a day, a small volume of dirt particles enters the main chamber every time a sample is exchanged. Often base pressures $> 5 \times 10^{-8}$ mbar can be read off. Additionally, after ion milling, gettering supports the turbo pump by removing argon and resist particles from the main chamber, whereby the pressure decreases more quickly.
With this procedure, we typically achieve pressures of $p = 1.0 \times 10^{-8}$ mbar.

Implementation of new sample holder

The new sample holder carries up to 4 inch wafers (Fig. 4.20). It consists of two step motors, one tilts the sample, the other one rotates it. It is designed by Thomas Brenninger, a WMI engineer, and fabricated by him and the WMI workshop. Together with Thomas, we mount the sample holder and perform first tests. Combining tilt and rotation allows a lot more variety in sample design. However, for the cross-type junctions, standard shadow evaporation is sufficient.

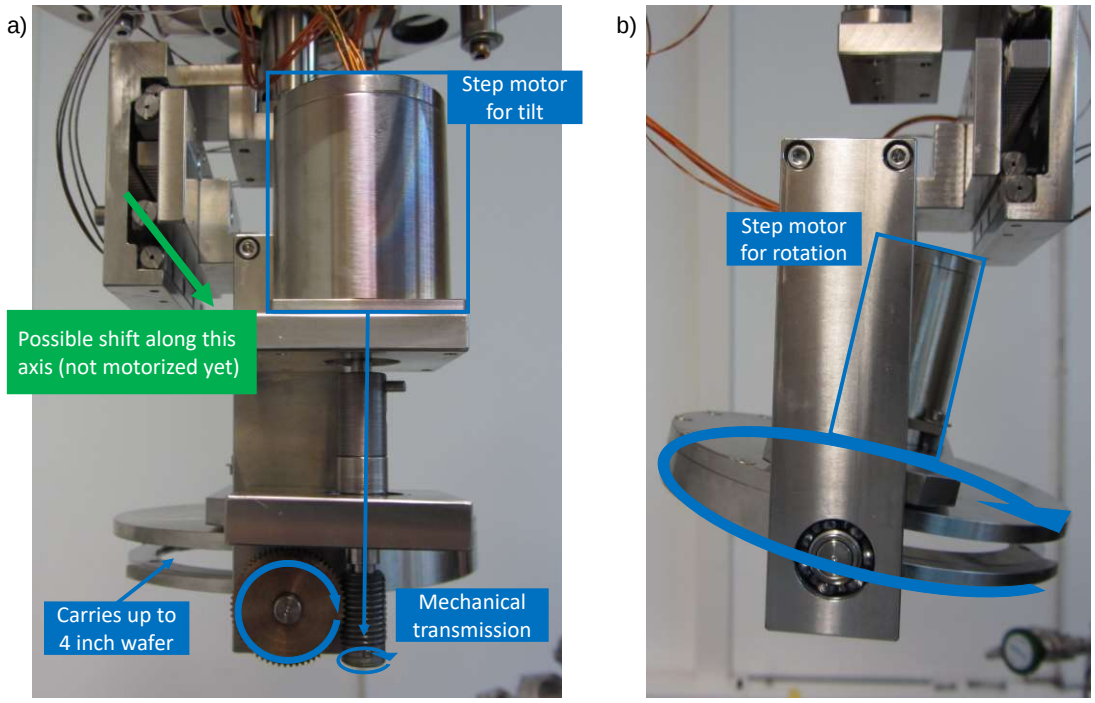

Figure 4.20: Picture of the new sample holder, which carries up to 4 inch wafers. It consists of two step motors, one tilts the sample, the other one rotates it. Additionally, it is possible to shift the whole mount (green arrow).

Before we can fabricate superconducting circuits, we need to calibrate the new sample holder. Besides to general tests, we need to concern an angle and a thickness deviation from the old process.

First, as the mechanical transmission for the tilt motor was not changed, we assume that the angles did not change either. We confirm this by manually tilting the sample holder and measuring the angle.

Second, the evaporated thickness of films might have changed. As the parameters for the evaporation process itself did not change, the distance from sample (holder) to crucible is the only remaining variable. The quartz crystal has not been moved, but the program does not show the correct thickness any more. In order to recalibrate the

crystal, we evaporate 14 samples in total, having nominal thicknesses of 25 to 100 nm (in 25 nm steps). The actual thickness can be obtained via x-ray reflectometry. Similar to white light spectrometry, according to Bragg's law, the incident x-rays are reflected by the aluminum surface and the substrate surface, interfere with each other and are measured in a detector. Instead of wavelength, here we vary the incident angle. Finally, we obtain an oscillatory behavior of intensity with varying angle. The periodicity of oscillation gives information about the thickness. We show a typical measurement in Fig. 4.21. We adapt the parameters in the fit-program Leptos, such that the minima and maxima of the simulated curve (red) fit best to the measurement (black). Sometimes, we observe a phase shift of $\pi/2$ between simulation and measurement over the total angle range. That way it is not possible to find a thickness fitting to the whole data. In that case, we fit low and high angle values individually and take the average of both thickness values.

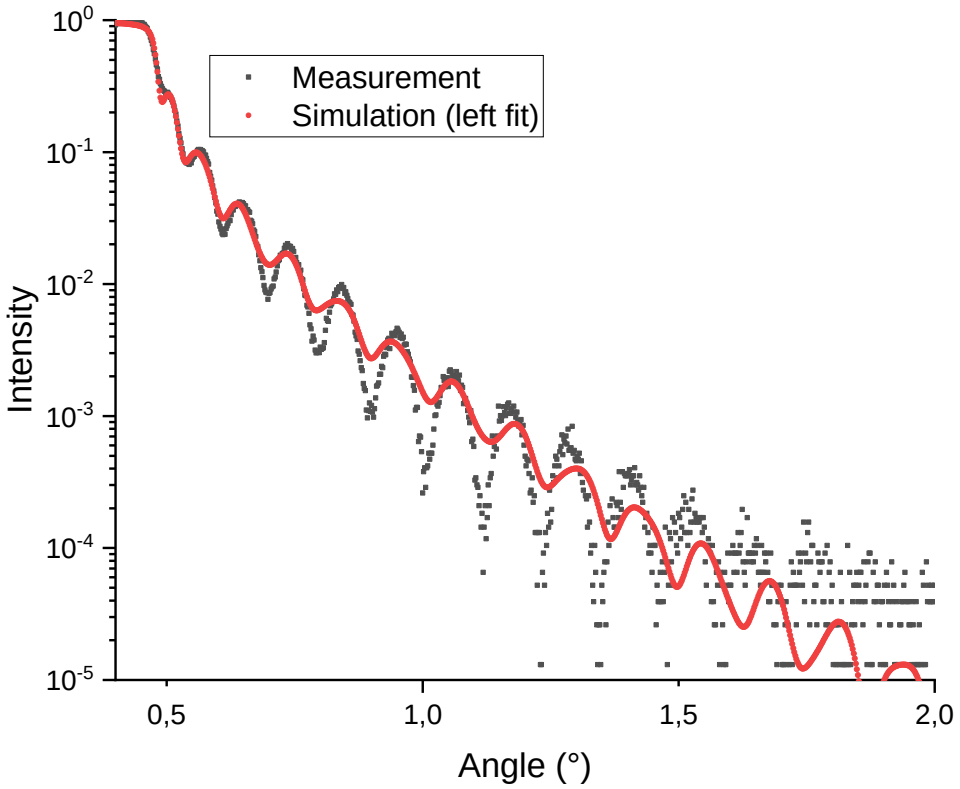

Figure 4.21: Typical XRD measurement (black dots) with a simulation of our material sytem (red curve). The deviation occurs, e.g., due to a different surface roughness or material density. However, the thickness of the aluminum layer depends mainly on the periodicity of the oscillations, which show good agreement between measurement and simulation.

Finally, we plot the measured thickness in relation to the nominal value (Fig. 4.22). Performing a linear fit, we obtain a slope of $m = 0.95$. Inserting this so-called turing-factor into the LabVIEW program controlling the evaporation system, we recalibrate the system to obtain the correct thickness.

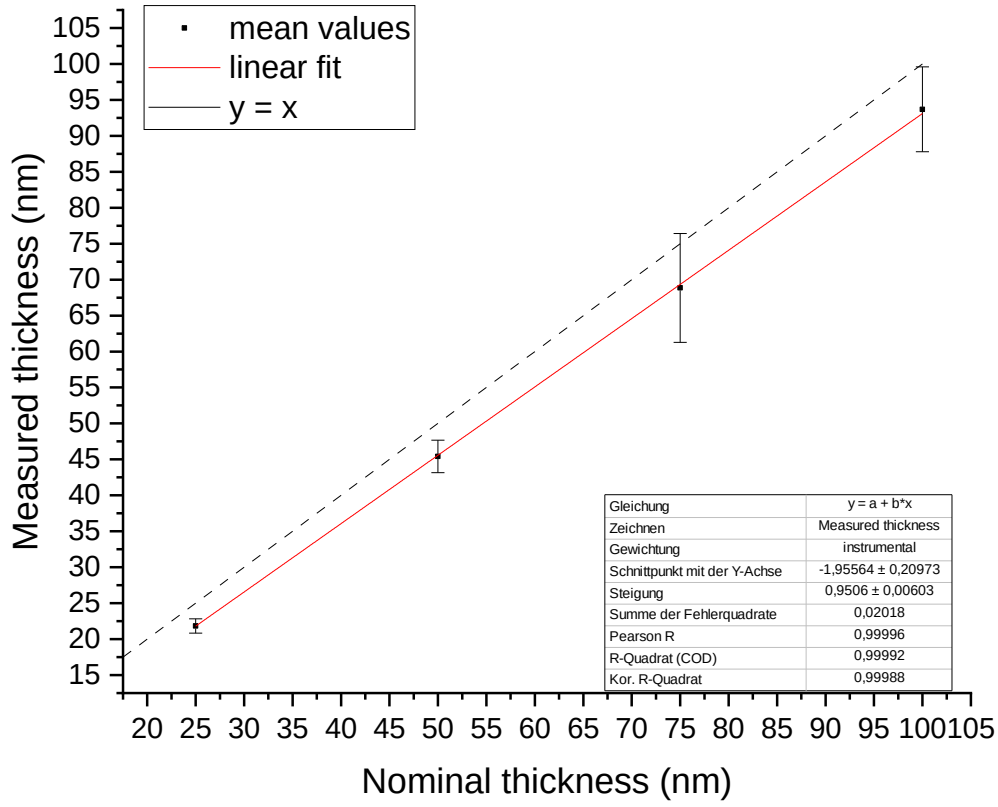

Figure 4.22: The graph shows the mean values of the measured film thickness versus nominal thickness. From a linear fit, we can extract a slope of $m = 0.95$. This so-called turing-factor is put into the LabVIEW program controlling the evaporation system in order to recalibrate the evaporated thickness of aluminum films.

Lift-off

As last improvement on the fabrication process, we slightly adapt the lift-off process. Instead of one bath in acetone, we heat the sample in a second bath at 70 °C. The sample is heated for 60 minutes in each bath. Afterwards, instead of stirring with a pipette, we put the beacon with hot acetone into the supersonic bath for 1 minute at lowest power (level 1). Next, the sample is flushed with IPA in order to remove residual acetone and metal on the surface. Finally we put the sample into two different beacons with deionized water for a few seconds each time. This way residual IPA is removed. As last step, the sample is blown dry with nitrogen.

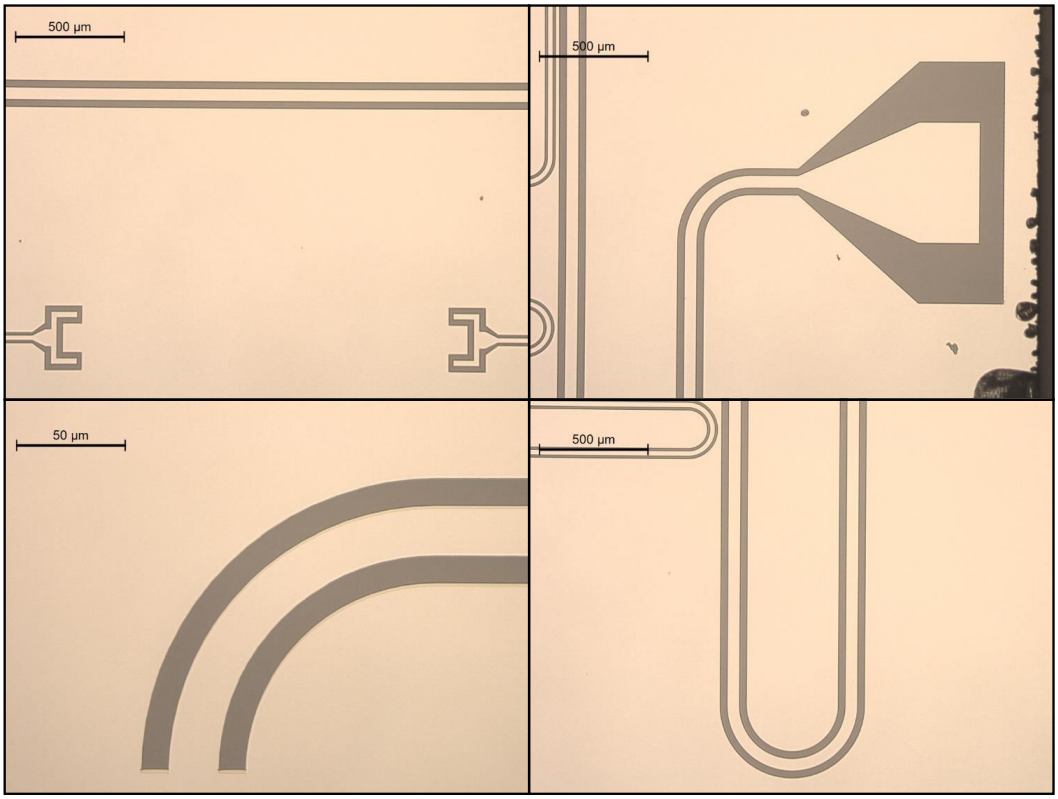

Figure 4.23: Optical micrographs of sample Res-026 after the lift-off process. Adding a second heating in acetone for 60 minutes and using the supersonic bath for removal of aluminum results in a consistent lift-off across the whole sample. A clear improvement over the original process (Fig. 3.9) can be observed.

4.2 Room temperature resistance measurements

In the second part of this chapter, we want to investigate the fabrication of the new cross-type junctions. First, we focus on a mere structural analysis by measuring the junction area with the help of a scanning electron microscope (SEM). Second, we measure the room temperature resistance of many junctions in order to obtain the critical current density and investigate the stability of the fabrication process.

4.2.1 Influence of charge dose and chip position on junction area

With regard to the structural analysis, we measure the overlap area of each junction on sample SQUID-011. We split the chip into 6 equal areas and average over 48 junctions per area. Within each area the charge dose for the junction layer varies between 5 and 8.5 C/m^2. The results are shown in Fig. 4.24. Note that the standard deviation increases due to the charge dose variation, which affects the overlap area. In total, we obtain area values between 0.068 μm^2 and 0.083 μm^2. Although we have some variations, we cannot observe any specific position dependency for the junctions.

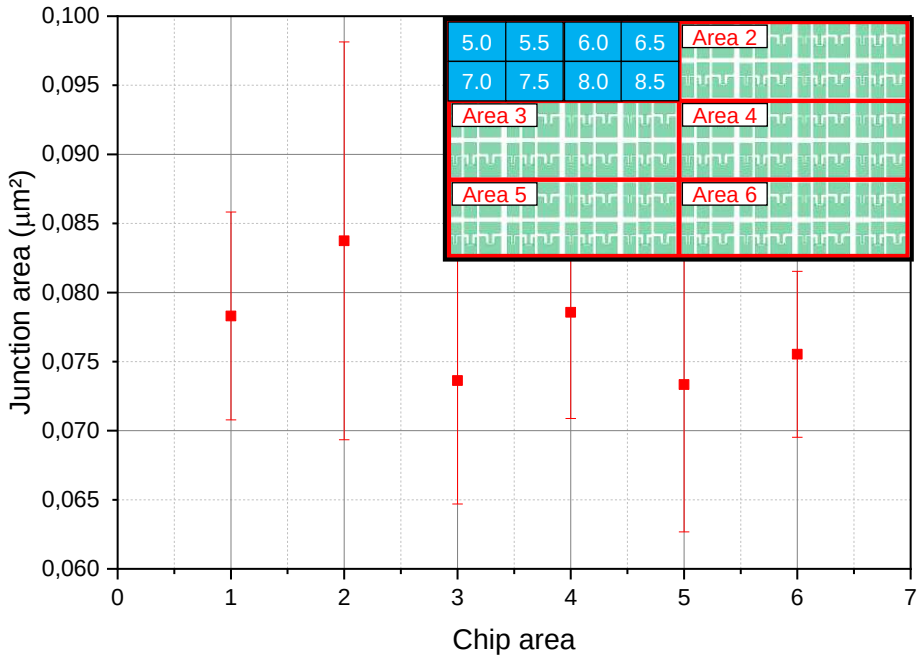

Figure 4.24: Mean values of the junction area for different chip areas. The inset shows the sample design with the specific areas (red boxes). Within the blue boxes the applied charge dose is shown in $\mathrm{C/m^2}$. The nominal junction area is 0.04 $\mu\mathrm{m}^2$ for all junctions.

Next, we want to investigate the influence of the charge dose. From our measurements, we can clearly see an increasing conductor width with higher doses, saturating at $8\,\mathrm{C/m^2}$. At the same time, the bridge width decreases due to a higher amount of reflected electrons which destroy polymer chains in the resist, even outside of the desired area. The widths of conductors for different charge doses are summarized in Tab. 4.8. We also notice, that the horizontal conductor is always bigger than the vertical one. This effect simply follows from the smaller resist bridge. Usually, the applied charge dose around the bridge is higher due to the ghost layer, enhancing this effect.

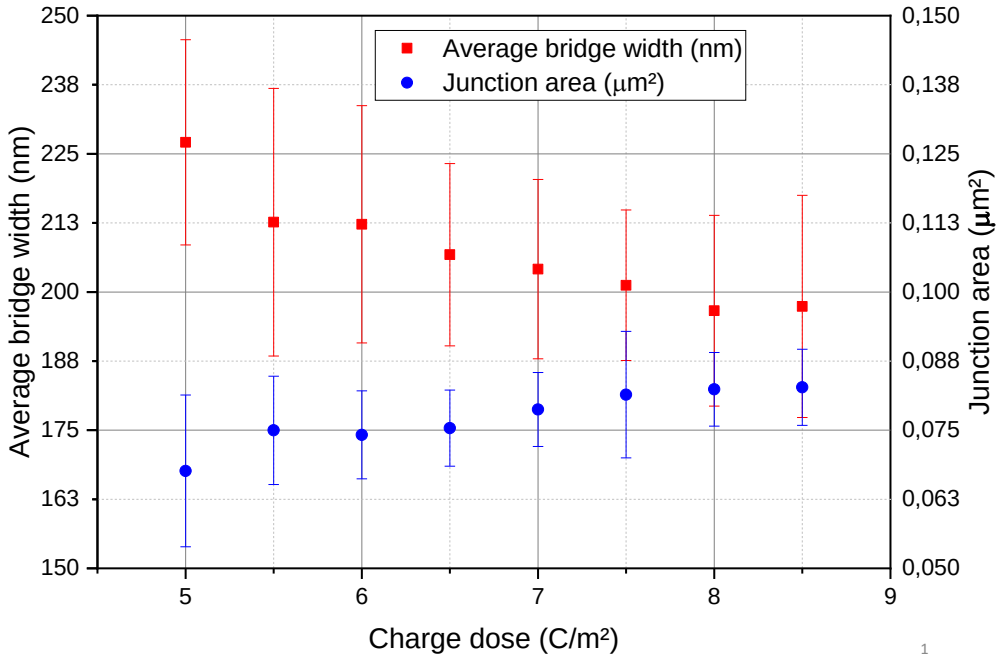

Figure 4.25: Influence of charge dose on the bridge width (blue data points) and junction area (red data points). Higher charge doses result in a smaller bridge width. Due to the smaller bridge width, the horizontal conductor widens, which results in a bigger junction area.

Charge dose (C/m^2)	w_v (nm)	w_h (nm)
5.0	242.81	288.28
5.5	252.56	296.11
6.0	246.90	299.67
6.5	251	299.89
7.0	255.83	307.48
7.5	263.77	308.42
8.0	265.19	310.64
8.5	264.81	312.28
Average	255.36	302.84

Table 4.8: Measured conductor widths for different charge doses. The nominal width is 200 nm for both conductors.

4.2.2 Resistance measurements

Now that we analyzed the junction structure in detail, we want to focus on room temperature resistance measurements. Therefore, we plot the measured resistance for each SQUID on sample SQUID-034 (Fig. 4.26). Here, each square represents a single SQUID loop. We chose a span of 0.1 - 15 kΩ as viable values for a measurement. Typically not the junction itself is broken, but instead the leads are interrupted (Fig. 4.27). This would result in a vanishing current during voltage sweep and therefore to an infinite resistance. If there's a SQUID outside of the chosen range, it is shown as white square in the colorplot. In agreement with Fig. 4.24, we cannot observe any position dependence.

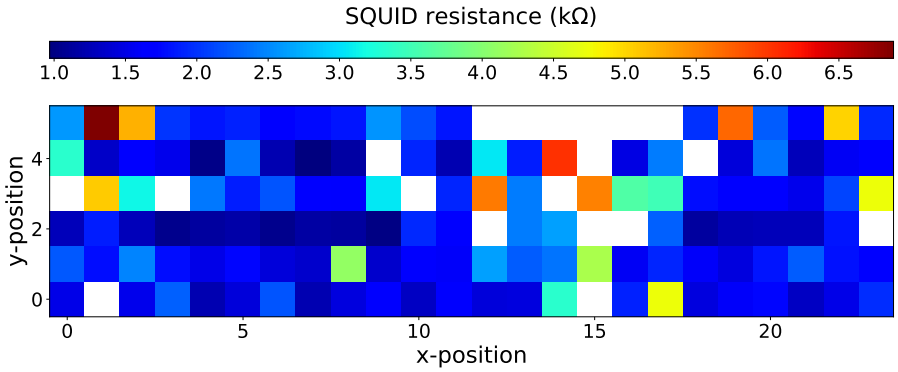

Figure 4.26: Resistance values for each SQUID on sample SQUID-034. Each square represents one SQUID, while the color shows the resistance value. x- and y-position are chosen as integer numbers, where (x, y) = (0, 0) corresponds to the bottom left SQUID.

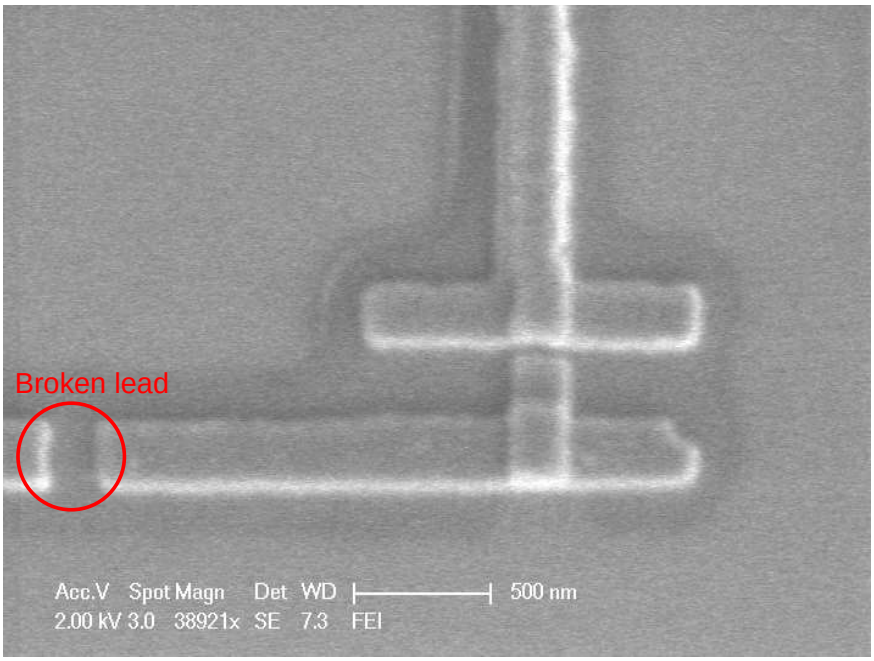

Figure 4.27: SEM image of a cross-type junction with a broken horizontal conductor.

Statistical analysis

Now that we have an overview over our junction fabrication, we want to investigate the measured resistances in detail. First, we look at the resistance in dependence of charge dose (Fig. 4.28). Assuming a constant current density, the resistance decreases with increasing junction area. In regard to Fig. 4.25 we see the expected behavior for the resistance by changing the charge dose.
In contrast to the resistance, we expect an opposite trend for the critical current. It can be calculated by Eq. 2.9. In Fig. 4.29 we observe the expected increase in current with charge dose. This indicates a stable oxidation process (and therefore a constant critical current density).

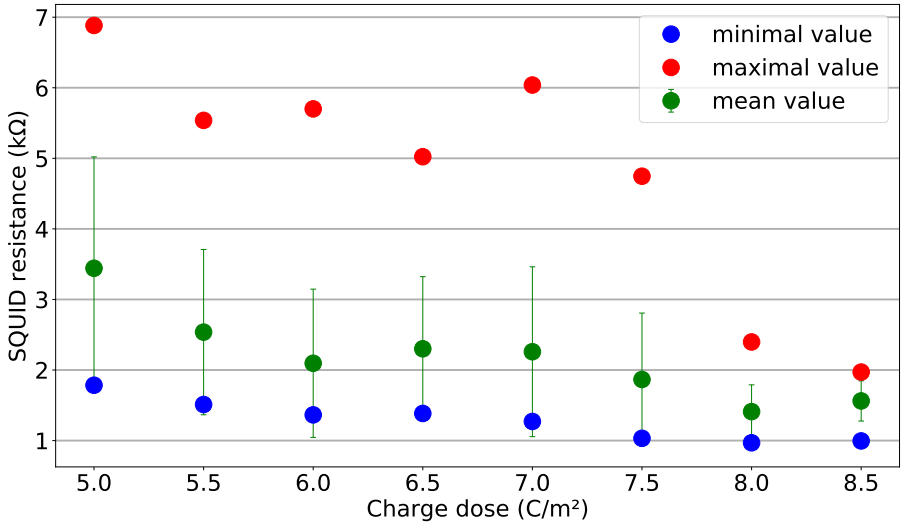

Figure 4.28: Mean, min and max values of the SQUID resistance for different charge doses for sample SQUID-034.

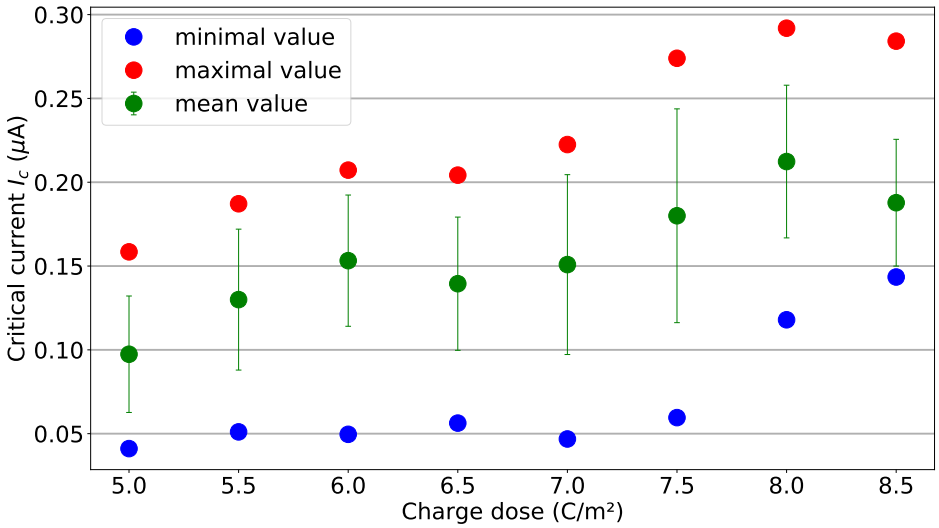

Figure 4.29: Mean, min and max values of critical current I_c for different charge doses for sample SQUID-034.

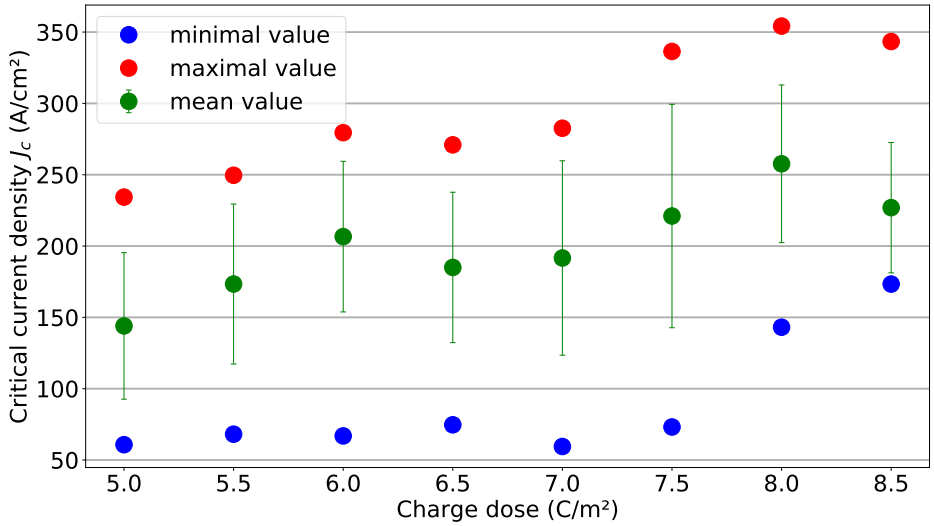

Figure 4.30: Mean, min and max values of critical current density J_c for different charge doses for sample SQUID-034.

Using the measured areas from Fig. 4.25, we can calculate the mean critical current density for each charge dose (Fig. 4.30). Here, for each charge dose, we divide every critical current value of Fig. 4.29 by the average area from Fig. 4.25. Unfortunately, we cannot measure the junction areas of sample SQUID-034 due to problems with the SEM. However, we gain still insight into the junction stability. Looking at the mean values, the average current density is $J_c = 201\ \mathrm{A/cm^2}$. For comparison, a typical value for the current density is $J_c = 26.5\ \mathrm{A/cm^2}$ for $R_n = 4.25\ \mathrm{k\Omega}$ and $A = 350\ \mathrm{nm} \times 350\ \mathrm{nm}$ [47]. This discrepancy might result from a different oxidation process. In general, the current density can be decreased by an additional annealing.
With a minimal mean current density of $J_c^{max} = 144\ \mathrm{A/cm^2}$ and a maximum value of $J_c^{max} = 258\ \mathrm{A/cm^2}$ we find a spread of ±28%. This value seems rather high, but is small compared to the spread of critical currents I_c (approx. ±80% around the average).

As last step in our analysis, we plot a histogramm of the number of SQUIDs for a certain resistance interval in Fig. 4.32. Here, we split the measured resistances into 30 intervals of $\Delta I \approx 0.20\,\mathrm{k\Omega}$ from maximal to minimal value. We see that most SQUIDs have resistances between $1\,\mathrm{k\Omega}$ and $2.6\,\mathrm{k\Omega}$. From the histogram, we find a peak at $R_\mathrm{n} = 1.8 \pm 0.1\,\mathrm{k\Omega}$. Around that maximum, we define a yield

$$Y(\Delta I) = \frac{\text{Number of SQUIDs within } \Delta I}{\text{Number of SQUIDs on chip}} \tag{4.7}$$

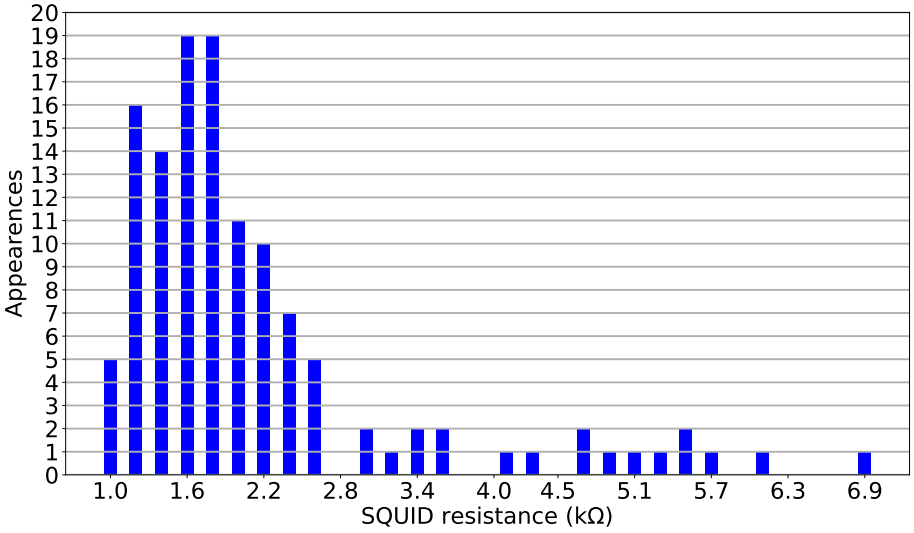

Figure 4.31: Number of appearences per SQUID resistance.

The yield for different interval lengths is shown in Tab. 4.9 for 144 SQUIDs in total on one chip.Within an interval of $0.2\,\mathrm{k\Omega}$ we only have a yield of 34%. Besides statistical fluctuations, the variation of charge dose additionally increases the spread in resistance and explains the low yield. For a reasonable result, we have to increase the interval width to $\pm\,0.8\,\mathrm{k\Omega}$.

ΔI (kΩ)	$\Delta I / R_\mathrm{n}$(%)	Yield $Y(\Delta I)$ (%)
0.2	11.1	34.0
0.4	22.2	50.7
0.6	33.3	66.7
0.8	44.4	73.6

Table 4.9: Yield for different intervals ΔI around a peak of $R_\mathrm{n} = 1.8\,\mathrm{k\Omega}$.

Outside of that interval, we also observe SQUIDs with higher resistances (> 2.8 kΩ). We assume that we have broken leads in one SQUID arm and/or damaged leads here. In Fig. 4.32 and Fig. 4.33 we show a histogram for each individual charge dose. From this analysis we can extract two results: First, in agreement with the increasing junction area from Fig. 4.25, we again observe a lower resistance for increasing charge dose. Second, the spread tends to decrease for higher charge dose while the yield increases. We assume, that with higher charge doses less resist remains on the sample, which might cause structural damage or influences on the oxide barrier.
However, more experiments are needed in the future. In such experiments, fabricating single junctions rather than SQUIDs should lead to a more accessible analysis.

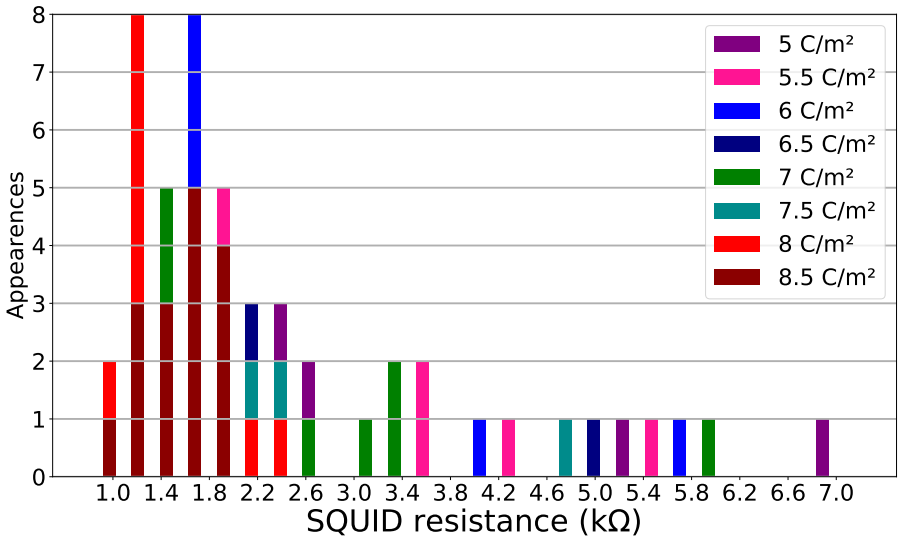

Figure 4.32: Number of appearences per SQUID resistance for each charge dose. We observe a shift of the resistance peak to lower values for higher charge doses in agreement with bigger junction area. Further, the resistance spread also decreases for higher charge doses.

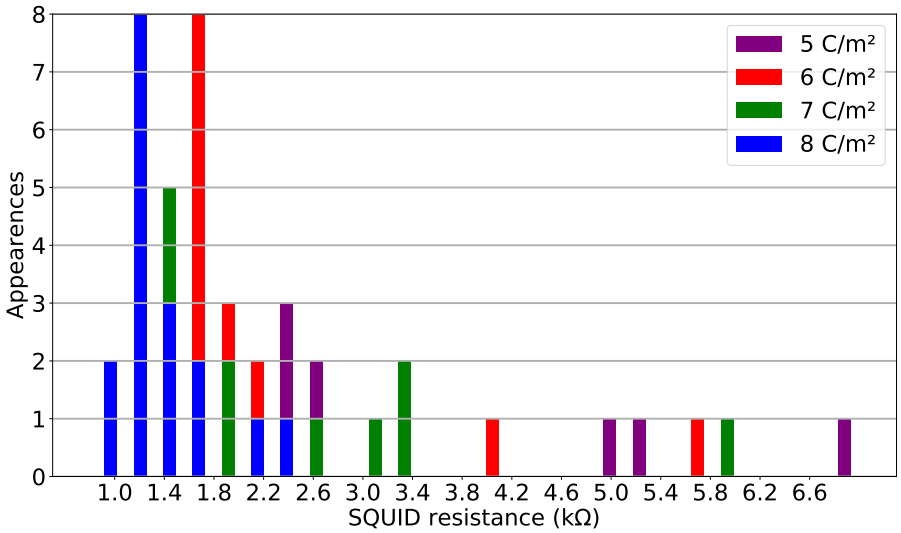

Figure 4.33: Number of appearences per SQUID resistance for each charge dose with even number. We observe a shift of the resistance peak to lower values for higher charge doses in agreement with bigger junction area. Further, the resistance spread also decreases for higher charge doses.

4.3 Resonator measurements

In the last part of this chapter, we want to investigate the quality of our resonators by performing transmission measurements, as described in Sec. 2.4. In particular, we have a closer look at the total internal losses of our resonators and compare different cleaning methods as well as ion gun treatment (see Tab. 4.10). Note, that for sample Res-046, we only have weakly coupled resonators according to the bottom left resonator in Fig. 4.13.

Sample	Cleaning	Argon ion milling
Res-005	Standard	No
Res-026	Oxygen ashing (3 min)	Yes
Res-035	Argon/oxygen ashing (3 min)	Yes
Res-046	Oxygen ashing (3min) + HF treatment	No

Table 4.10: Fabrication details for resonator samples.

4.3.1 General measurement procedure and loss extraction

First of all, we present the procedure for a resonator measurement. In general, we perform a transmission measurement for each resonator at 9 different temperatures from 50 mK up to 290 mK. For each temperature, we vary the input power between -90 dBm and 40 dBm. Room temperature noise in the microwave probe signal is suppressed by attenuators at various temperature stages with a total attenuation of 70 dB. Afterwards, we insert the data into the fit algorithm from Qiming Chen, as described in Sec. 2.4. In Fig. 4.34, we plot the internal losses obtained from a typical measurement. Here, the measurements at three temperatures are shown. At high input power, we can extract thermally induced quasiparticle losses δ_{qp} by looking at different temperatures. At low input power, TLS losses dominate and we can calculate δ^0_{TLS}.

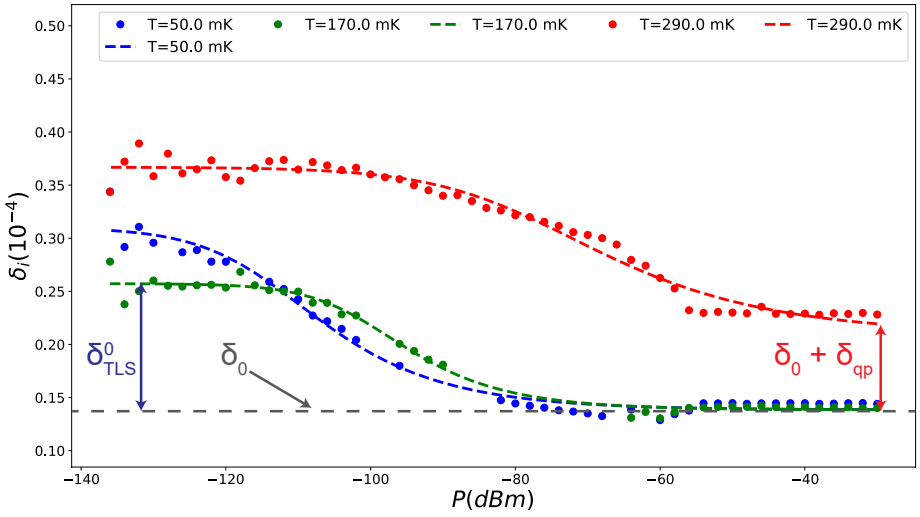

Figure 4.34: Internal losses δ_{i} of resonator 1 with $f_{\mathrm{r}} = 5.82$ GHz on sample Res-005 vs. power. We show the measurements at three different temperatures.

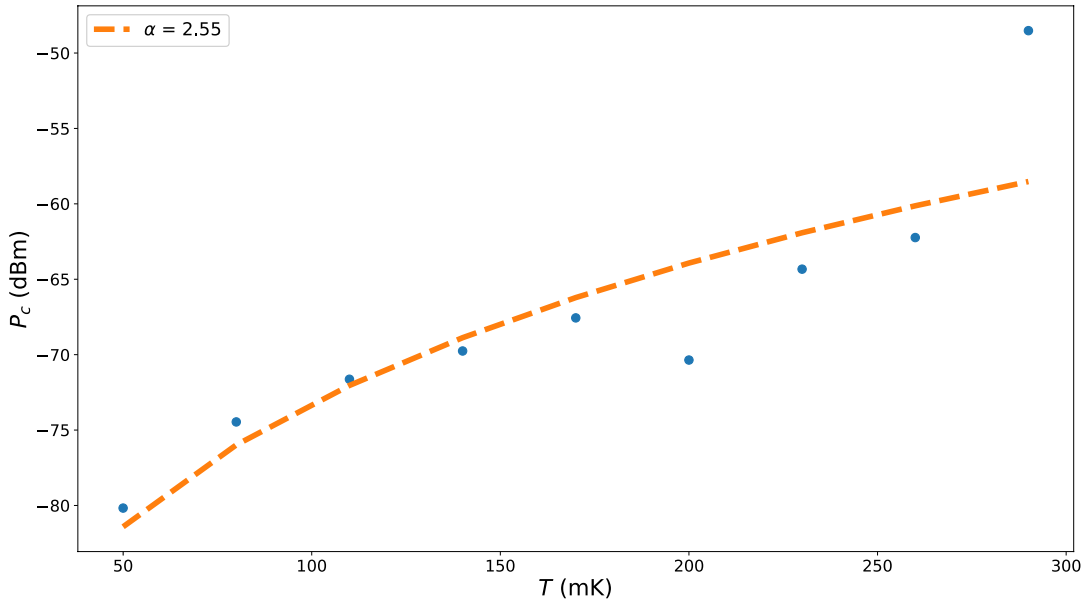

Figure 4.35: Temperature dependency of characteristic power P_c for resonator 1 with f_r = 5.82 GHz on sample Res-005. We obtain α by fitting Eq. 2.70 to the measured values of P_c. The orange dashed line shows the fit according to Eq. 2.70.

We also have a look at the characteristic power P_c for different temperatures in Fig. 4.35. Fitting Eq. 2.70 to the values of $P_c(T)$, we obtain α. From our fits, we typically obtain values $\alpha \approx 2-3$ in good agreement with Ref. [28]. Next, the values of β and δ^0_{TLS} are obtained by fitting Eq. 2.69 to the internal losses vs. power. The parameters are shown in Tab. 4.11.

Sample	f_r (GHz)	P_c(50 mK, W)	α	Average β
Res-005	5.82	$9.56 \cdot 10^{-9}$	2.562	0.70
	6.21	$2.18 \cdot 10^{-8}$	2.19	0.57
Res-026	5.77	$5.74 \cdot 10^{-9}$	0.92	0.57
	6.14	$2.02 \cdot 10^{-9}$	-10.52*	0.83
	6.56	$1.77 \cdot 10^{-9}$	2.02	1.88 (at 50 mK)
	7.02	$8.19 \cdot 10^{-11}$	2.93	0.52
Res-035	5.75	$4.02 \cdot 10^{-10}$	0.45	0.55
	7.00	$8.15 \cdot 10^{-11}$	2.81	1.57

Table 4.11: Fit parameters for different resonators. The $*$ marks unphysical values.

4.3.2 Loss analysis

From our measurements, we can now extract the different loss contributions. Internal losses δ_i at low power limit, the prefactor δ^0_{TLS} for TLS losses and power independent losses δ_c for some resonators are shown in Tab. 4.12. Note, that we only show results from reasonable fits here. For some measurements, the circle fitting procedure did not show any viable results. The whole data set can be found in the Appendix C.2.
In the following, we analyze each loss mechanism introduced in Sec. 2.5.

Sample	f_r (GHz)	Temp. (mK)	$\delta_i/10^{-5}$	$\delta_0^{TLS}/10^{-5}$	$\delta_c/10^{-5}$
Res-005	5.82	50	3.40	1.70	1.38
	5.82	Average	3.02	1.53	1.51
	6.21	50	17.5	1.79	15.8
	6.21	Average	17.33	1.59	15.89
	6.67	50	149	0.95	148
	6.67	Average	285.37	0.22	310.19
Res-026	5.77	50	3.9	3.1	1.1
	5.77	Average	3.33	1.96	1.57
	6.14	50	13.1	2.31	10.9
	6.14	Average	12.78	1.53	9.79
	6.56	50	116.4	1.15	115
	6.56	Average	111.23	0.64	110.64
	7.02	50	6.0	4.8	1.6
	7.02	Average	5.18	2.77	2.49
Res-035	5.75	50	20.4	2.31	18.2
	5.75	Averages	20.27	1.73	18.71
	6.12	50	330	5.16	325
	6.12	Averages	339.62	513.34	15.06
	7.00	50	6.5	3.29	3.39
	7.00	Averages	5.91	1.90	4.18
Res-046	5.08	50	-	0.255	2.26
	5.72	50	-	<0.5	3.33
	5.99	50	-	0.402	2.66

Table 4.12: Internal δ_i (low power), TLS δ^0_{TLS} and power independent losses δ_c for some resonators. We show the losses at 50 mK and the average loss for all measured temperatures.

TLS losses

First we want to investigate TLS losses. As already mentioned, they can be extracted by measuring the internal loss for different input power. As the substrate-metal inferface has a critical influence on TLS loss, we compare four different cleaning methods (Tab. 4.13).

Sample	Cleaning	Average $\delta_0^{\mathrm{TLS}}/10^{-5}$
Res-005	Standard	1.56
Res-026	Ox. ashing + Ar ion milling	2.09
Res-035	Ar/ox. ashing + Ar ion milling	2.68
Res-046	Ox. ashing + HF treatment	0.39

Table 4.13: Prefactor δ^0_{TLS} of TLS losses for different cleaning methods. We do not consider resonators with $f_{\mathrm{r}} = 6.67, 6.65, 6.65, 6.12\,\mathrm{GHz}$ due to high total loss.

With the standard cleaning process on sample Res-005, we obtain $\delta^0_{\mathrm{TLS}} \approx 1.6 \cdot 10^{-5}$. In comparison to Ref. [28], this value is about 5 times higher ($\delta^0_{\mathrm{TLS,\,Goetz}} = 0.34 \cdot 10^{-5}$) for their sample fabricated with electron beam lithography. Since they sputter-deposit a niobium film, followed by an etching process, the deviation might already arise from the different materials and fabrication.
Adding an ashing process before spin-coating and performing argon ion milling directly before evaporation, the TLS losses seem to increase slightly for both of our methods. However, due to little statistics, more experiments are required in order to draw a proper conclusion. It is unlikely that both, ashing and ion milling, have a negativ effect regarding TLS loss. On the contrary, it has been shown that argon ion milling can drastically decrease TLS loss [28], [48]. We assume, that in our case ion gun treatment has no effect, as our specific ion gun can not achieve optimal parameters.
If we carry out a treatment in hydrofluoric acid (HF) after ashing with oxygen, we observe a 75% decrease in TLS loss compared to standard cleaning. We want to mention, that HF treatment and spin coating for sample Res-046 are performed at the Walter-Schottky-Institute, while the rest of the fabrication process is carried out at WMI. Although there is still room for improvement on the fabrication side, we already see a drastic improvement in the substrate-metal interface.

Quasiparticle losses

We want to have a look at QP loss generated by stray infrared light. From Sec. 2.5.2 we know that our system is only sensitive to radiation above the gap frequency of 87 GHz ($f_{\mathrm{gap}} = 2\Delta/h$, with Δ the superconducting energy gap and h Planck's constant). For that reason, we implement K&L filters in our setup (part number 6L250-00089). The datasheet can be found in the appendix C.1. From the amplitude and VSWR response, we can read off a cutoff frequency of 12 GHz and an attenuation of approx. -62 dB at 16.5 GHz. That means any input signal with frequencies above 16.5 GHz is almost entirely filtered. Consequently, the majority of stray light is filtered and we can neglect its contribution on QP loss.
In Fig. 4.36, we plot the power independent losses for different temperatures. By fitting Eq. 2.73 to our data and setting the ratio of kinetic to total inductance γ as fit parameter, we can investigate loss due to thermally excited QP. For high temperatures ($T = 290$ mK), we measure $\delta_{\mathrm{qp}} \approx 0.7 \cdot 10^{-5}$. Decreasing the temperature the loss also decreases according to the Matthis-Bardeen theory [33], [34]. Reaching about 170 mK, δ_{qp} almost vanishes. Therefore, we can neglect QP contribution when measuring at 50 mK entirely.

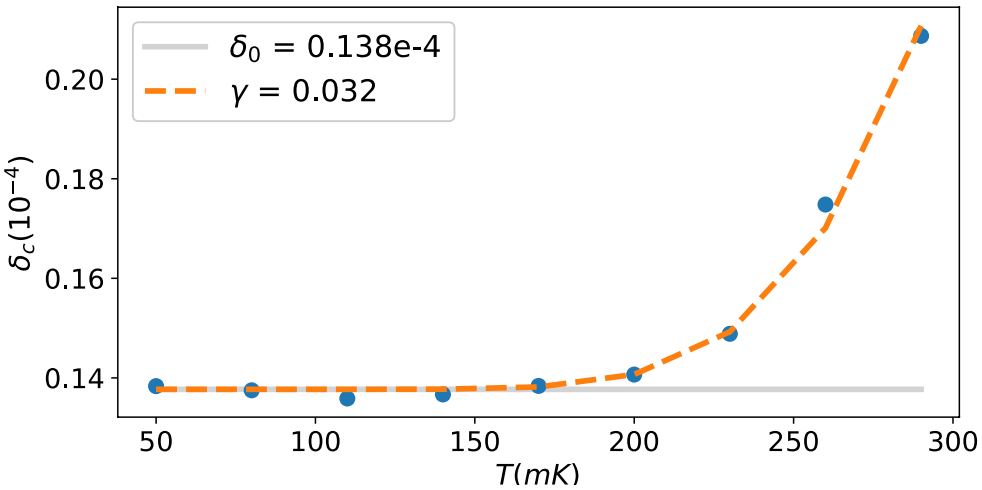

Figure 4.36: Power-independent losses in dependence of temperature for resonator 1 with $f_{\mathrm{r}} = 5.82$ GHz on sample Res-005.

Eddy current losses

In order to estimate eddy current losses in our setup, we first calculate the conductivity of the copper box at low temperature. In comparison to Goetz et al. [28], we use a small amount of GE varnish to attach our sample onto the sample box. Therefore we expect the copper box itself having the most impact on eddy currents. Assuming a residual resistance ratio (RRR) of 50 and a conductity of copper at 300 K of $\sigma_{\mathrm{Cu}}(300\,\mathrm{K}) = 58 \cdot 10^6\,\mathrm{S/m}$, we obtain $\sigma_{\mathrm{Cu}}(0\,\mathrm{K}) = \mathrm{RRR} \cdot \sigma_{\mathrm{Cu}}(300\,\mathrm{K}) = 2.9 \cdot 10^9\,\mathrm{S/m}$. In Ref. [28], they measure power independent losses of $\delta_{\mathrm{c}} \approx 1.2 \cdot 10^{-5}$ at 50 mK using a Si substrate with 525 µm thickness. From a power independent loss vs. thickness plot, they extract $\delta_0 \approx 8 \cdot 10^{-6}$ and $\sigma_{\omega_{\mathrm{r}}}^{\mathrm{Goetz}} \approx 7 \cdot 10^7\,\mathrm{S/m}$. Neglecting quasiparticle loss due to low temperature (Fig. 4.36) and using Eq. 2.68, they obtain eddy current losses of $\delta_{\mathrm{s}}^{Goetz} = \delta_{\mathrm{c}} - \delta_0 \approx 4 \cdot 10^{-6}$.
As our resonators have the same gap size g, we estimate our losses by

$$\delta_{\mathrm{s}} \approx \delta_s^{\mathrm{Goetz}} \cdot \sqrt{\frac{f_{\mathrm{r}} \cdot \sigma_{\omega_{\mathrm{r}}}^{\mathrm{Goetz}}}{f_{\mathrm{r}}^{\mathrm{Goetz}} \cdot \sigma_{\mathrm{Cu}}}} \cdot \frac{l}{l^{\mathrm{Goetz}}} \tag{4.8}$$

Inserting an average resonance frequency for our samples $f_{\mathrm{r}} = 6.4\,\mathrm{GHz}$ and an average length $l = 4.28\,\mathrm{mm}$ and assuming $f_{\mathrm{r}}^{\mathrm{Goetz}} = 4.0\,\mathrm{GHz}$ and $l^{\mathrm{Goetz}} \approx 14\,\mathrm{mm}$, we end up with

$$\delta_{\mathrm{s}} \approx 2.4 \cdot 10^{-7}. \tag{4.9}$$

From our measurements, we obtain losses approx. two orders of magnitude larger. Consequently, we can neglect eddy current losses at the current state of our fabrication.

Radiation losses

We can estimate losses due to radiation by using Eq. 2.75. Inserting the result for $I'(\epsilon = 11.68,\ n = 1) = 1.615$ and the specific geometry of a resonator we obtain $\delta_{\mathrm{rad}} \approx 1.7 \cdot 10^{-5}$. The estimated values for each resonator are listed in Tab. 4.14.

Sample	f_{r} (GHz)	$\delta_{\mathrm{rad}}/10^{-5}$
Res-005	5.82	1.47
	6.21	1.67
	6.67	1.93
Res-026	5.77	1.45
	6.14	1.63
	6.56	1.87
	7.02	2.14
Res-035	5.75	1.44
	6.12	1.62
	7.00	2.13
Res-046	5.08	1.12
	5.72	1.42
	5.99	1.56

Table 4.14: Estimated radiation loss for each resonator. The values are obtained by using Eq. 2.75.

Compared to the values from Ref. [21], our results seem very high at first glance. They calculate $\delta_{\mathrm{rad}}^{\mathrm{ref}} \approx 0.16 \cdot 10^{-6}$ for a 6 GHz resonator. However, they insert $s_{\mathrm{ref}} = w + 2g = 5\ \mu\mathrm{m}$. As δ_{rad} scales with s^2, our geometry with $s_{\mathrm{WMI}} = 44\ \mu\mathrm{m}$ causes this discrepancy. Rescaling gives us:

$$\delta_{\mathrm{rescaled}}(f_{\mathrm{r}} = 6\,\mathrm{GHz}) = \left(\frac{s_{\mathrm{WMI}}}{s_{\mathrm{ref}}}\right)^2 \delta_{\mathrm{rad}}^{\mathrm{ref}} = \left(\frac{44}{5}\right)^2 \cdot 0.16 \cdot 10^{-6} = 1.24 \cdot 10^{-5}, \quad (4.10)$$

which is close to the values around 6 GHz in Tab. 4.14. The remaining deviation results from a slightly different $I'(\epsilon, n = 1)$ and ϵ.
In Ref. [49], the internal quality factor at high power is investigated for different resonator dimensions with resonance frequencies between 2 and 3 GHz. Sage et al. define the radiation loss as:

$$\delta_{\mathrm{rad}}^{\mathrm{Sage}} = \frac{(g + w)^{n_{\mathrm{r}}}}{\alpha}, \quad (4.11)$$

with $\alpha = 2.8 \cdot 10^8$ and $n_{\mathrm{r}} = 2.3$ being fit parameters.

For comparison, inserting our resonator dimension $g + w = (12 + 20)\,\mu\text{m}$, we obtain $\delta_{\text{rad}} = 1.03 \cdot 10^{-5}$ from Eq. 4.11. However, if we also take a frequency (and therefore length) dependency into account by using Eq. 2.75, we obtain $\delta_{\text{rad}}(f_{\text{r}} = 3\,\text{GHz}) = 0.39 \cdot 10^{-5}$ for our design. Although there is some discrepancy, we can take our results as order of magnitude estimation. The estimated radiation losses are in the same order of magnitude as our best power independent losses δ_{c}. Therefore, we have to change our resonator geometry in the future.

Residual losses

Finally, we want to investigate residual power independent losses $\delta_{\mathrm{c,\,resid}} = \delta_{\mathrm{c}} - \delta_{\mathrm{rad}}$. By subtracting the values of δ_{c} at 50 mK from Tab. 4.12 with the estimated radiation losses, we obtain:

Sample	f_{r} (GHz)	$\delta_{\mathrm{c,\,resid}}/10^{-5}$	Q_{e}
Res-005	5.82	≈ 0	296270
	6.21	14.13	6129
	6.67	146.07	762
Res-026	5.77	≈ 0	184764
	6.14	9.27	10271
	6.56	113.13	320
	7.02	≈ 0	43326
Res-035	5.75	16.76	16031
	6.12	13.44*	2361
	7.00	1.26	40237
Res-046	5.08	1.14	49261
	5.72	1.91	27322
	5.99	1.1	44444

Table 4.15: Estimated remaining power independent loss $\delta_{\mathrm{c,\,resid}}$ at 50 mK and external quality factors Q_{ext}, averaged over all temperatures.
$*$: Here, we took the average δ_{c} for calculation.

For three of our resonators, we obtain approx. zero remaining loss, i.e., a faithful estimate of $\delta_{\mathrm{c,\,resid}}$ is not possible in this case. We conclude that these resonators are mainly limited by TLS loss and radiation loss. Both are of the same order of magnitude ($\approx 10^{-5}$).
However, for some other resonators, we observe very high residual loss. Since they are on the same chip as the high quality resonators, it is conceivable that structural discrepancies between them are the source for increased loss. It is conspicuous, that for most of the high loss resonators, the edges of the inner conductor show irregularities (Fig. 4.37), while low loss resonators have mostly smooth edges (Fig. 4.38).

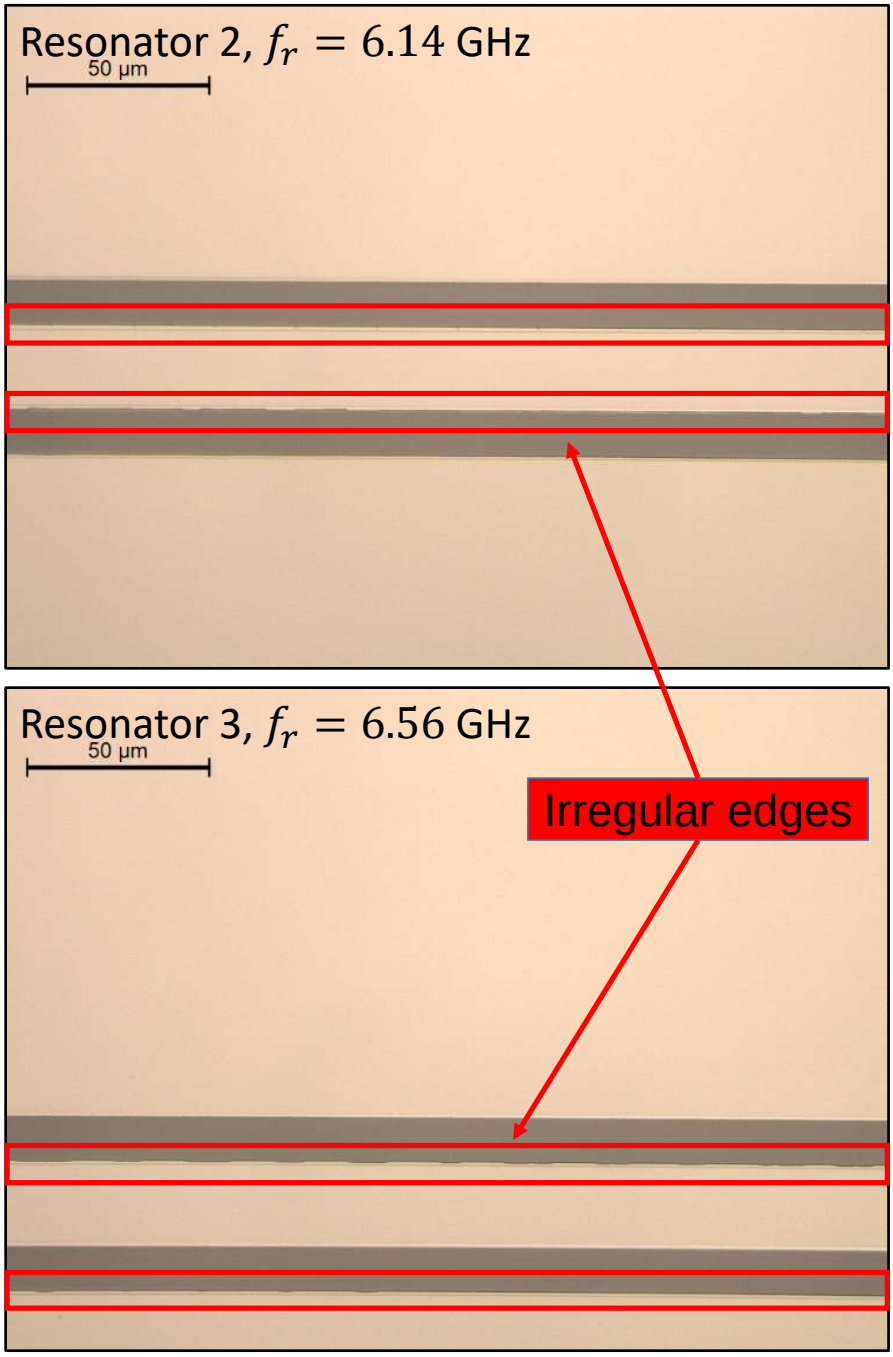

Figure 4.37: Microscope pictures of resonators 2 and 3 on sample Res-026. Both have irregular edges, a possible source of high loss.

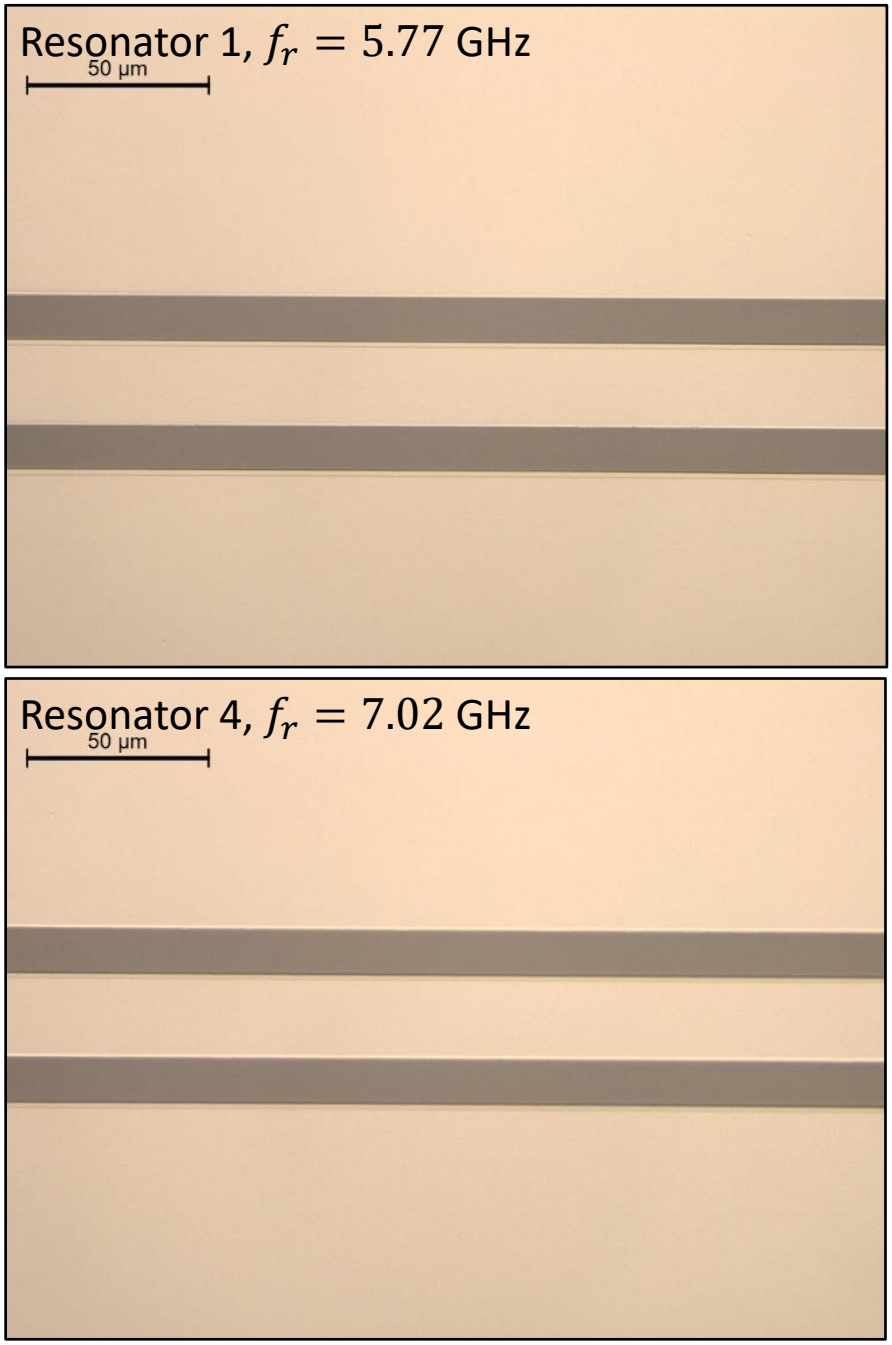

Figure 4.38: Microscope pictures of resonators 1 and 4 on sample Res-026. Both have smooth edges, consistent with the observed low loss.

Another reason for varying values of $\delta_{\mathrm{c,\,resid}}$ might be the different coupling to the feedline. In general, if the external loss is higher than the internal loss ($\delta_{\mathrm{ext}} \gg \delta_i$ or $Q_{\mathrm{e}} \ll Q_{\mathrm{i}}$), the lineshape of the transmission measurement is dominated by δ_{ext} and the accuracy of δ_{i} is reduced [36]. On the other hand, if $\delta_{\mathrm{ext}} \ll \delta_{\mathrm{i}}$ (or $Q_{\mathrm{e}} \gg Q_{\mathrm{i}}$), it is difficult to measure the resonator due to the reduced signal [50]. Thus, in order to measure the internal loss δ_{i} accurately, internal and external losses should be close to each other.

Although it is possible to simulate a specific resonator design and its coupling strength to a feedline, it is hard to pre-determine the internal losses. We have shown the variety of loss mechanisms and the associated challenge in fabrication.

We illustrate the importance of proper coupling by looking at the imaginary part of our signal, $\mathrm{Im}(S_{21})$, in Fig. 4.39 and Fig. 4.40. For a fixed external quality factor of $Q_{\mathrm{e}} = 100\,000$, internal quality factors of $Q_{\mathrm{i}} = 10\,000$ and $Q_{\mathrm{i}} = 30\,000$ can easily be distinguished. Reducing the external quality factor to $Q_{\mathrm{e}} = 1000$, internal quality factors of $Q_{\mathrm{i}} = 10\,000$ and $Q_{\mathrm{i}} = 30\,000$ almost show the same curve. The external quality factors Q_{e} for all measurements are shown in Tab. C.2 in the appendix. By taking a closer look at the resonators shown in Tab. 4.15, we notice a strong correlation between high residual loss and small external quality factor ($Q_{\mathrm{ext}} < 20\,000$). We conclude, that resonators 2 and 3 ($f_{\mathrm{r}}^2 \approx 6.2\,\mathrm{GHz}$ and $f_{\mathrm{r}}^3 \approx 6.6\,\mathrm{GHz}$) on each sample are coupled too strongly to the feedline. Therefore we change the design in sample Res-046, such that all resonators are weakly coupled.

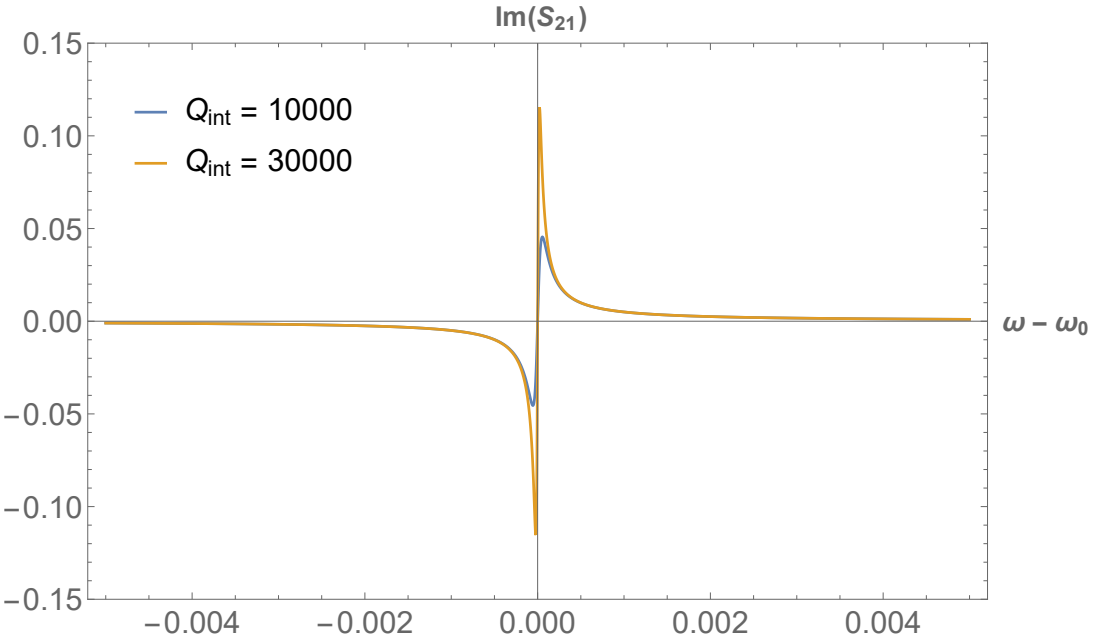

Figure 4.39: Influence of external coupling on the accuracy of the extracted internal quality factor. We show the imaginary part of the signal vs. frequency. Here, ω_0 is the resonance frequency. For a fixed external quality factor of $Q_e = 100\,000$, internal quality factors of $Q_i = 10\,000$ and $Q_i = 30\,000$ can easily be distinguished.

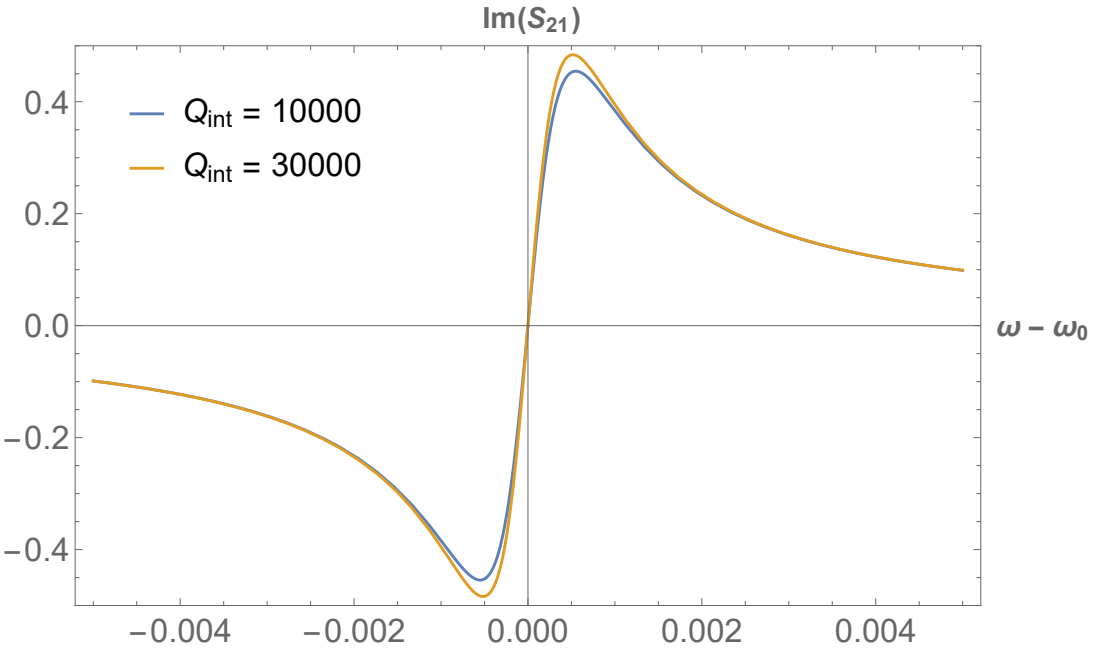

Figure 4.40: Influence of external coupling on the accuracy of the extracted internal quality factor. We show the imaginary part of the signal vs. frequency. Here, ω_0 is the resonance frequency. For a fixed external quality factor of $Q_e = 1000$, internal quality factors of $Q_i = 10\,000$ and $Q_i = 30\,000$ almost show the same curve.

Chapter 5

Summary and outlook

Improvements on fabrication

During the course of this thesis, we have analyzed each step of the current WMI fabriaction process for superconducting circuits. In regard to the cleaning of substrates we show, that an additional ashing in the reactive ion etching chamber increases the quality of our samples significantly. Further, the new cross-type junction is implemented successfully using the new sample holder in the evaporation system. By analyzing the influence of charge dose and development time on structure size, we realize the importance of careful parameter choice for the new junctions on one hand. On the other hand, resonator fabriaction seems less susceptible due to their greater lateral dimension. Finally a slight adaption of the lift-off process significantly increases the total yield during fabrication and shows more consistent results across each sample.

Room temperature resistance measurements

We establish a quick and easily accessible technique to analyze the properties of fabricated Josephson junctions by measuring their room temperature resistance. With the setup described in Sec. 3.2 many junctions can be analyzed within a short amount of time. Using the Ambegaokar-Baratoff relation, we calculate the critical current density J_c, the junction's most important parameter. For the new cross-type junctions, we don't observe a specific position dependence on $6 \times 10\,\mathrm{mm}^2$ silicon substrates, while varying the charge dose during electron beam patterning has a significant impact. In general, higher charge doses (up to $8.5\,\mathrm{C/m}^2$) show less variations and a higher yield in total. On the other hand, small charge doses (down to $5\,\mathrm{C/m}^2$) typically result in a larger deviation with lower yield.

Resonator measurements

The coherence time for many applications in circuit quantum electrodynamics is limited by internal loss channels. Information of the losses can be obtained by measuring the internal quality factor of a CPW resonator. By varying microwave input power and temperature, we extract different loss contributions, such as TLS loss and quasiparticle loss. While TLS loss is mainly affected by the substrate-metal interface, quasiparticle generation can be neglected for low temperatures. For our analysis, we fabricate multiple samples with different cleaning methods in order to improve the substrate-metal interface.

We observe, that additional ashing with oxygen or a combination of oxygen and argon in combination with an in-situ ion gun treatment before evaporation has no effect on TLS loss ($\delta_{\mathrm{TLS}} \approx 2 \cdot 10^{-5}$). We even observe an increase of approx. 33% for oxygen ashing and an increase of approx. 72% for oxygen/argon ashing. In contrary to our measurements, a positive effect of ion gun treatment has been shown [28]. This could arise from our specific ion gun, which can not achieve optimal parameters.

A treatment with fluoric acid (HF) after oxygen ashing already decreases TLS loss by 75% compared to a standard cleaning.

Further, we estimate radiation loss which mainly depends on the resonator geometry, as well as eddy current loss, which depends on substrate thickness and the mount. We calculate a radiation loss within the same order of magnitude as the power-independent loss for many of our resonators.

Eddy current loss is estimated to be in the order of 10^{-7} and not limitating at the current state of our process.

Outlook

With regard to the junction process further experiments are required. By measuring single junctions instead of SQUID loops, the analysis should be more accessible. Higher charge doses as well as an annealing process might lead to further improvement of the stability.
With respect to the resonator fabrication, a slight adaption of design should decrease radiation losses. This can be achieved by choosing a smaller geometry $s = w + 2g$ and fabricating longer resonators (with smaller resonance frequencies). However, scaling down the CPW geometry, the fraction of the electric energy in TLSs and the related loss will increase. Performing an HF treatment already shows improvement on TLS loss and has to be optimized from a fabricational point of view. During the end of our experiments the new Plassys thin-film deposition system was delivered. The new device can be a good alternative to our home-made evaporation system. It also includes an ion gun, operating in a more promising parameter range than the one used in this work. As soon as the internal losses of our resonators are in the order of 10^{-7} we will be limited by eddy currents and we have to consider improving the sample mount.

Appendix A

Blackbody radiation

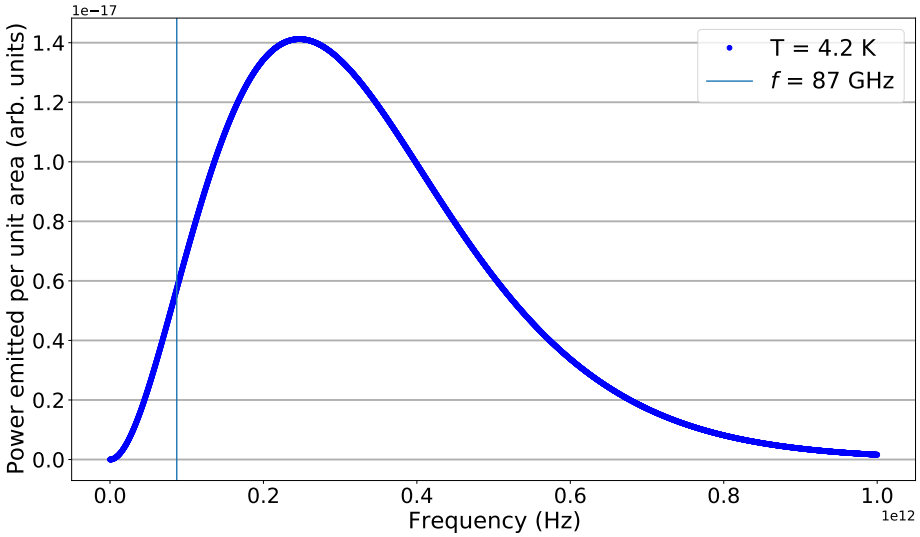

Figure A.1: Power emitted by a black-body at 4.2 K in dependence of frequency.

Figure A.1 shows the emitted power by a black-body at 4.2 K in dependence of frequency. The vertical line shows the gap frequency of aluminum. The curve is calculated by Planck's law of black-body radiation:

$$B_f(f,T) = \frac{2hf^3}{c^2}\frac{1}{\mathrm{e}^{(hf/k_\mathrm{B}T)}-1}, \tag{A.1}$$

where h is Planck's constant, f the frequency, c the speed of light, k_B the Boltzmann constant and T the absolute temperature of the body.

Appendix B

Sample fabrication

B.1 Substrate cleaning

Chemical 1	Acetone
Volume 1 (ml)	10
Heating temperature (°C)	70
Heating time (min)	10
Chemical 2	Acetone
Volume 2 (ml)	10
Heating temperature (°C)	70
Heating time (min)	10
Chemical 3	Isopropylic alcohol (IPA)
Volume 3 (ml)	10
Supersonic bath strength	9
Time (s)	120

Table B.1: Cleaning parameters. We put the sample in the supersonic bath after each step.

B.2 Ashing parameters

General settings	
Pumping pressure (Torr)	$2.0 \cdot 10^{-5}$
RF generator power (W)	100 (98 meas.)
ICP forward power (W)	50 (45 meas.)
APC controller (Torr)	$5.0 \cdot 10^{-2}$
Oxygen ashing	
Oxygen flow (sccm)	50
Argon flow (sccm)	0
Time (min)	3 or 10
Argon ashing	
Oxygen flow (sccm)	50
Argon flow (sccm)	25
Time (min)	3

Table B.2: Ashing parameters. For the oxygen ashing we choose two different times.

B.3 Additional cleaning

Chemical 1	Acetone
Volume 1 (ml)	10
Time (s)	≈ 5
Chemical 2	IPA
Volume 2 (ml)	10
Supersonic bath strength	9
Time (s)	60

Table B.3: Additional cleaning parameters. First, the sample is put into acetone for a few seconds while moving it in circles. Afterwards we flush it with IPA while moving it into another beacon with IPA. Finally we put it into the supersonic bath.

B.4 Spin coating e-beam resist

Bottom resist	PMMA/MA33%
Volume (µl)	440
Rotation speed	2000 r.p.m.
Rotation time (s)	120
Baking time (min)	10
Baking temperature (°C)	160
Top resist	PMMA 950K A2 (AR-P 679.02)
Volume (µl)	220
Rotation speed	4000 r.p.m.
Rotation time (s)	120
Baking time (min)	10
Baking temperature (°C)	160

Table B.4: Spin coating parameters.

B.5 E-beam lithography

SQUIDs	
Current (nA)	≈ 5
Voltage (kV)	80
Charge dose junction layer (C/m^2)	5 to 8.5 (0.5 steps)
Charge dose ghost layer (C/m^2)	0.8
Charge dose contact pads (C/m^2)	5.0
Resonators	
Current (nA)	≈ 18
Voltage (kV)	80
Charge dose (C/m^2)	5.0

Table B.5: E-beam parameters.

B.6 Development

Developer 1	AR 600-56
Temperature (°C)	RT
Time (s)	30
Developer 2	IPA
Temperature (°C)	4.5 to 5.5
Time (min)	10

Table B.6: Development parameters.

B.7 Ion gun treatment parameters

Angle while turning away (°)	20
Argon flow (sccm)	0.5
Pressure (mbar)	$1.3 \cdot 10^{-5}$
Microwave current (mA)	20
Extraction voltage (V)	-600
Extraction current (mA)	0.35
Angle while milling (°)	70
Acceleration voltage (V)	2400
Acceleration current (mA)	≈ 0.1
Time (s)	200

Table B.7: Ion gun treatment parameters.

B.8 Evaporation and oxidation parameters

Evaporation 1	
Thickness (nm)	40
Rate (Å/s)	10
Angle (°)	-55
Oxidation	
Pressure (mbar)	$7.9 \cdot 10^{-3}$
VAT ventil open (%)	15
Oxygen flow (sccm)	8
Time (s)	4200
Evaporation 2	
Thickness (nm)	70
Rate (Å/s)	10
Angle (°)	0
Post-oxidation	
Pressure (mbar)	$7.9 \cdot 10^{-3}$
VAT ventil open (%)	15
Oxygen flow (sccm)	8
Time (s)	2300

Table B.8: Evaporation and oxidation parameters.

B.9 Lift-off parameters

Chemical 1	Acetone
Volume 1 (ml)	10
Heating temperature (°C)	70
Time (h)	1
Chemical 2	Acetone
Volume 2 (ml)	10
Heating temperature (°C)	70
Time (h)	1
Chemical 3	IPA
Volume 3 (ml)	10
Supersonic bath strength	1
Time (s)	60
Chemical 4	IPA
Volume 4 (ml)	10
Time (min)	2
Chemical 5	Water
Volume 3 (ml)	10
Time (s)	10

Table B.9: Lift-off parameters.

Appendix C

Setups and measurements

C.1 AFM measurements

Cleaning method	Standard Cleaning	Oxygen ashing	Oxygen/Argon ashing
Avg. RMS roughness (nm, total grid size)	0.063	0.052	0.083
Top left	0.059	0.056	0.080
Top right	0.063	0.049	0.128
Middle	0.090	0.052	0.075
Bot left	0.052	0.054	0.048
Bot right	0.051	0.048	0.082
Avg. RMS roughness (nm, without grains)	0.052	0.052	0.066
Top left	0.053	0.056	0.080
Top right	0.051	0.050	0.073
Middle	0.059	0.051	0.076
Bot left	0.048	0.054	0.048
Bot right	0.049	0.048	0.052

Table C.1: Root mean square (RMS) roughness according to our AFM measurements. The values are calculated for the whole area (total grid size), as shown in the top half of the table. The bottom half shows measurements without grains, by averaging over 4 smaller areas ($1 \times 5\ \mu m^2$) within one measurement. Therefore, we can neglect high resist leftovers or other dirt and gain more insight into the actual substrate surface.

C.2 Ion gun datasheet

tectra

IonEtch

Sputter Ion Gun, GenII

The tectra IonEtch ion gun is a filamentless ion source based on a microwave plasma discharge. The IonEtch works by coupling microwave energy into a coaxial waveguide and from there via evanescent wave coupling, into an Alumina plasma chamber. The intense oscillating electric fields cause the gas to breakdown and a plasma discharge to take place.

Typical applications:

- sputter cleaning / surface preparation in surface science
- MBE and HV sputter processes
- ion assisted deposition, ion beam sputter coating
- reactive ion etching.

KEY FEATURES AND BENEFITS

- Filamentless Ion Source
- Suitable for use with most gases including reactive ones such as oxygen, hydrogen, …
- No Microwave Tuning. Factory set. Simply turn plasma on / off
- User Configurable
- The ion optics are designed to be quickly and easily exchanged allowing users to customize their source to suit a particular combination of sample size, working pressure and current density
- Easily exchanged apertures enable beam diameter, gas load and current density to be optimized.

A quadrupole field around the chamber further enhances the plasma density via the Electron Cyclotron Resonance (ECR) effect. Ions are extracted from the plasma using a two grid single-hole extraction optics.

The use of microwaves to sustain the plasma allows ions to be extracted at very low energies without the plasma collapsing (down to 25eV) and since there are no hot metal electrodes in the plasma also permits the use of reactive gases such as oxygen and hydrogen.

The GenII is the second generation of the IonEtch sputter gun with some significant improvements in performance and features. To name only some: higher total beam current, high efficiency direct microwave coupling without need of tuning, Alumina plasma cup now standard, only 4 screws to undo non-bakeable parts and more compact, space saving air side setup.

Integration of the robust microwave generator and the ion source, mean that no tuning of the source is required and there is no waveguide to construct or install.

Due to the evanescent wave coupling, no electrodes are present in the plasma i.e. no filaments or other metal. The plasma is entirely surrounded by alumina or other dielectric materials e.g. Boron Nitride (BN). Therefore the source is also suitable for use with reactive gases such as oxygen and hydrogen. A selection of grids and grid conductances allow the optimum balance between gas flow, working pressure and beam current to be achieved.

SPECIFICATION

Dimensions

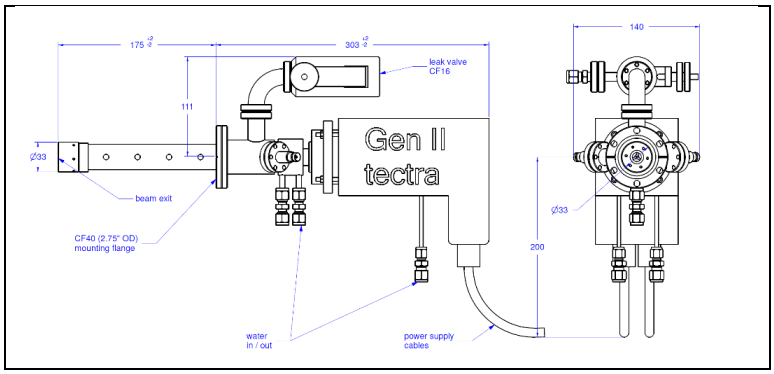

Technical Specification

Source	Microwave Plasma Discharge (No Filament)
Source Diameter	33 mm (Vacuum Side)
Ion Energy	25 eV – 5 keV
Total Beam Current	~ 0.5 mA (at 5kV with Ø1,5mm aperture and Argon),
	~ 2 mA (with Ø3mm aperture and Argon)
Beam Divergence	Dependent on Ion Energy (typically 15°)
Working Distance	100 mm (typically)
Mounting	CF35 (2.75" O. D.)
Gas Inlet	CF16 (1.33" O. D.)
Leak Valve	Required (not included)
Gas Flow Rate	1 – 5 sccm (1.5 sccm typical, gas dependent)
Working Pressure	~ $5x10^{-5}$ mbar to $2x10^{-4}$ mbar
	(without optional differential pumping)
	Low 10^{-6} mbar range possible at reduced beam current

Power Supply

Power	230 VAC / 50 Hz (Standard)
	115 VAC / 60 Hz (to be stated with order)
Size	19" rack mount, 3U height

Options

Gas	Mass Flow Controller
	Differential Pumping
	Different Apertures
Control	Remote Control Options

Please contact us for more Information.
We and our team behind us will be happy to help you!

tectra GmbH
Reuterweg 51 – 53
60323 Frankfurt/M.
Germany

Phone: +49-(0)69-720040
Fax: +49-(0)69-720400
E-Mail: info@tectra.de
Web: www.tectra.de

Rev: Feb. 2017

C.3 K&L filter datasheet

Tubular .250 Inch Lowpass Filters

◆ **Features:**

- Miniature Size and Volume
- Higher Frequency of Operation

◆ **Specifications:**

K&L Part Number	3 dB Cutoff Frequency	Insertion Loss	VSWR	50 dB Rejection	Outline Dimension
6L250-00084	2000 MHz	<1.0 dB @ 1800	1.5:1 Typical	2720 to 9000 MHz	2.90 +/- .020
6L250-00085	4000 MHz	<1.0 dB @ 3600	1.5:1 Typical	5400 to 18,000 MHz	3.00 +/- .020
6L250-00086	6000 MHz	<1.0 dB @ 5400	1.5:1 Typical	8160 to 18,000 MHz	2.56 +/- .020
6L250-00088	10000 MHz	<1.0 dB @ 9000	1.5:1 Typical	13,600 to 20,000 MHz	1.89 +/- .020
6L250-00089	12000 MHz	<1.0 dB @ 10800	1.5:1 Typical	16,320 to 26,000 MHz	1.98 +/- .020

◆ **Applications:**

- Clean-Up Filters

◆ **Amplitude and VSWR Response**

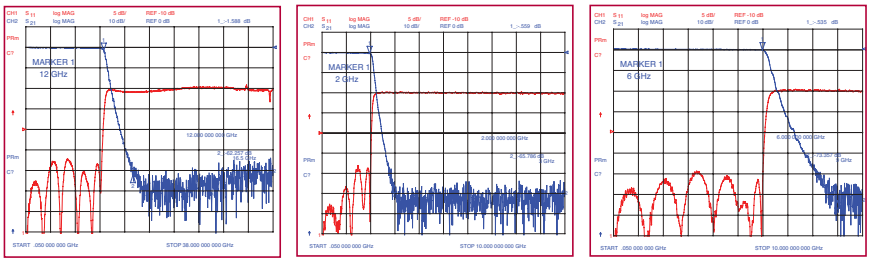

K&L MICROWAVE
A DOVER COMPANY

Filtering Solutions for Your Global Market

USA
Phone: 410-749-2424
FAX: 443-260-2268
Email: sales@klmicrowave.com

EUROPE
Phone: +44-(0)-1904-567355
FAX: +44-(0)-1904-675521
Email: sales@kleurope.com

www.klfilterwizard.com & www.klmicrowave.com

Figure C.1: Datasheet for K&L filter.

C.4 Product specification for GE varnish.

CMRdirect

Product Specification: GE / IMI 7031 [02-33-001]

Low temperature glue for thermally anchoring wires at cryogenic temperatures. Does not outgas after baking and can be used in vacuum. Can be air-dried or baked.

Thermal Conductivity	
1K	0.034 W/m-K
4.2K	0.062 W/m-K
77K	0.22 W/m-K
100K	0.24 W/m-K
300K	0.44 W/m-K

Viscosity at 298K	1300cps
Specific gravity at 298K	0.89
Maximum operating temperature	423K
Flash point (TOC)	253K
Air drying time	10 minutes at RT
Baking time	2-5 minutes at 398K
Thinner	Ethanol or 50.50 ethanol:toluene
Evaporation rate (Butyl Acetate = 1)	Less than 1
Volume resistivity	1013-1015 Ω/cm

Cambridge Magnetic Refrigeration, 19-21 Godesdone Road, Cambridge, CB5 8HR email info@cmr-direct.com

Figure C.2: Product specification for GE varnish low temperature glue.

f_r (GHz)	Temp. (mK)	$\delta_i/10^{-5}$	$\delta_0^{TLS}/10^{-5}$	$\delta_c/10^{-5}$	β	P_C	α	γ	Q_e	Q_i
5.82	50	3.40	1.70	1.38	0.67	$9.56 \cdot 10^{-9}$			500152	29412
5.82	Averages	3.02	1.53	1.51	0.70	$1.75 \cdot 10^{-6}$	2.562	0.032	296270	33577
6.21	50	17.5	1.79	15.8	0.59	$2.18 \cdot 10^{-8}$			7019	5714
6.21	Averages	17.33	1.59	15.89	0.57	$4.70 \cdot 10^{-6}$	2.19	0.031	6129	5772
6.67	50	149	0.95	148	1.32	$2.30 \cdot 10^{-9}$			733	671
6.67	Averages	285.37	0.22	310.19	-127.85	$1.52 \cdot 10^{-6}$	-7.59	-8.73	762	1452
7.06	50									
7.06	Averages	31.94	985.63	-625.32	-12.06	$5.34 \cdot 10^{-5}$	0	0	96356	3132
5.77	50	3.9	3.1	1.1	0.51	$3.95 \cdot 10^{-10}$			164873	25641
5.77	Averages	3.33	1.96	1.57	0.57	$5.74 \cdot 10^{-9}$	0.92	0.01	184764	30759
6.14	50	13.1	2.31	10.9	0.62	$2.02 \cdot 10^{-9}$			9845	7634
6.14	Averages	12.78	1.53	9.79	0.83	$5.50 \cdot 10^{-5}$	-10.52	0.13	10271	7855
6.56	50	116.4	1.15	115	1.88	$1.77 \cdot 10^{-9}$			906	859
6.56	Averages	111.23	0.64	110.64	-42.83	$4.65 \cdot 10^{-8}$	2.02	2.77	320	899
7.02	50	6.0	4.8	1.6	0.35	$8.19 \cdot 10^{-11}$			43121	16667
7.02	Averages	5.18	2.77	2.49	0.52	$1.50 \cdot 10^{-8}$	2.93	0.14	43326	19844
5.75	50	20.4	2.31	18.2	0.52	$4.02 \cdot 10^{-10}$			16736	4902
5.75	Averages	20.27	1.73	18.71	0.55	$2.02 \cdot 10^{-9}$	0.45	0.092	16031	4937
6.12	50	330	5.16	325	21.23	$4.09 \cdot 10^{-11}$			3233	303
6.12	Averages	339.62	513.34	15.06	94.70	4.20	9.1	20.9	2361	298
6.56	50	0	-43	19	-1.02	$2.98 \cdot 10^{-10}$			0	0
6.56	Averages	108.26	115521463.39	-109932476.06	0.00	$2.62 \cdot 10^{7}$	21.06	90987680	106820	1085
7.00	50	6.5	3.29	3.39	0.31	$8.15 \cdot 10^{-11}$			40437	15385
7.00	Averages	5.91	1.90	4.18	1.57	$1.30 \cdot 10^{-8}$	2.81	0.1	40237	17098

Table C.2: Data from resonator measurements and fits. δ_0, Q_e and Q_i are shown for lowest input power.

Bibliography

[1] Deutsche Forschungsgemeinschaft. Munich Center for Quantum Science and Technology. URL `https://www.mcqst.de/` (2021).

[2] T. Niemczyk, F. Deppe, E. P. Menzel, M. J. Schwarz, H. Huebl, F. Hocke, M. Häberlein, M. Danner, E. Hoffmann, A. Baust, E. Solano, J. J. Garcia-Ripoll, A. Marx & R. Gross. Selection rules in a strongly coupled qubit-resonator system. *Arxiv* 1–8 (2011).

[3] V. Bouchiat, D. Vion, P. Joyez, D. Esteve & M. H. Devoret. Quantum Coherence with a Single Cooper Pair. *Physica Scripta* **T76**, 165 (1998).

[4] B. D. Josephson. Possible new effects in superconductive tunnelling. *Physics Letters* **1**, 251–253 (1962).

[5] J. Koch, T. M. Yu, J. Gambetta, A. A. Houck, D. I. Schuster, J. Majer, A. Blais, M. H. Devoret, S. M. Girvin & R. J. Schoelkopf. Charge-insensitive qubit design derived from the Cooper pair box. *Physical Review A - Atomic, Molecular, and Optical Physics* **76**, 1–21 (2007).

[6] R. J. Schoelkopf & S. M. Girvin. Wiring up quantum systems. *Nature* **451**, 664–669 (2008).

[7] M. Hofheinz, H. Wang, M. Ansmann, R. C. Bialczak, E. Lucero, M. Neeley, A. D. O'Connell, D. Sank, J. Wenner, J. M. Martinis & A. N. Cleland. Synthesizing arbitrary quantum states in a superconducting resonator. *Nature* **459**, 546–549 (2009).

[8] J. Heinsoo, C. K. Andersen, A. Remm, S. Krinner, T. Walter, Y. Salathé, S. Gasparinetti, J. C. Besse, A. Potočnik, A. Wallraff & C. Eichler. Rapid High-fidelity Multiplexed Readout of Superconducting Qubits. *Physical Review Applied* **10**, 034040 (2018).

[9] M. Mariantoni, H. Wang, R. C. Bialczak, M. Lenander, E. Lucero, M. Neeley, A. D. O'Connell, D. Sank, M. Weides, J. Wenner, T. Yamamoto, Y. Yin, J. Zhao,

J. M. Martinis & A. N. Cleland. Photon shell game in three-resonator circuit quantum electrodynamics. *Nature Physics* **7**, 287–293 (2011).

[10] V. Ambegaokar & A. Baratoff. Tunneling between superconductors. *Physical Review Letters* **11**, 104 (1963).

[11] J. Gao, M. Daal, A. Vayonakis, S. Kumar, J. Zmuidzinas, B. Sadoulet, B. A. Mazin, P. K. Day & H. G. Leduc. Experimental evidence for a surface distribution of two-level systems in superconducting lithographed microwave resonators. *Applied Physics Letters* **92**, 152505 (2008).

[12] H. K. Onnes. The resistance of pure mercury at helium temperatures. *Communication from the Physical Laboratory at the University of Leiden* **120b, 122b and 124c** (1911).

[13] W. Meissner & R. Ochsenfeld. Ein neuer Effekt bei Eintritt der Supraleitfähigkeit. *Die Naturwissenschaften* **21**, 787–788 (1933).

[14] F. London & H. London. The electromagnetic equations of the supraconductor. *Proceedings of the Royal Society of London. Series A - Mathematical and Physical Sciences* **149**, 71–88 (1935).

[15] V. Ginzburg & L. Landau. On the Theory of superconductivity. *Zh. Eksp. Teor. Fiz.* **20**, 1064–1082 (1950).

[16] J. Bardeen, L. N. Cooper & J. R. Schrieffer. Theory of Superconductivity. *Phys. Rev.* **108**, 1175–1204 (1957).

[17] R. Gross, A. Marx, F. Deppe & K. Fedorov. Applied Superconductivity. *Lecture Notes* (2020).

[18] R. Gross & A. Marx. *Festkörperphysik* (2018).

[19] D. Pozar. Microwave engineering. *IEEE Potentials* **8**, 11–13 (1989).

[20] R. Klement. Zur Abtrennung des Rhodiums von Uran, Molybdän, Ruthenium, Palladium und Zirkonium aus Lösungen von Uran-Brennstofflegierungen. *Fresenius' Zeitschrift für analytische Chemie* **179**, 435–436 (1961).

[21] B. A. Mazin. *Microwave Kinetic Inductance Detectors*. Ph.D. thesis (2004).

[22] M. S. Khalil, M. J. A. Stoutimore, F. C. Wellstood & K. D. Osborn. An analysis method for asymmetric resonator transmission applied to superconducting devices. *Journal of Applied Physics* **111**, 054510 (2012).

[23] P. J. Petersan & S. M. Anlage. Measurement of resonant frequency and quality factor of microwave resonators: Comparison of methods. *Journal of Applied Physics* **84**, 3392–3402 (1998).

[24] S. Probst, F. B. Song, P. A. Bushev, A. V. Ustinov & M. Weides. Efficient and robust analysis of complex scattering data under noise in microwave resonators. *Review of Scientific Instruments* **86**, 024706 (2015).

[25] Q.-M. Chen, F. Deppe, Y. Nojiri, S. Pogorzalek, M. Renger, M. Partanen, K. G. Fedorov, A. Marx & R. Gross. Determination of the internal and coupling quality factors in both notch-type and transmission-type coplanar waveguide resonators. *Unpublished* (2020).

[26] N. Chernov & C. Lesort. Least Squares Fitting of Circles. *Journal of Mathematical Imaging and Vision* **23**, 239–252 (2005).

[27] J. Wenner, R. Barends, R. C. Bialczak, Y. Chen, J. Kelly, E. Lucero, M. Mariantoni, A. Megrant, P. J. J. O'Malley, D. Sank, A. Vainsencher, H. Wang, T. C. White, Y. Yin, J. Zhao, A. N. Cleland & J. M. Martinis. Surface loss simulations of superconducting coplanar waveguide resonators. *Applied Physics Letters* **99**, 113513 (2011).

[28] J. Goetz, F. Deppe, M. Haeberlein, F. Wulschner, C. W. Zollitsch, S. Meier, M. Fischer, P. Eder, E. Xie, K. G. Fedorov, E. P. Menzel, A. Marx & R. Gross. Loss mechanisms in superconducting thin film microwave resonators. *Journal of Applied Physics* **119** (2016).

[29] D. S. Wisbey, J. Gao, M. R. Vissers, F. C. S. da Silva, J. S. Kline, L. Vale & D. P. Pappas. Effect of metal/substrate interfaces on radio-frequency loss in superconducting coplanar waveguides. *Journal of Applied Physics* **108**, 093918 (2010).

[30] M. Arzeo, F. Lombardi & T. Bauch. Microwave losses in MgO, $LaAlO_3$, and $(La_{0.3}Sr_{0.7})(Al_{0.65}Ta_{0.35})O_3$ dielectrics at low power and in the millikelvin temperature range. *Applied Physics Letters* **104**, 212601 (2014).

[31] R. Barends, J. Wenner, M. Lenander, Y. Chen, R. C. Bialczak, J. Kelly, E. Lucero, P. O'Malley, M. Mariantoni, D. Sank, H. Wang, T. C. White, Y. Yin, J. Zhao, A. N. Cleland, J. M. Martinis & J. J. A. Baselmans. Minimizing quasiparticle generation from stray infrared light in superconducting quantum circuits. *Applied Physics Letters* **99**, 113507 (2011).

[32] A. Rothwarf & B. N. Taylor. Measurement of Recombination Lifetimes in Superconductors. *Physical Review Letters* **19**, 27–30 (1967).

[33] J. Gao, J. Zmuidzinas, A. Vayonakis, P. Day, B. Mazin & H. Leduc. Equivalence of the Effects on the Complex Conductivity of Superconductor due to Temperature Change and External Pair Breaking. *Journal of Low Temperature Physics* **151**, 557–563 (2008).

[34] D. C. Mattis & J. Bardeen. Theory of the anomalous skin effect in normal and superconducting metals. *Physical Review* **111**, 412–417 (1958).

[35] A. Vayonakis & J. Zmuidzinas. Radiative losses from 2-d apertures. URL `http://scholar.google.com/scholar?hl=en{&}btnG=Search{&}q=intitle:Radiative+Losses+from+2+?+D+Apertures{#}0`.

[36] C. R. H. McRae, H. Wang, J. Gao, M. R. Vissers, T. Brecht, A. Dunsworth, D. P. Pappas & J. Mutus. Materials loss measurements using superconducting microwave resonators. *Review of Scientific Instruments* **91**, 091101 (2020).

[37] C. Song, T. W. Heitmann, M. P. DeFeo, K. Yu, R. McDermott, M. Neeley, J. M. Martinis & B. L. T. Plourde. Microwave response of vortices in superconducting thin films of Re and Al. *Physical Review B* **79**, 174512 (2009).

[38] D. Kasilingam & D. Rutledge. Surface-Wave Losses of Coplanar Transmission Lines. In *MTT-S International Microwave Symposium Digest* Vol. 83113–116 (MTT005, 1983). URL `https://ieeexplore.ieee.org/stamp/stamp.jsp?tp=&arnumber=1130827&tag=1`.

[39] T. Noguchi, M. Naruse & Y. Sekimoto. RF conductivity and surface impedance of a superconductor taking into account the complex superconducting gap energy. *Physics Procedia* **36**, 318–323 (2012).

[40] E. Xie. *Optimized fabrication process for nanoscale Josephson junctions used in superconducting quantum circuits*. Master's thesis, Technische Universität München (2013).

[41] J. Goetz. *The Interplay of Superconducting Quantum Circuits and Propagating Microwave States*. Ph.D. thesis (2017). URL `http://www.wmi.badw.de/publications/theses.htm`.

[42] G. Frossati. Experimental techniques: Methods for cooling below 300 mK. *Journal of Low Temperature Physics* **87**, 595–633 (1992).

[43] N. Cabrera & N. F. Mott. Theory of the oxidation of metals. *Reports on Progress in Physics* **37**, 231–316 (1974).

[44] J. E. Boggio. The pressure dependence of the oxidation of aluminum at 298 °K. *Surface Science* **14**, 1–6 (1969).

[45] E. Xie. *A scalable 3D quantum memory*. Ph.D. thesis (2018).

[46] V. L. Stout & M. D. Gibbons. Gettering of Gas by Titanium. *Journal of Applied Physics* **26**, 1488–1492 (1955).

[47] A. Bilmes. *Resolving locations of defects in superconducting transmon qubits*. Ph.D. thesis (2019).

[48] K. Geerlings, S. Shankar, E. Edwards, L. Frunzio, R. J. Schoelkopf & M. H. Devoret. Improving the quality factor of microwave compact resonators by optimizing their geometrical parameters. *Applied Physics Letters* **100**, 192601 (2012).

[49] J. M. Sage, V. Bolkhovsky, W. D. Oliver, B. Turek & P. B. Welander. Study of loss in superconducting coplanar waveguide resonators. *Journal of Applied Physics* **109**, 063915 (2011).

[50] J. Gao. *The physics of superconducting microwave resonators*. Ph.D. thesis (2008).

Acknowledgement

In this part, I would like to thank all the people that contributed to this thesis.

First, I want to thank **Dr. Frank Deppe**, for giving me the opportunity to do my master thesis in the qubit group at the Walther-Meißner-Institute. His feedback is always very constructive and his corrections increased the quality of this thesis a lot.

Second, I thank **Yuki Nojiri**, who worked together with me on the fabrication process. Our extensive discussions about fabrication, but also about theory aspects, were always helpful and gave a lead for improvements on this work.

Further, I want to thank **Qi-ming Chen** for providing me the Python script in order to analyze our resonator measurements and for explaining the theory of the fitting procedure.

Next, I thank **Thomas Brenninger** for helping me with the implementation of the new evap sample holder. Besides that, he always immediatly helped, when a machine was not working properly anymore.

Furthermore, thanks to all Master and Ph.D. students at the Walther-Meißner-Institute for your great support. Special thanks are directed to **Florian Fesquet**, **Emir Karadza**, **Manuel Müller**, and **Leander Peis**.

I express gratitude to my girlfriend, **Anna Maria**, for supporting me during the whole time of this work.

Last but not least, I thank my parents, **Rosmarie** and **Peter**, for providing me the opportunity to study physics and supporting me for my whole life.